# FINITE ELEMENT SIMULATIONS OF LAMINATED COMPOSITE FORMING PROCESSES

René ten Thije

De promotiecommissie is als volgt samengesteld:

| | |
|---|---|
| *voorzitter en secretaris:* | |
| Prof. dr. F. Eising | Universiteit Twente |
| *promotoren:* | |
| Prof. dr. ir. R. Akkerman | Universiteit Twente |
| Prof. dr. ir. J. Huétink | Universiteit Twente |
| *leden:* | |
| Prof. dr. P. Boisse | LaMCoS, INSA de Lyon |
| Prof. dr. Z. Gürdal | Technische Universiteit Delft |
| Prof. dr. ir. J.W.M. Noordermeer | Universiteit Twente |
| Prof. dr. ir. J.J.W. van der Vegt | Universiteit Twente |

Keywords: anisotropy, finite element, large deformation, intra-ply shear locking, laminated composite

First print, September 2007

ISBN-13: 978-90-365-2546-6


Printed by PrintPartners Ipskamp B.V., Enschede, the Netherlands

*Cover: The Airbus A380 touches down on its first arrival at Charles de Gaulle Airport, June 2007. Photo by Airbus S.A.S.*©

# FINITE ELEMENT SIMULATIONS OF LAMINATED COMPOSITE FORMING PROCESSES

PROEFSCHRIFT

ter verkrijging van
de graad van doctor aan de Universiteit Twente,
op gezag van de rector magnificus,
prof. dr. W.H.M. Zijm,
volgens besluit van het College van Promoties
in het openbaar te verdedigen
op vrijdag 21 september 2007 om 16.45 uur

door

René Hermanus Willem ten Thije

geboren op 21 april 1977

te Hengelo Ov.

Dit proefschrift is goedgekeurd door de promotoren:

Prof. dr. ir. R. Akkerman
Prof. dr. ir. J. Huétink

# Summary

Continuous Fibre Reinforced Polymers (CFRPs) combine strength and stiffness of fibres with the design flexibility of polymeric matrix materials. Fast production methods like thermo-folding, diaphragm forming or stamping can produce large numbers of CFRP components in a cost efficient way. Pre-consolidated laminates are heated above their melting temperature and subsequently re-shaped. These forming processes can introduce unacceptable shape distortions such as springback, wrinkling or tearing.

The objective of this research is the development of a design tool for high precision CFRP components made from multi-layer laminates. Optimisation of the CFRP design and the forming process reduces costly trial-and-error procedures and can significantly shorten the time-to-market. This requires a predictive model that is robust, accurate and fast. Such an all-encompassing procedure is not readily available.

Forming processes of single-layer and multi-layer composite materials have been successfully simulated using the Finite Element (FE) method. A new non-linear FE formulation was developed to accurately simulate large deformations of highly anisotropic materials, for which the traditional FE formulations appeared to be inadequate. An appropriate decomposition of the deformation gradient results in constitutive equations formulated in invariant tensors. Consistent tangent matrices were derived for general anisotropic, elastic materials and plastically deforming fibres. Multiple two and three dimensional analyses showed quadratic convergence for simulations with large strain increments and large rotations.

Intra-ply shear locking is a numerical artefact that can deteriorate the simulation results. Several solutions to this problem were implemented in various element types. They were tested in a two dimensional simulation of a bias extension experiment and a three dimensional realistic drape simulation. Selective reduced integration is a straightforward solution to

eliminate locking, but compromises performance of simulations with large deformations. Therefore an assumed strain element has been developed. This element contains additional degrees of freedom that represent the fibre strain field. It was demonstrated that the new element performs significantly better than other solutions.

A multi-layer element has been developed for efficient simulations of laminated composite forming processes with only one element through the thickness. Simulations were validated against drape experiments, in which multi-layered pre-consolidated laminates of different lay-ups were formed on a dome geometry. The experiments emphasised the importance of inter-ply interactions during forming of laminated composites. Simulations and experiments agree very well up to the point at which wrinkling starts. Membrane elements were used for simulation time arguments. They proved capable of predicting the material instabilities during forming, but are unsuited for realistic wrinkling simulations due to the lack of a bending stiffness. Several strategies are discussed as to how the simulations can be used as an effective and predictive tool during the optimisation of layered CFRP products.

# Samenvatting

Continue-vezelversterkte polymeren combineren de sterkte en stijfheid van vezels met de ontwerpvrijheid van polymere matrixmaterialen. Deze composieten zijn geschikt voor economisch aantrekkelijke, snelle productiemethoden zoals thermovouwen, membraanvormen of persen. Bij deze methoden worden voorgeconsolideerde laminaten tot boven de smelttemperatuur verhit en vervolgens vormgegeven. Hierbij kunnen echter ongewenste en onacceptabele vervormingen optreden, waarvan maatonnauwkeurigheid, plooivorming en scheurvorming enkele voorbeelden zijn.

Het doel van dit onderzoek is de ontwikkeling van een ontwerpgereedschap voor het maatnauwkeurig produceren van meerlaagse composietproducten. Optimalisatie van het ontwerp en het productieproces met behulp van dit ontwerpgereedschap reduceert kostbare trial-and-error-procedures en kan de time-to-market aanzienlijk verkorten. Voor een dergelijk gereedschap is een voorspellend model nodig, dat tegelijkertijd robuust, nauwkeurig en efficiënt is qua rekentijd. Momenteel is er geen model beschikbaar dat aan al deze eisen voldoet.

Binnen dit onderzoek is de productie van enkel- en meerlaagse composieten succesvol gesimuleerd met behulp van de eindige-elementenmethode. Conventionele eindige-elementenformuleringen bleken ongeschikt om grote vervormingen van zeer anisotrope materialen nauwkeurig te simuleren. Daarom is er een nieuwe niet-lineaire formulering opgezet, waarbij een geschikte ontbinding van de vervormingstensor resulteert in constitutieve vergelijkingen die uitgedrukt kunnen worden in invariante tensoren. De consistente tangentmatrices voor algemeen anisotroop elastisch materiaal, elastisch vervormende vezels en elastoplastisch vervormende vezels zijn opgesteld. Meerdere twee- en driedimensionale simulaties met grote vervormingen en rotaties toonden aan dat het convergentiegedrag kwadratisch is, waarmee de consistentie van de tangentmatrices is aangetoond.

Intra-ply shear locking is een numeriek probleem dat de resultaten van simulaties met vezelversterkte materialen onbruikbaar kan maken. Een aantal oplossingen voor dit probleem zijn geïmplementeerd in verschillende typen elementen. Deze oplossingen zijn getest in een tweedimensionale simulatie van het bias extension experiment en in een realistische driedimensionale drapeersimulatie. Hieruit is gebleken dat selectieve gereduceerde integratie een eenvoudige methode is om locking the voorkomen. Het verlaagde echter de convergentiesnelheid van simulaties met grote vervormingen. Deze tekortkoming is opgelost door de onwikkeling van een assumed strain element, een element waarin randvoorwaarden betreffende het rekveld expliciet zijn vastgelegd. Het element bevat extra vrijheidsgraden die de rek in de vezels vastleggen. Uit simulaties bleek dat het nieuwe assumed strain element sneller convergeert en robuuster is dan het element met selectieve gereduceerde integratie.

Er is een element ontwikkeld dat de respons kan simuleren van een laminaat dat bestaat uit meerdere lagen, waarbij wrijving tussen de verschillende lagen meegenomen wordt. Op deze manier kan de vervorming van een meerlaagscomposiet efficiënt worden gesimuleerd met slechts één enkel element over de dikte. Er zijn simulaties uitgevoerd met meerlaagse composieten van verschillende opbouw, die op een bolvormige geometrie gedrapeerd werden. Deze simulaties zijn geverifieerd met experimenten. Deze experimenten benadrukten dat de wrijving tussen de individuele lagen van het laminaat tijdens de productie in hoge mate kan bijdragen aan de ongewenste vervormingen in het uiteindelijke product. De resultaten van de simulaties en de experimenten kwamen goed overeen tot het punt waarop plooivorming in het product ontstond. De simulaties maakten gebruik van membraanelementen om de simulatietijd te beperken. Deze elementen bleken in staat om het begin van materiaalinstabiliteiten te voorspellen, maar door hun gebrek aan buigstijfheid waren ze niet geschikt voor realistische simulaties van plooivorming. Enkele strategien zijn uitgewerkt om de voorspellende kwaliteiten van dit meerlaagse element efficiënt in te zetten tijdens de optimalisatie van meerlaagse composietproducten.

# Nomenclature

List of abbreviations and symbols used.

## Abbreviations

| | |
|---|---|
| ALE | Arbitrary Lagrangian Eulerian |
| CFRP | Continuous Fibre Reinforced Polymer |
| CFRTP | Continuous Fibre Reinforced ThermoPlastics |
| (C)MF | (Constant) Multi-Field |
| CP | Cross-Ply |
| DOF, dof | Degree Of Freedom |
| DRIL | Allmann88 triangle with DRILling dofs |
| FE(M) | Finite Element (Method) |
| FLD | Forming Limit Diagram |
| H | Harness weave |
| LTR | Linear/simplex TRiangular element |
| PPS | PolyPhenylene Sulfide |
| QI | Quasi-Isotropic |
| QUAD | QUADrilateral element |
| RPF | Rubber Press Forming |
| (S)QTR | (Semi) Quadratic TRiangular element |
| (S)RI | (Selective) Reduced Integration |
| XFEM | Extended Finite Element Method |

## Scalars

| | |
|---|---|
| $C$ | Mooney-Rivlin material parameters |
| $E$ | Young's modulus |
| $h$ | film thickness |
| $I$ | invariants of the left Cauchy strain tensor |
| $J$ | Jacobian, volume ratio |
| $\ell$, $L$ | length |

| | |
|---|---|
| $p$ | hydrostatic pressure |
| $q$ | scalar weight function |
| $R$ | radius |
| $r$ | constraint ratio |
| $S$ | principal stress |
| $t$ | time |
| $u$, $v$, $w$ | displacement in $x$, $y$, $z$-direction |
| $V$ | volume |
| $\Gamma$ | surface area |
| $\gamma$ | shear deformation |
| $\delta$ | increment |
| $\epsilon$ | error norm, convergence criterion |
| $\varepsilon$ | strain |
| $\eta$ | viscosity |
| $\eta_0$, $C$, $n$ | Cross model parameters |
| $\lambda$ | contraction ratio |
| $\nu$ | volume fraction |
| $\rho$ | density |
| $\sigma_0$, C, $\varepsilon_0$, $n$ | Nadai stress-strain curve parameters |
| $\sigma$ | stress |
| $\psi$ | free energy |

## Vectors

| | |
|---|---|
| $\mathbf{a}$ | fibre direction |
| $\mathbf{e}$ | base vector |
| $\mathbf{n}$ | normal vector |
| $\mathbf{t}$ | boundary traction |
| $\mathbf{u}$ | displacement |
| $\mathbf{v}$ | velocity |
| $\mathbf{w}$ | vector of weight functions |
| $\mathbf{X}$ | Lagrangian vector |
| $\mathbf{x}$ | Eulerian vector |
| $\boldsymbol{\tau}$ | interface traction |

## Tensors

| | |
|---|---|
| $\mathbf{B}$ | left Cauchy-Green strain |
| $\mathbf{C}$ | right Cauchy-Green strain |
| $\mathbf{D}$ | rate of deformation |

| | |
|---|---|
| $\mathbf{d}$ | invariant rate of deformation |
| ${}^4\mathbf{E}$ | fourth order material tensor |
| $\mathbf{F}$ | deformation gradient |
| $\mathbf{G}$ | stretch tensor |
| $\mathbf{I}$ | second order unit tensor |
| ${}^4\mathbf{I}$ | fourth order unit tensor |
| $\mathbf{L}$ | velocity gradient |
| $\mathbf{L}_g$ | adapted velocity gradient |
| $\mathbf{R}$ | rotation tensor |
| $\mathbf{W}$ | spin tensor from polar decomposition |
| $\boldsymbol{\sigma}$ | Cauchy stress |
| $\boldsymbol{\tau}$ | local stress |
| $\boldsymbol{\Omega}$ | general spin tensor |

## Vector / Matrix notated

| | |
|---|---|
| $\{\boldsymbol{\varepsilon}\}$ | strain tensor in compressed or Voigt notation |
| $[\mathbf{B}]$ | derivatives of the element shape functions |
| $\mathbf{F}$, $\mathbf{R}$ | force vector |
| $\mathbf{N}$, $\mathbf{M}$ | vector element interpolation functions |
| $[\mathbf{K}]$ | tangent/stiffness matrix |

## Subscripts

| | |
|---|---|
| $0$ | initial/reference value |
| $e$ | elastic |
| $f$ | in the fibre direction |
| $p$ | plastic |
| $y$ | yield |
| $xyz$ | cartesian coordinates |

## Superscripts

| | |
|---|---|
| $k$ | nodal index |
| $d$ | deviatoric part |

## Mathematical

| | | | |
|---|---|---|---|
| $\overrightarrow{\nabla}$ | pre-gradient, e.g. | $\mathbf{A} = \overrightarrow{\nabla}\mathbf{b}$ | $a_{ij} = b_{j,i}$ |
| $\overleftarrow{\nabla}$ | post-gradient, e.g. | $\mathbf{A} = \mathbf{b}\overleftarrow{\nabla}$ | $a_{ij} = b_{i,j}$ |
| $\cdot\overleftarrow{\nabla}$ | divergence, e.g. | $\mathbf{a} = \mathbf{B} \cdot \overleftarrow{\nabla}$ | $a_i = b_{ij,j}$ |
| $\cdot$ | contraction, inner product, e.g. | $\mathbf{A} = \mathbf{B} \cdot \mathbf{C}$ | $a_{ij} = b_{ik}c_{kj}$ |
| (default) | dyadic product, e.g. | $\mathbf{A} = \mathbf{bc}$ | $a_{ij} = b_i c_j$ |
| : | double contraction, e.g. | $a = \mathbf{B} : \mathbf{C}$ | $a = b_{ij}c_{ij}$ |
| $\times$ | cross product | $\mathbf{a} = \mathbf{b} \times \mathbf{c}$ | $a_i = \varepsilon_{ijk}b_j c_k$ |
| $A^T$ | transpose | | |
| $\dot{A}$ | time derivative | | |
| $\triangle$ | difference | | |
| $\partial$ | partial differentiator | | |

# Contents

# Chapter 1

# Introduction

Continuous Fibre Reinforced Polymers (CFRPs) consist of strong and stiff continuous fibres embedded in a polymeric matrix material. The primary function of the fibres is to improve the mechanical properties of the matrix material. CFRPs made of glass, carbon or aramid fibres are widely used and well known, but for some typical applications less common reinforcements are used. This includes for example the use of steel cords as reinforcement in plastic oil-pipes, natural fibres for bio-degradable products or highly oriented thermoplastics like Dyneema® for bullet proof vests. Together with a wide variety of matrix materials, this leads to numerous material combinations, which are typically stiff, strong, corrosion resistant and have good fatigue properties. An example of a project that would have been impossible without modern CFRPs is shown in figure 1.1. SpaceShipOne was the first private spaceship that flew out of the atmosphere in 2004.

*Figure 1.1: SpaceShipOne on its way to space, a project impossible without CFRPs. Photo by Scaled Composites.*

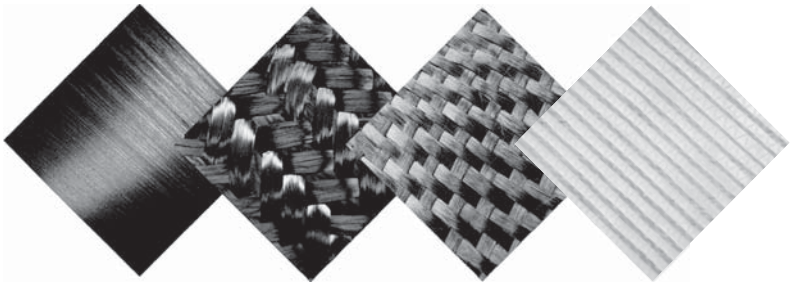

*Figure 1.2: Several types of continuous fibre reinforcements. From left to right a unidirectional prepreg, a braid, a woven fabric and a non crimp fabric.*

## 1.1 CFRP production

Perhaps one of the most important advantage in designing CFRP components is the design flexibility. The polymer matrix material can be shaped arbitrarily. Thermoset polymers can be moulded only once, while thermoplastic polymers can be re-heated and re-moulded multiple times until the level of degradation is unacceptable. The ability of thermoplastics to melt allows for fast and cost efficient production methods. It makes products suitable for recycling as well, an increasingly important aspect nowadays. Thermoset polymers are generally slightly stronger and better suited for high temperature use than thermoplastics.

Well designed CFRPs have a high stiffness to weight ratio, making them suitable for structural aircraft components. Primarily glass and carbon fibres are used for this application. Processes like filament winding are capable of processing individual yarns on their own, but generally fibres are arranged in a sheet form to make handling possible. Figure 1.2 shows four examples of these sheet forms. Prepreg is a combination of yarns and a yet uncured thermoset matrix. The braids and fabrics consist of dry yarns.

The initially planar material is formed into a final three dimensional shape during forming. When this shape is doubly curved, a stiff product is created by exploiting the high membrane stiffness of the material. Three strategies are followed. The first strategy involves the manual layup of prepreg material followed by an autoclave cycle. This conventional method has long been the standard in aerospace industry. The second strategy is to deposit the dry reinforcement in a mould, followed by the addition of a thermoset resin. Dry fabrics, which are pre-shaped to the mould geometry before impregnation,

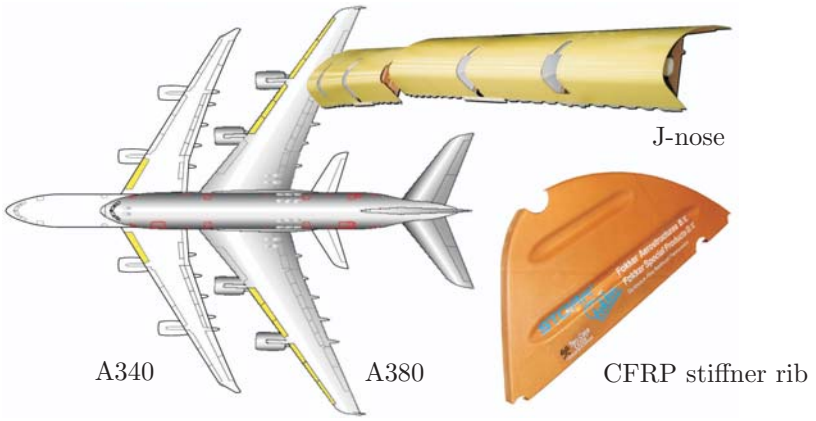


*Figure 1.3: CFRP stiffner ribs in the J-nose of the Airbus A340 and A380.*

are known as preforms. Production processes such as hand lay-up, vacuum infusion or resin transfer moulding follow this strategy. The third strategy is to create a pre-consolidated flat laminate first, by using a thermoplastic matrix material. This laminate is then reheated and when the matrix material has melted, it is formed into the final three dimensional shape. Typical examples of this production strategy are thermo-folding, diaphragm forming and rubber pressing. These fast methods can produce large numbers of composite products in a cost efficient way, without compromising the structural strength and will contribute to the growing use of composites in the aerospace industry [1].

Currently, new promising methods like fibre placing are under development as well. Though this is a costly process, it produces components with very good mechanical properties and increases the design flexibility even further by allowing full control of the fibre deposition.

The research in this thesis focusses on the rapid production methods of multi-layer pre-consolidated laminates. A typical product resulting from these processes is the stiffner rib shown in figure 1.3. It is produced by Stork Fokker AESP using the rubber pressing process. The thin-walled stiffner rib consists of four layers of thermoplastic material, reinforced with a woven glass fibre fabric. It is produced by first heating a pre-consolidated laminate, followed by a press cycle in which the laminate is formed between a steel mould and a rubber counterpart.

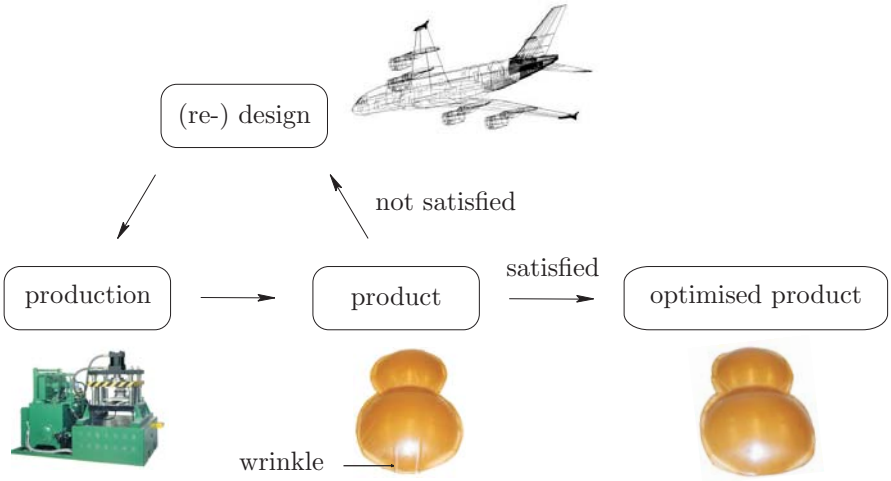


*Figure 1.4: Iterative optimisation cycle of a product.*

## 1.2 Product optimisation

Manufacturing processes can lead to unacceptable shape distortions in CFRP products. The thin walled products exhibiting double curvature are especially susceptible to springback, wrinkling or inefficient fibre distribution upon forming. These distortions depend on a wide variety of parameters, like e.g. the geometry, material properties, lay-up, process temperatures and friction. Redesign of the product or production process is necessary until the end result is satisfactory, as schematically illustrated in figure 1.4.

Optimisation through a trial and error procedure usually results in an acceptable product, but it is always accompanied by additional labour costs, machine time and scrap products. Numerical tools that can simulate the production processes can help the designer to optimise the product in the design phase and ideally lead to a first-time-right production cycle. These optimisations require a robust, accurate and yet fast numerical procedure, which is not readily available for anisotropic, multi-layered materials like CFRPs.

## 1.3 Deformation mechanisms of CFRPs

The mechanical behaviour of continuous fibre reinforced materials differs significantly from other materials by the presence of the fibres with their

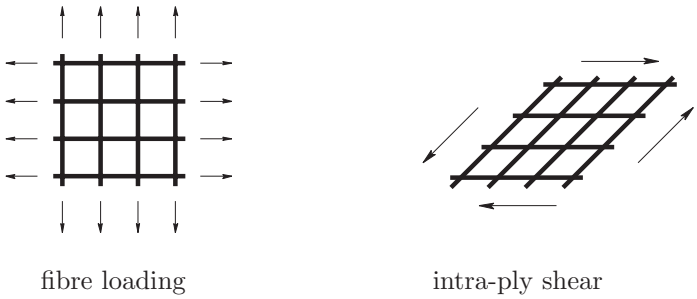


*Figure 1.5: Primary intra-ply deformation mechanisms.*

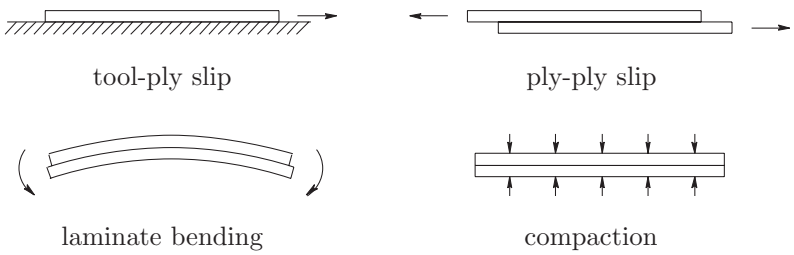


*Figure 1.6: Inter-ply and out-of-plane deformation mechanisms.*

dominant stiffness. Figure 1.5 shows the two most important in-plane deformation mechanisms of a biaxial woven fabric. The first one is fibre loading, shown at the left hand side of the figure. The initial stiffness of the tows under tensile loading can be low due to their waviness. Once fully stretched, elongation of the fibres is often negligible compared to other deformation mechanisms.

The second mechanism, intra-ply shear, is the primary deformation mode when forming biaxial fabrics into doubly curved shapes. This mode is also referred to as the trellis mode. Parallel fibres rotate with each fibre crossing acting as a hinge point. The response of the laminate in shear will be rate and temperature dependent if the fabric has been impregnated. When sheared, inter-tow compaction occurs due to the decrease in surface area and the deformation will get blocked at a certain shear angle, the locking angle. Two widely used experimental methods to examine the shear behaviour of biaxial fabrics are the bias extension and the picture frame test. Details on these test methods can be found in [2].

Figure 1.6 shows four deformation mechanisms that are important besides the intra-ply mechanisms. Tool-ply and ply-ply friction is often a combination of dry and lubricated friction. Friction transfers the external loads into the material and can cause wrinkling or fibre buckling in internal plies or in the laminate as a whole. The bending stiffness of thin laminates is often negligible compared to the membrane stiffness. When the number of plies increases, the influence of the bending stiffness during forming can become significant. Compaction of the plies is important in the consolidation phase of the production process. Poor compaction causes voids between the individual plies and this results in inferior mechanical behaviour. Again, details on these deformation mechanisms and experimental methods to analyse these can be found in [2].

## 1.4 Forming simulations

There are two main approaches to composite forming simulations: the geometrical approach and the Finite Element (FE) approach. The geometrical or mapping algorithms date back to the 1950s, when Mack and Taylor predicted the fibre distribution of a woven cloth on simple geometries based on a pin jointed net assumption [3]. One chooses a starting point and two initial fibre directions on the product surface. The position of the next fibre crossing is found by solving a local geodesic problem, assuming that the fibres are inextensible and shear is the only deformation mechanism. This process continues until the complete geometry has been covered. These simple geometrical models are fast, with simulation times in the order of seconds and are often sufficient for preliminary design studies.

Finite element simulations are based on solving equilibrium for the complete structure, rather than using a simple mapping algorithm. They are capable of simulating the production process in great detail by including e.g. complex material models and boundary conditions such as tool-part friction. Simple FE simulations are still relatively fast with simulation times of several minutes, but this number increases significantly if more complexities are added. A full three dimensional pressing simulation of a multi-layer CFRP product including friction can take a few hours up to days. These complex simulation are sometimes inevitable for an accurate prediction of the shape distortions in CFRP products as illustrated in the next example. Figure 1.7 shows a schematic representation of the rubber pressing process used to create a z-profile.

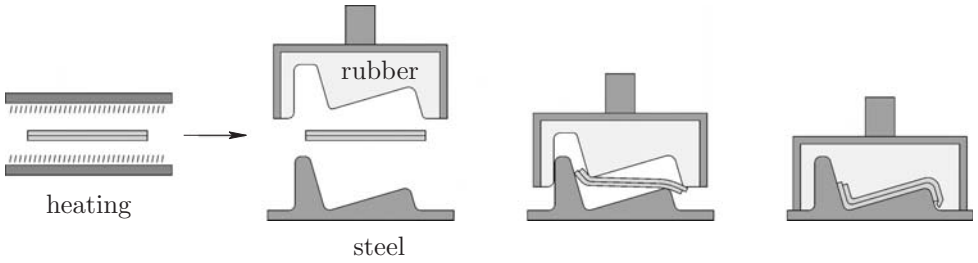


*Figure 1.7: The rubber pressing process.*

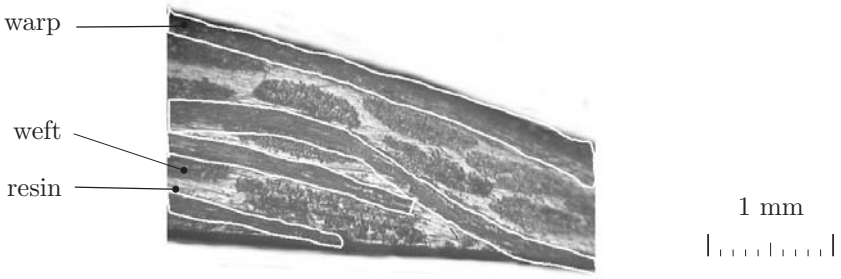


*Figure 1.8: Process induced transverse shear and slip in a laminated composite [5].*

After heating, the pre-consolidated laminate is formed between a rubber female mould and a steel male mould. The steel mould rapidly cools down the laminate and the product is removed after a consolidation period of minutes. The closing of the moulds introduces transverse shear and slip between the different layers of the laminate as illustrated in figure 1.7. Research by Lamers [4] and Wijskamp [5] showed that inter-ply and the tool-ply friction can introduce significant residual stresses upon forming, causing severe shape distortions of the final product. Figure 1.8 shows a picture of a cross-section of a laminate after forming, as seen with a microscope. The raw material was cut from a pre-consolidated laminate and the layers were consequently aligned at the right hand side before forming. Transverse shear of the laminate and slip between the layers has occurred upon forming, as is clearly visible in the figure. The top layer has moved around 2 mm with respect to the bottom layer. The finite element method is most suited for accurate simulations of these phenomena. Geometric draping analyses are not eligible, since the effects of inter-ply and tool-ply interactions cannot be included.

## 1.5 Finite element modelling

One of the earliest elastic finite element models was applied by Chen and Govindaraj in the 1990s [6]. They simulated the draping of a woven cloth on a table, considering the fabric a continuous, orthotropic medium. Although fabrics are discontinuous at lower length scales, the continuous approach has proven to be successful in many forming simulations. Special attention should be given to the constitutive equations, as the fibre directions change upon forming. The stiffness of the fibres is dominant and their orientation should be followed accurately. A continuum description of the reinforced material allows for implementation in standard, commercial FE packages. Many continuum models of fibre reinforced composites were successfully implemented using the user subroutines available in ABAQUS© [7–10].

Reinforcements can also be included in FE models by adding bar or truss elements to standard continuum elements. The mechanical behaviour of the (often isotropic) matrix material is modelled by the continuum elements and the response of the fibres by the truss elements. This approach has been used by several researchers [11, 12] and was implemented as a standard option in the commercial FE programs ABAQUS© and MSC MARC©. Modelling each individual yarn as a discrete element is computationally too expensive for forming simulations of fibre reinforced materials. This approach is limited to the microscale range, where it can provide information of e.g. the local compaction behaviour [13, 14].

Finite element forming simulations of single layer reinforced composites gradually become common nowadays, even in commercial environments. This is mainly due to the increased understanding of the material deformation mechanisms and the simulation techniques. The increase in computational power of modern computers is an important factor as well, making the complex and time-consuming simulations commercially more attractive. However, forming simulations of multi-layer composites including tool-ply and ply-ply slip are still in a research stage. Stacking several plies with contact logic and an appropriate friction characterisation between each layer is a straightforward method to model these materials. This approach causes the FE model to grow rapidly and in combination with the computationally expensive contact logic, it slows down the simulation to unacceptable levels. Some researchers successfully simulated the forming of a multi-layer composite with this approach on a small scale [15].

Modelling the multi-layer laminate with one element through the thickness is computationally more attractive than modelling the separate layers individually. Contact logic between the layers is avoided, which saves time and avoids instabilities. Lamers [4] developed a triangular membrane element that contains multiple layers, but having only nine degrees of freedom for each configuration. These degrees of freedom represent the global displacement of the laminate and the displacement of the individual layers is solved locally by an energy minimisation algorithm. This method proved to be fast in multi-layer simulations, but failed to accurately capture the tool-ply interaction, as shown by Wijskamp [5]. Wijskamp proposed to use global degrees of freedom in at least the top and bottom layer of the element to improve the accuracy of the tool-ply interaction. This will improve the simulation results of the important transverse effects, which are shown in figure 1.8.

## 1.6 Objective

The objective of this research is to develop a design tool that assists the designer in optimising the design and production of laminated composites, made from multi-layer laminates or preforms. Shape distortions in the final product can be minimised by adjusting the design of the product or by correction of tool geometries beforehand. This requires a predictive model that is both numerically efficient and accurate.

## 1.7 Outline

Simply implementing a highly anisotropic material model in a standard finite element code is not always successful. Large deformation FE simulations of highly anisotropic materials often show slow convergence or break down with increasing anisotropy and deformation. Chapter two describes a conceptually simple method, which makes the implementation of anisotropic material models straightforward. The method proved to be robust, accurate and provides quadratic convergence, even in simulations including plastic deformation of the fibres.

Intra-ply shear locking is a numerical problem. Standard elements have continuous displacement fields and cannot represent intra-ply shear deformation within the element. This causes unrealistically high fibre stresses and spurious wrinkling. Locking can be avoided by aligning the meshes with the fibre directions. Since this solution is only possible up to a maximum of two fibre directions per element, it is useless for multi-layer elements. Alternate solutions to this problem are presented in chapter three.

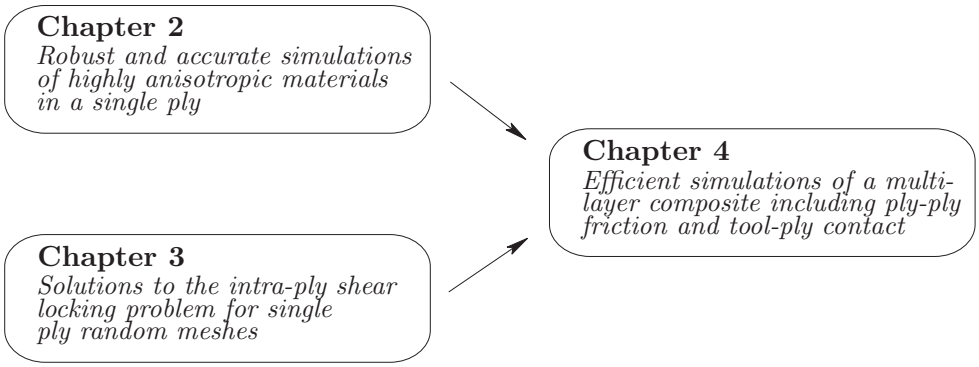


*Figure 1.9: Outline of this thesis.*

In chapter four a multi-layer element is presented that includes the solutions given in chapter two and three. Each layer has been modelled according to the method presented in chapter two and the numerical locking problem was solved as described in chapter three. The separate plys of a laminate were modelled with one element through the thickness, avoiding computationally expensive contact logic and the associated instabilities. The element includes ply-ply friction and tool-ply contact. The results of a rubber pressing simulation of a laminated composite were validated against experiments.

Chapters two, three and four were submitted as scientific publications to journals. Therefore, a slight overlap exists of some of the topics covered in the introductory parts. An interconnecting summary of the conclusions and recommendations for further research are presented in chapter five.

The article-based structure of the thesis limits the space for the elucidation of formulas or ideas. Therefore, the appendices present a detailed look into the finite element formulations of the most important material models and boundary conditions that were used within this research. Attention has been payed to the derivation of consistent tangent matrices, since these significantly improve convergence speed and hence simulation times of implicit finite element simulations.

## Bibliography

[1] A. Offringa. 'Thermoplastics in aerospace, a stepping stone approach'. Technical report, Stork Fokker AESP B.V., 2006.

[2] A. C. Long, editor. *Composites forming technologies.* Woodhead Publishing Ltd, Cambridge, England, 2007. ISBN 978-1-84569-033-5.

[3] C. Mack and H. Taylor. 'The fitting of woven cloth to surfaces'. *J Text I*, 47:477–487, 1956.

[4] E. A. D. Lamers. *Shape distortions in fabric reinforced composites due to processing induced fibre reorientation.* Ph.D. thesis, University of Twente, the Netherlands, 2004. ISBN 90-365-2043-6.

[5] S. Wijskamp. *Shape distortions in composite forming.* Ph.D. thesis, University of Twente, the Netherlands, 2005. ISBN 90-365-2175-0.

[6] B. Chen and M. Govindaraj. 'A physically based model of fabric drape using flexible shell theory'. *Text Res J*, 65:324–330, 1995.

[7] A. Spencer. 'Theory of fabric-reinforced viscous fluids'. *Compos Part A-Appl S*, 31:1311–1321, 2000.

[8] W.-R. Yu, P. Harrison and A. Long. 'Finite element forming simulation for non-crimp fabrics using a non-orthogonal constitutive equation'. *Compos Part A-Appl S*, 36:1079–1093, 2005.

[9] X. Peng and J. Cao. 'A continuum mechanics-based non-orthogonal constitutive model for woven composite fabrics'. *Compos Part A-Appl S*, 36:859–874, 2005.

[10] P. Xue, X. Peng and J. Cao. 'Non-orthogonal constitutive model for characterizing woven composites'. *Compos Part A-Appl S*, 34:183–193, 2003.

[11] S. Reese. 'Meso-macro modelling of fibre-reinforced rubber-like composites exhibiting large elastoplastic deformation'. *Int J Solids Struct*, 40:951–980, 2003.

[12] S. B. Sharma and M. P. F. Sutcliffe. 'A simplified finite element model for draping of woven material'. *Compos Part A-Appl S*, 35:637–643, 2004.

[13] D. Durville. 'Numerical simulation of entangled materials mechanical properties'. *J Mater Sci*, 40:5941–5948, 2005.

[14] S. V. Lomov, D. S. Ivanov, I. Verpoest, M. Zako, T. Kurashiki, H. Nakai and S. Hirosawa. 'Meso-FE modelling of textile composites: Road map, data flow and algorithms'. *Compos Sci Technol*, 67:1870–1891, 2007.

[15] D. Soulat, A. Cheruet and P. Boisse. 'Simulation of continuous fibre reinforced thermoplastic forming using a shell finite element with transverse stress'. *Comput Struct*, 84:888–903, 2006.

# Chapter 2

# Large deformation simulation of anisotropic material using an updated Lagrangian finite element method*


## Abstract

Large deformation Finite Element (FE) simulations of anisotropic material often show slow convergence or break down with increasing anisotropy and deformation. Large deformations are generally approximated by multiple small linearised steps. This leads to poor performance and contradicting formulations. Here, a new conceptually simple scheme was implemented in an updated Lagrange formulation. An appropriate decomposition of the deformation gradient results in constitutive relations defined in invariant tensors. Consistent tangent matrices are given for a linearly elastic fibre model and for a generalised anisotropic material. The simulations are robust, showing quadratic convergence for arbitrary degrees of anisotropy and arbitrary deformations with strain increments over 100%. Plasticity of the fibres is included without compromising the rate of convergence.



*This chapter has been published as: R.H.W. ten Thije, R. Akkerman and J. Huétink. Large deformation simulation of anisotropic material using an updated Lagrangian finite element method. *Computer Methods in Applied Mechanics and Engineering*, Volume 196, Issues 33-34, July 2007, Pages 3141-3150, with R.H.W. ten Thije as the principal author.

## 2.1 Introduction

Numerical optimization of products and production processes becomes increasingly important in the design phase of composite structures. It can reduce the time to market and can avoid the production of costly prototypes. Numerical simulations of the composite forming processes such as e.g. draping, rubber pressing or diaphragm forming are an essential part of these optimization tools if doubly curved products are considered. Redistribution of the fibres is then inevitable. The resulting fibre orientation is one of the most important parameters to control. These numerical simulations can also reveal problem areas where wrinkling or fibre buckling might occur.

There are two main approaches in composite forming simulations: the geometrical approach and the Finite Element (FE) approach. The fast and simple geometrical models are often sufficient for design purposes and date back to the fifties of the past century, where Mack and Taylor predicted the fibre distribution of a woven cloth on simple geometries based on a pin jointed net assumption [1]. Increasingly sophisticated models have been built ever since [2–4] and recently even interactive tools that allow the user to virtually manipulate woven fabrics have been developed [5].

FE simulations are capable of simulating the production process in great detail, including mechanisms such as tool-part friction, inter-ply friction, wrinkling and fibre bridging. One of the earliest elastic models was applied by Chen and Govindaraj in the mid nineties of the past century [6]. These FE simulations are however time consuming and often not very robust. Large deformation FE simulations of highly anisotropic material often show slow convergence or break down with increasing anisotropy and deformation.

The scale of anisotropy in metals is of a different order of magnitude compared to fibre reinforced composites, but recent developments point to the same imperfections in standard FE formulations in this field as well. Inclusion of yielding and plastic flow of anisotropic metals according to the Hill, Vegter or Barlat criteria [7–9] is a standard option in FE packages nowadays. Extension to large deformations and strains is however not straightforward. Bonet and Burton illustrated that the standard FE formulations are only valid for small or moderate strains [10]. Standard theories are based on the additive decomposition of the linear strain tensor, which can add up to significant deviations if the simulation is split into multiple steps. Inclusion of anisotropy is only straightforward if the additive structure is preserved according to Sansour and Bocko [11]. A formulation along this line can be

found in the work of Lu an Papadopoulos [12], who proposed a covariant formulation of anisotropic plasticity to circumvent problems associated with intermediate configurations that typically result from the small strain theory. It is worth noting at this point that the shortcomings of the small strain theory are independent of the fact that the material is anisotropic, but anisotropy makes the need for accurate descriptions at high strains more eminent or even inevitable.

Nedjar [13–15] and Huétink [16] proposed the use of multiplicative splits of the deformation tensors, which do not necessarily have to be equal for each material fraction. Huétink illustrated the straightforward implementation of fibrous materials in FE simulations by splitting the deformation tensor into a rotation part and a stretch part for each fibre fraction. Anisotropic materials can be efficiently and accurately modelled by implementing several material fractions into one element as shown by Hsiao and Kikuchi [17]. It results in a continuum material formulation with one or more axes of anisotropy. Huétink's approach allows for accurate tracking of multiple fibre directions in one continuum, whereas the use of a classic Green Naghdi or Jaumann approach would lead to poor results because the fibre direction is not exactly followed. These conclusions are stated by Boisse as well [18].

Accurate modelling of the fibre rotations with respect to the reference coordinate system is included in the viscous models of McEntee and ÓBrádaigh and Spencer [19, 20]. A different approach was adopted by Yu et al. Peng and Cao and Xue et al. by using non-orthogonal constitutive models [21–23]. A convected non-orthogonal coordinate system, whose in-plane axes coincides with the two fibre directions, is embedded in elements. The exactness of these models is often compromised on an implementation level where increments are linearised. FE formulations using a hybrid formulation automatically track the fibre direction. Bar or truss elements are coupled to displacement degrees of freedom of continuum elements and their orientation is therefore known exactly. This approach has been used by several researchers [24, 25] and was implemented as a standard option in the commercial FE programs Abaqus© and Msc Marc©.

### 2.1.1 Uniaxial tensile test

The following examples illustrate the difficulties when using a standard FE formulation to simulate deformations of highly anisotropic materials. An arbitrary commercial FE code, Ansys©, is used to simulate a simple tensile test with a ply of unidirectional fibres. The linear elastic material is highly

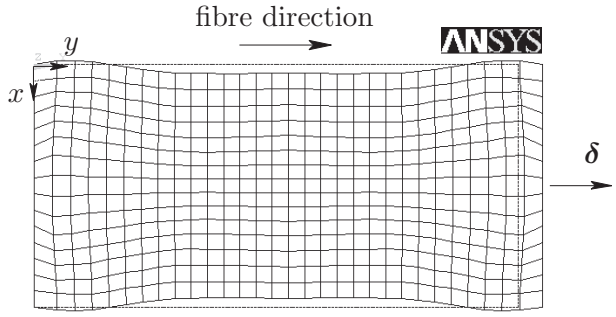


*Figure 2.1: Deformed shape of a tensile test simulation with a highly anisotropic material (scaled 250 times).*

anisotropic with a stiffness ratio of 1 to $10^5$. A mesh of 15 x 30 plane stress quadrilateral elements (PLANE42) is used. The left and right hand side are clamped and the right hand side moves in the $y$-direction as shown in figure 2.1. The incremental displacement $\delta$ is very small, only $5 \cdot 10^{-5}$ times the length of the specimen. Geometric nonlinearities are taken into account (NLGEOM,ON). Nevertheless, the simulation breaks down after only 4 steps at an elongation of only 0.02%. Figure 2.1 shows the last converged solution. The ply widens near the clamped edges, while it should contract due to Poisson's effect. Similar results are obtained with other FE codes. This phenomenon is caused by updating the material orientations using an incorrect geometry. The element strains $\boldsymbol{\varepsilon}$ are found by:

$$\{\boldsymbol{\varepsilon}\} = [\mathbf{B}] \cdot \{\mathbf{u}\} \tag{2.1}$$

where $[\mathbf{B}]$ contains the derivatives of the element shape functions and $\{\mathbf{u}\}$ denotes the nodal displacements. Implicit codes obtain the highest order of accuracy if $[\mathbf{B}]$ is evaluated on the intermediate geometry between the initial state and the current deformed state. The resulting stresses and subsequently the nodal forces become misaligned if the material orientation is updated using the same intermediate geometry, as illustrated in figure 2.2b. The top node of a single element is moved to the right. As the fibre is the only stress bearing material in the element, the resulting nodal force at the end of the step should be aligned with the new fibre direction. The orientation update should take place using the current geometry to avoid misalignment of the nodal forces in large deformation simulations with anisotropic material (figure 2.2c).

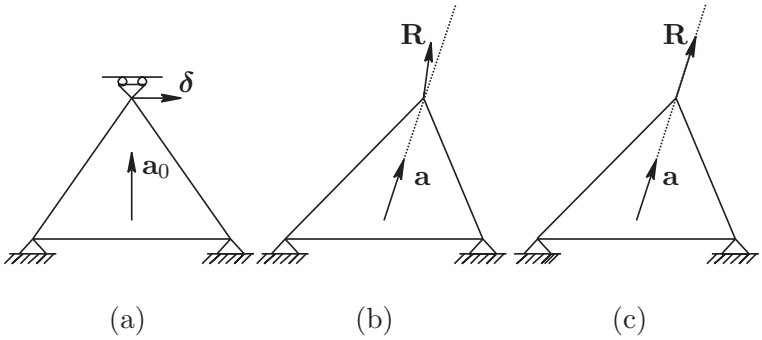


*Figure 2.2: Resulting (mis-) alignment of the nodal force. (a) initial geometry (b) nodal force R when using the intermediate geometry (c) nodal force R when using the final geometry.*

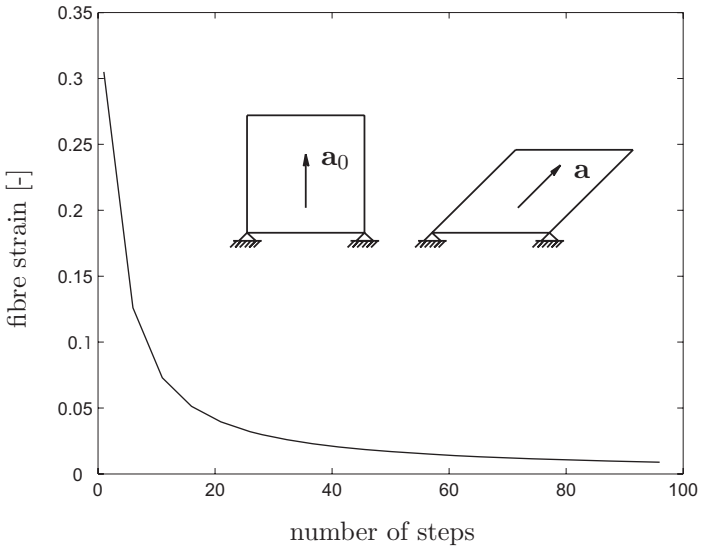


*Figure 2.3: Inaccurate fibre strain in pure shear.*

### 2.1.2 Pure shear

Incorrect deformed shapes can be avoided by evaluating the material tensor using the final geometry. Unfortunately this leads to less accurate strain predictions as shown in the next example. One element is sheared up to 75° as shown in figure 2.3. Applying pure shear should not introduce strains in the fibres which are aligned with the frame. The fibre strain is however as high as 30% if it is evaluated according to (2.1) and the deformation is applied in one

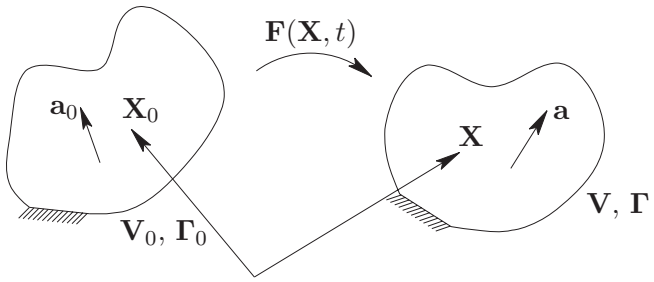


*Figure 2.4: Initial and current configuration of a body.*

step. Figure 2.3 shows that the accuracy improves if the total deformation is split into several steps, but this increases the calculation time significantly. As much as 86 steps are necessary to reduce the fibre strain below 1%.

The 'standard' large deformation simulations are based on the assumption that a large nonlinear displacement can be accurately approximated by multiple small steps in which a linear theory is applied. This assumption leads to poor performance in implicit FE simulations with (highly) anisotropic material. The previous examples illustrate that it leads to contradicting requirements as well. A review of the Finite Element formulation is necessary if large deformations of anisotropic material are considered.

## 2.2 Continuum mechanics

Continuum mechanics provides a mathematical description of motion and deformation of material in a reference system. It considers a body of a homogenous material which can be anisotropic.

### 2.2.1 Kinematics

The deformable body in figure 2.4 is located in space by the Lagrangian vector $\mathbf{X}$ at time $t$. The body has a volume $\mathbf{V}$ and a surface boundary $\mathbf{\Gamma}$. The location of the material particles in time is defined by the Eulerian location vector $x$, which is a function of $\mathbf{X}$ and $t$.

$$x = x(\mathbf{X}, t) \tag{2.2}$$

The deformation gradient $\mathbf{F}(\mathbf{X},\mathrm{t})$ maps the initial configuration onto the current configuration,

$$\mathbf{F}(\mathbf{X}, t) = \frac{\partial x}{\partial \mathbf{X}}|_t = x \overleftarrow{\nabla}_0 \tag{2.3}$$

and can be decomposed into a stretch tensor and a subsequent rotation or vice versa. The split is commonly performed using a polar decomposition and results in a symmetrical stretch tensor. An alternative decomposition is more convenient when considering anisotropic materials. The symmetry condition of the stretch tensor is abandoned. The deformation tensor is decomposed in a stretch tensor $\mathbf{G}$ and a subsequent rotation $\mathbf{R}$.

$$\mathbf{F} = \mathbf{R} \cdot \mathbf{G} \tag{2.4}$$

We are free to choose any orthonormal rotation tensor $\mathbf{R}$ such that the non symmetrical stretch tensor $\mathbf{G}$ is invariant under rigid body rotations. With the decomposition of (2.4), the velocity gradient $\mathbf{L}$ is written as:

$$\begin{aligned} \mathbf{L} &= \mathbf{v}\overleftarrow{\nabla} \\ &= \dot{\mathbf{F}} \cdot \mathbf{F}^{-1} \\ &= \dot{\mathbf{R}} \cdot \mathbf{R}^T + \mathbf{R} \cdot \dot{\mathbf{G}} \cdot \mathbf{G}^{-1} \cdot \mathbf{R}^T \end{aligned} \tag{2.5}$$

where $\mathbf{v}$ is the velocity. Introducing the tensors $\boldsymbol{\Omega}$ and $\mathbf{L}^G$ as:

$$\boldsymbol{\Omega} = \dot{\mathbf{R}} \cdot \mathbf{R}^T \tag{2.6}$$

$$\mathbf{L}^G = \dot{\mathbf{G}} \cdot \mathbf{G}^{-1} \tag{2.7}$$

the velocity gradient is split into the skew symmetric spin tensor $\boldsymbol{\Omega}$ and an invariant nonsymmetric rate of deformation tensor:

$$\mathbf{L} = \boldsymbol{\Omega} + \mathbf{R} \cdot \mathbf{L}^G \cdot \mathbf{R}^T \tag{2.8}$$

The tensor $\boldsymbol{\Omega}$ is equal to the spin tensor $\mathbf{W}$ if the stretch tensor is symmetric. The second term of (2.8) is then equal to the symmetric rate of deformation tensor $\mathbf{D}$,

$$\begin{aligned} \mathbf{L} &= \mathbf{W} + \mathbf{D} \\ &= \tfrac{1}{2}(\mathbf{v}\overleftarrow{\nabla} - \overrightarrow{\nabla}\mathbf{v}) + \tfrac{1}{2}(\mathbf{v}\overleftarrow{\nabla} + \overrightarrow{\nabla}\mathbf{v}) \end{aligned} \tag{2.9}$$

However, the decomposition of (2.4) does not necessarily result in a symmetric stretch tensor in which case $\boldsymbol{\Omega}$ and $\mathbf{W}$ will differ! This will be illustrated in section 2.4. The rate of rotation tensor $\dot{\mathbf{R}}$ is found by rewriting (2.5):

$$\begin{aligned} \dot{\mathbf{R}} &= \mathbf{L} \cdot \mathbf{R} - \mathbf{R} \cdot \dot{\mathbf{G}} \cdot \mathbf{G}^{-1} \\ &= \boldsymbol{\Omega} \cdot \mathbf{R} \end{aligned} \tag{2.10}$$

### 2.2.2 Stresses and strains

The local stress tensor $\boldsymbol{\tau}$ is introduced as:

$$\boldsymbol{\tau} = \mathbf{e}_i \cdot \tau_{ij} \cdot \mathbf{e}_j \tag{2.11}$$

with $\mathbf{e}_i$ and $\mathbf{e}_j$ the global base vectors. The local stress tensor $\boldsymbol{\tau}$ co-rotates with the rigid body rotations of the axes of anisotropy, which result from the decomposition (2.4). The stress tensor $\boldsymbol{\tau}$ is therefore invariant. It is related to the global Cauchy stress tensor $\boldsymbol{\sigma}$ by a rotation only,

$$\boldsymbol{\sigma} = \mathbf{R} \cdot \boldsymbol{\tau} \cdot \mathbf{R}^T \tag{2.12}$$

This approach was introduced by Huétink [16] and leads to a conceptually simple scheme for an updated or total Lagrange FE formulation for anisotropic materials. Nonlinearities due to reorientation of the material are taken into account when mapping the local stress tensor to the global Cauchy stress tensor. Constitutive laws can be written in terms of an invariant fourth order material tensor ${}^4\mathbf{E}$, where ${}^4\mathbf{E}$ is constant in case of elastic deformations. There is no need for non-orthogonal constitutive equations as introduced by Yu [21] and Xue [23].

The right and left Cauchy Green tensor, $\mathbf{C}$ and $\mathbf{B}$ respectively, are suitable strain definitions for large deformations. Both strain measures equal unity in case of rigid body rotations. Using the decomposition of (2.4), the strain definitions can be written as:

$$\mathbf{C} = \mathbf{F}^T \cdot \mathbf{F} = \mathbf{G}^T \cdot \mathbf{G} \tag{2.13}$$

$$\mathbf{B} = \mathbf{F} \cdot \mathbf{F}^T = \mathbf{R} \cdot \mathbf{G} \cdot \mathbf{G}^T \cdot \mathbf{R}^T \tag{2.14}$$

The rate of the right Cauchy Green tensor is related to the rate of deformation tensor $\mathbf{D}$ according to

$$\begin{aligned} \dot{\mathbf{C}} &= 2\mathbf{F}^T \cdot \mathbf{D} \cdot \mathbf{F} \\ &= 2\mathbf{G}^T \cdot \mathbf{R}^T \cdot \mathbf{D} \cdot \mathbf{R} \cdot \mathbf{G} \end{aligned} \tag{2.15}$$

The rate of the Cauchy stress (2.12) is related to the local stress and the local stress rate:

$$\dot{\boldsymbol{\sigma}} = \dot{\mathbf{R}} \cdot \boldsymbol{\tau} \cdot \mathbf{R}^T + \mathbf{R} \cdot \dot{\boldsymbol{\tau}} \cdot \mathbf{R}^T + \mathbf{R} \cdot \boldsymbol{\tau} \cdot \dot{\mathbf{R}}^T \tag{2.16}$$

### 2.2.3 Plasticity

The total deformation is split into an elastic reversible part and a plastic irreversible part

$$\mathbf{F} = \mathbf{R} \cdot \mathbf{G}_e \cdot \mathbf{G}_p \tag{2.17}$$

This results in a split of the velocity gradient $\mathbf{L}^G$ (2.7) in an elastic part $\mathbf{L}_e$ and plastic part $\mathbf{L}_p$

$$\mathbf{L}^G = \mathbf{L}_e + \mathbf{L}_p \tag{2.18}$$

with

$$\mathbf{L}_e = \dot{\mathbf{G}}_e \cdot \mathbf{G}_e^{-1} \tag{2.19}$$

$$\mathbf{L}_p = (\mathbf{G}_e \cdot {}^4\mathbf{I} \cdot \mathbf{G}_e^{-T}) : \dot{\mathbf{G}}_p \cdot \mathbf{G}_p^{-1} \tag{2.20}$$

where ${}^4\mathbf{I}$ is a fourth order tensor having the property ${}^4\mathbf{I} : \mathbf{A} = \mathbf{A}$, where $\mathbf{A}$ is an arbitrary second order tensor. Constitutive laws provide the additional equations to determine the quantitative split of the total deformation.

### 2.2.4 Free energy and stress

Constitutive equations can be successfully derived using the Helmholtz free energy, see e.g. Akkerman [26]. The starting point is some form of the Second Law of thermodynamics. There are no restrictions for the material response at large deformations, but the response at small deformations must coincide with the linear theory, see Huétink [27]. Huétink [16] showed that the free energy can be expressed as an invariant function of $\mathbf{C}$ only in case of anisotropy, whereas that is not possible for the left Cauchy Green tensor $\mathbf{B}$. The free energy would then be a function of the tensor $\mathbf{R}$ as well. This makes it more complicated to derive constitutive equations from free energy functions. Therefore $\psi$ is regarded as a function of the elastic strain tensor $\mathbf{C}_e$.

$$\psi = \psi(\mathbf{C}_e) \tag{2.21}$$

The local stress tensor is derived from the free energy (*Huétink [16]*):

$$\boldsymbol{\tau} = 2\rho \mathbf{G}_e \cdot \frac{\partial \psi}{\partial \mathbf{C}_e} \cdot \mathbf{G}_e^T \tag{2.22}$$

## 2.3 Finite Element formulation

The strong form of mechanical equilibrium without the presence of body forces and boundary traction is formulated as:

$$\boldsymbol{\sigma} \cdot \overleftarrow{\nabla} = \mathbf{0} \tag{2.23}$$

Following the standard procedure of weighing, applying reduced integration and the divergence theorem of Gauss, the weak form of (2.23) becomes:

$$\int_V \mathbf{w}\overleftarrow{\nabla} : \boldsymbol{\sigma}\, dV = \int_\Gamma \mathbf{w}\cdot\mathbf{t}\, d\Gamma \tag{2.24}$$

where $\mathbf{w}$ are the weight functions and $\mathbf{t}$ is the traction on the boundary surface. The rate form of this equation in the current configuration is found to be

$$\int_V \left(\mathbf{w}\overleftarrow{\nabla} : \dot{\boldsymbol{\sigma}} - \mathbf{w}\overleftarrow{\nabla}\cdot\mathbf{v}\overleftarrow{\nabla} : \boldsymbol{\sigma} + \mathbf{w}\overleftarrow{\nabla} : \boldsymbol{\sigma}\tfrac{j}{J}\right) dV = \int_\Gamma \mathbf{w}\cdot\dot{\mathbf{t}}\, d\Gamma \tag{2.25}$$

where $J$ denotes the Jacobian, the volume ratio:

$$J = det(\mathbf{F}) = \frac{dV}{dV_0} \tag{2.26}$$

Equation (2.25) is used to find consistent tangent matrices for the FE calculations.

## 2.4 Fibre reinforced material

Section 2.2.1 stated the freedom of choice for the decomposition of the deformation tensor $\mathbf{F}$ in a stretch tensor $\mathbf{G}$ and a subsequent rotation $\mathbf{R}$. The mapping of the initial fibre $\mathbf{a}_0$ onto its current state $\mathbf{a}$ is given by:

$$\begin{aligned}\mathbf{a} &= \mathbf{F}\cdot\mathbf{a}_0 \\ &= \mathbf{R}\cdot\mathbf{G}\cdot\mathbf{a}_0\end{aligned} \tag{2.27}$$

In case of uniaxial fibres it is convenient to take a rotation $\mathbf{R}$ that rotates the initial fibre direction $\mathbf{a}_0$ towards the current fibre direction $\mathbf{a}$:

$$\mathbf{R}\cdot\mathbf{a}_0 = \frac{\ell_0}{\ell}\mathbf{a} \tag{2.28}$$

The non-symmetrical tensor $\mathbf{G}$ now relates the current length $\ell$ to the initial length $\ell_0$:

$$\mathbf{G}\cdot\mathbf{a}_0 = \frac{\ell}{\ell_0}\mathbf{a}_0 \tag{2.29}$$

The fibres are assumed to be linearly elastic. The scalar fibre strain is defined as:

$$\varepsilon = \tfrac{1}{2}\frac{\ell^2 - \ell_0^2}{\ell_0^2} \tag{2.30}$$

or using the right Cauchy Green tensor:

$$\varepsilon = \tfrac{1}{2}\mathbf{a}_0\mathbf{a}_0 : (\mathbf{C}_e - \mathbf{I})/\ell_0^2 \tag{2.31}$$

The resulting free energy function per unit mass equals the elastically stored energy.

$$\begin{aligned}\psi &= \frac{1}{2\rho}E_f\varepsilon^2 \\ &= \frac{E_f}{8\rho_0\ell_0^4}(\mathbf{C}_e - \mathbf{I}) : \mathbf{a}_0\mathbf{a}_0\mathbf{a}_0\mathbf{a}_0 : (\mathbf{C}_e - \mathbf{I})\end{aligned} \tag{2.32}$$

Using (2.22), the invariant stress $\boldsymbol{\tau}$ is found to be

$$\boldsymbol{\tau} = \frac{\rho E_f \ell^2}{2\rho_0\ell_0^6}\mathbf{a}_0\mathbf{a}_0\mathbf{a}_0\mathbf{a}_0 : (\mathbf{C}_e - \mathbf{I}) \tag{2.33}$$

and the Cauchy stress tensor:

$$\boldsymbol{\sigma} = \frac{\rho E_f}{2\rho_0\ell_0^4}\mathbf{a}\mathbf{a}\mathbf{a}_0\mathbf{a}_0 : (\mathbf{C}_e - \mathbf{I}) \tag{2.34}$$

### 2.4.1 Consistent tangent

The performance of implicit FE simulations depends largely on the consistency of the tangent (stiffness) matrix when using a Newton-Raphson procedure. The iterative process converges very slowly or even diverges if not all the nonlinearities are taken into account, especially when it concerns highly anisotropic materials.
The local stress rate is found by differentiating (2.33) with respect to time.

$$\dot{\boldsymbol{\tau}} = \frac{\rho E_f \ell^2}{2\rho_0\ell_0^6}\,\mathbf{a}_0\mathbf{a}_0\mathbf{a}_0\mathbf{a}_0 : \dot{\mathbf{C}}_e + \boldsymbol{\tau}(2\frac{\dot{\ell}}{\ell} + \frac{\dot{\rho}}{\rho}) \tag{2.35}$$

The rate of rotation tensor $\dot{\mathbf{R}}$ results from combining (2.28), (2.29) and (2.10):

$$\dot{\mathbf{R}} = \mathbf{L}\cdot\mathbf{R} - \frac{\dot{\ell}}{\ell}\mathbf{R} \tag{2.36}$$

Conservation of mass can be expressed as:

$$\rho J = c \tag{2.37}$$

This results in the following relation for the rates:

$$\frac{\dot{\rho}}{\rho} = -\frac{\dot{J}}{J} \tag{2.38}$$

Equations (2.33), (2.35), (2.36) and (2.12) are now used to express the rate of the Cauchy stress (2.16). This rate is used in (2.25) and with (2.38) it results in the following consistent tangent matrix for the uniaxial fibre model:

$$K = \int_V \left[ \frac{\rho E_f}{\rho_0 \ell_0^4} \cdot \left( \tfrac{1}{2}(\mathbf{w}\overleftarrow{\nabla} + \overrightarrow{\nabla}\mathbf{w}) \cdot \mathbf{aa} \right) : \left( \mathbf{aa} \cdot \tfrac{1}{2}(\mathbf{v}\overleftarrow{\nabla} + \overrightarrow{\nabla}\mathbf{v}) \right) + \overrightarrow{\nabla}\mathbf{w} \cdot \mathbf{v}\overleftarrow{\nabla} : \boldsymbol{\sigma} \right] dV \tag{2.39}$$

Details on the uni-axial fibre model are presented in appendix C.

## 2.5 General elastic anisotropy

The free energy function $\psi$ of the uniaxial fibre model (2.32) is extended to the arbitrary anisotropic case:

$$\psi = \frac{1}{8\rho_0}(\mathbf{C}_e - \mathbf{I}) : {}^4\mathbf{E} : (\mathbf{C}_e - \mathbf{I}) \tag{2.40}$$

with ${}^4\mathbf{E}$ the invariant and constant fourth order material tensor. Using (2.22), the invariant stress $\boldsymbol{\tau}$ for the generalised anisotropic model is:

$$\boldsymbol{\tau} = \frac{\rho}{2\rho_0}(\mathbf{G}_e \cdot {}^4\mathbf{I} \cdot \mathbf{G}_e) : {}^4\mathbf{E} : (\mathbf{C}_e - \mathbf{I}) \tag{2.41}$$

### 2.5.1 Consistent tangent

The rate of the local stress tensor (2.41) is given by:

$$\dot{\boldsymbol{\tau}} = \frac{\dot{\rho}}{\rho}\boldsymbol{\tau} + {}^4\mathbf{E}^* : \mathbf{L}_e \tag{2.42}$$

with

$${}^4\mathbf{E}^* = 4\frac{\rho}{\rho_0}(\mathbf{G}_e \cdot {}^4\mathbf{I} \cdot \mathbf{G}_e) : {}^4\mathbf{E} : (\mathbf{G}_e^T \cdot {}^4\mathbf{I} \cdot \mathbf{G}_e^T) + {}^4\mathbf{I} \cdot \boldsymbol{\tau} + \boldsymbol{\tau} \cdot {}^4\mathbf{I} \tag{2.43}$$

Since ${}^4\mathbf{E}^*$ is symmetric, the skewsymmetric components of $\mathbf{L}_e$ in (2.42) will vanish. The nonsymmetric tensor $\mathbf{L}_e$ can be replaced by its symmetric part, an invariant rate of deformation tensor $\mathbf{d}_e$:

$$\begin{aligned} \mathbf{d}_e &= \tfrac{1}{2}(\mathbf{L}_e + \mathbf{L}_e^T) \\ &= \mathbf{R}^T \cdot \mathbf{D} \cdot \mathbf{R} \end{aligned} \tag{2.44}$$

The local stress rate can therefore be written as:

$$\dot{\boldsymbol{\tau}} = \frac{\dot{\rho}}{\rho}\boldsymbol{\tau} + {}^4\mathbf{E}^* : \mathbf{d}_e \tag{2.45}$$

Analogous to the procedure in section 2.4.1, equations (2.41), (2.45), (2.10) and (2.12) are now used to express the rate of the Cauchy stress (2.16). This rate is used in (2.25) and with (2.38) it results in the following consistent tangent matrix for the generalised anisotropic model:

$$K = \int_V \left[ \frac{\rho}{\rho_0} \cdot \tfrac{1}{2}(\mathbf{w}\overleftarrow{\nabla} + \overrightarrow{\nabla}\mathbf{w}) : \left(\mathbf{F} \cdot {}^4\mathbf{I} \cdot \mathbf{F}\right) : {}^4\mathbf{E} : \right. \tag{2.46}$$
$$\left. \left(\mathbf{F}^T \cdot {}^4\mathbf{I} \cdot \mathbf{F}^T\right) : \tfrac{1}{2}\left(\mathbf{v}\overleftarrow{\nabla} + \overrightarrow{\nabla}\mathbf{v}\right) + \overrightarrow{\nabla}\mathbf{w} \cdot \mathbf{v}\overleftarrow{\nabla} : \boldsymbol{\sigma} \right] dV$$

Details on the generalised elastic anisotropic material model are presented in appendix E.

## 2.6 Application

The large deformation finite element formulation has been implemented in MATLAB© to examine the performance. Multiple convergence and accuracy tests were performed. The uniaxial tensile test example discussed in the introduction does not show unrealistic shapes anymore due to the correct update of the fibre direction. The fibre strain in the shear test example is now accurately predicted, independent of the number of steps or the size of the displacement increments. Two additional examples including plasticity will be discussed here: the bias extension experiment and the pressurisation of a McKibben actuator.

### 2.6.1 Bias extension

The bias extension experiment is frequently used to examine the shear response of biaxial reinforced materials. Figure 2.5 shows the undeformed and the deformed shape of the material. The two fibre directions are initially perpendicular to each other at $\pm 45°$. The specimen is gripped on the short edges and elongated in the $0°$ direction. The stiffness of the fibres is dominant and the specimen deforms as a trellis frame, with each fibre crossing acting as a possible hinge point. Three deformation regions develop: an undeformed region, a central region with pure shear and a region with intermediate shear. Potter presented an extensive discussion of the bias extension experiment in [28].

The fabric is 70 mm wide, 210 mm long and has a thickness of 1 mm. It is meshed using 300 two-dimensional plane stress simplex triangles. Several material fractions are combined within one element in these simulations. The

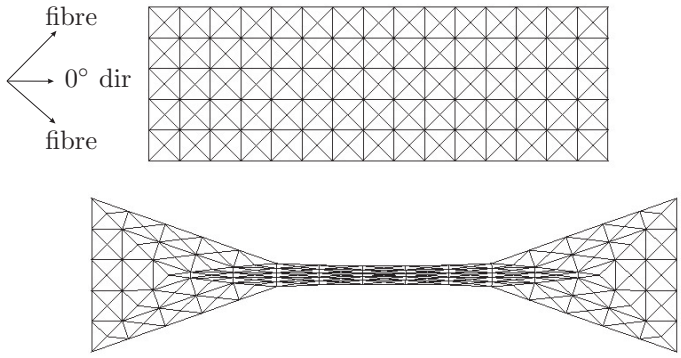


*Figure 2.5: The undeformed and deformed shape of the bias extension simulation (no displacement scaling).*

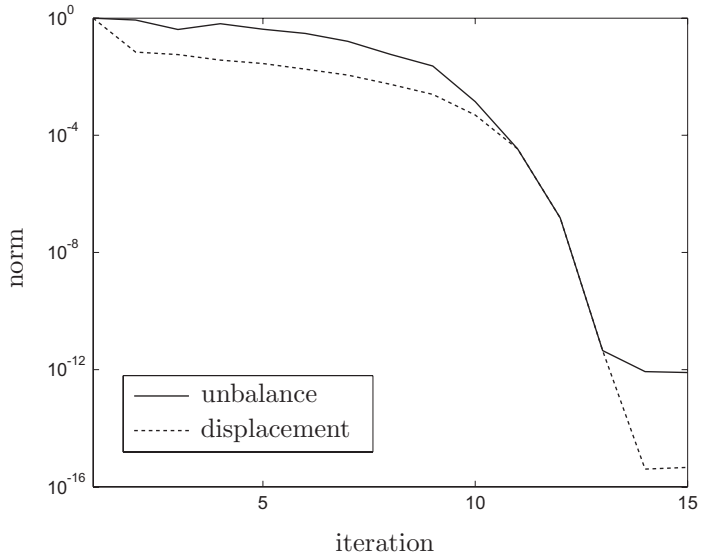


*Figure 2.6: Convergence plot of the one-step bias extension simulation.*

deformation is equal for each fraction and each fraction contributes to the total stress proportional to its volume fraction $\nu$:

$$\boldsymbol{\sigma} = \Sigma_i \nu_i \boldsymbol{\sigma}_i \tag{2.47}$$

where $i$ denotes the fraction number. The biaxial material is represented by an elastic isotropic bulk fraction and two fibre fractions, with a Young's modulus

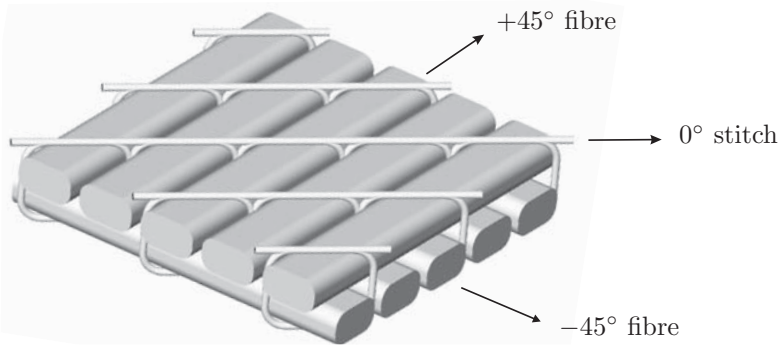


*Figure 2.7: Idealised model of a biaxial non crimp fabric: two fibre layers and a stitching thread.*

1.0 GPa and $1.0{\cdot}10^3$ GPa respectively. The deformation shown in figure 2.5 is applied in only one step, which is a good performance for an FE code. Figure 2.6 shows the convergence behaviour of this simulation. The unbalance norm $\epsilon_u$ and the displacement norm $\epsilon_d$ are given by:

$$\epsilon_u = \frac{\|R - F\|}{\|R\|} \qquad \epsilon_d = \frac{\|\triangle u\|}{\|u\|} \tag{2.48}$$

where $R$ are the reaction forces, $F$ the applied nodal loads, $\triangle u$ the displacement found during the iteration and $u$ the total displacement. The simulation initially converges slowly, due to strain increments over 100% and fibre rotations up to 45°. After 8 iterations it shows quadratic convergence. All individual steps converge to machine precision within 6 iterations if the simulation is split into more than 3 steps, showing quadratic convergence from the first iteration onwards.

Another large advantage of the nonlinear Cauchy Green strain definition is the increased robustness of the simulation when using poorly shaped elements. Figure 2.5 shows elements with angles below 2°, but the simulation can be continued with another step without problems.

### Plasticity and rigid rotations

Non crimp fabrics (NCF) consist of separate fibre layers which are stitched together with a stitching thread. This thread is often made from polyester. An idealised model of the biaxial NCF is found in figure 2.7. The two fibre layers are orientated in the ±45° direction and the stitching thread is orientated in the 0° direction. The stitch can deform plastically. A bias extension

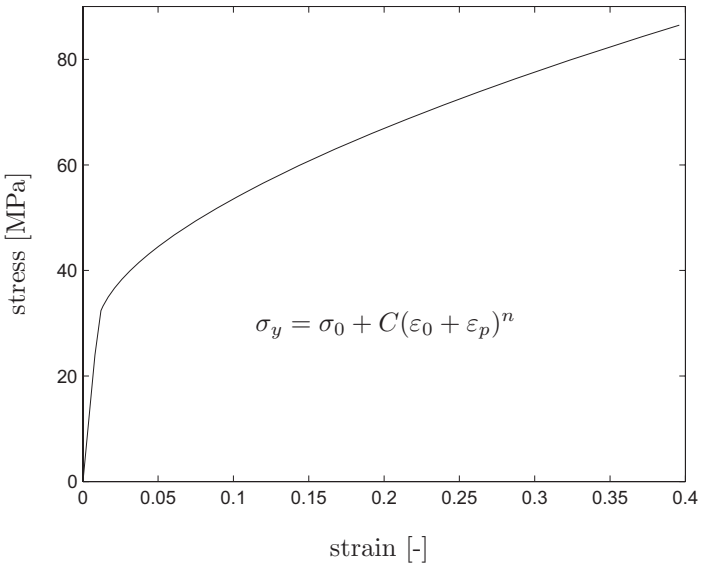


*Figure 2.8: Stress strain curve of a polyester stitching thread with Nadai hardening. Young's modulus = 3.0 GPa, $\sigma_0$ = 30 MPa, C = 100 MPa, $\varepsilon_0$ = $5{\cdot}10^{-5}$, n = 0.6*

experiment as illustrated in figure 2.5 is no longer dominated by the shear response of the fabric, but by the response of the stitch thread. The thread is included in the simulation by an additional fibre fraction that can deform plastically according to the Nadai stress-strain curve shown in figure 2.8. The stitch responds elastically up to the yielding point and then follows the yield surface given by the yield stress $\sigma_y$:

$$\sigma_y = \sigma_0 + C(\varepsilon_0 + \varepsilon_p)^n \tag{2.49}$$

where $\sigma_0$, $C$, $\varepsilon_0$ and $n$ are material parameters and $\varepsilon_p$ denotes the plastic strain in the stitch material. The soft stitch material has been modelled using the following values: Young's modulus = 3.0 GPa, $\sigma_0$ = 30 MPa, C = 100 MPa, $\varepsilon_0 = 5{\cdot}10^{-5}$ and $n = 0.6$.

The fabric is simultaneously rotated by 90° during the extension to illustrate the performance of the code under large rigid body rotations. Figure 2.9 shows the deformed shape of the specimen. The colours indicate the plastic strain in the stitches, going up to 40%. The total deformation and rotation is applied in two steps and the individual steps converged to machine precision within 8 iterations. This illustrates that the formulation works very well for large deformations and rotations including plasticity as well. Details on the elasto-plastic uni-axial fibre model are presented in appendix D.

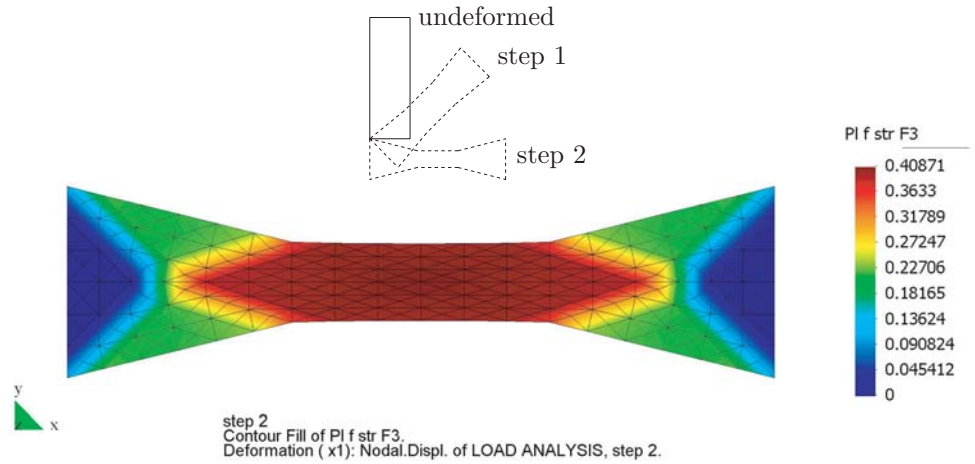


*Figure 2.9: Plastic strain in the polyester stitching thread during a bias extension and simultaneous rotation of a non crimp fabric.*

### 2.6.2 McKibben actuator

The McKibben actuator is a pneumatic actuator with a high power to weight ratio and used as an artificial muscle or as an actuator in mobile robots. It consists of a inner bladder made of a flexible material, covered by a braided shell with two fibre families. These fibres families have an equal but opposite angle with respect to the longitudinal axis. The actuator expands radially if it is pressurised and contracts or expands longitudinally, depending on the initial orientation of the fibres. The angle of the fibres with respect to the longitudinal axis will approach the theoretical limit of 54,4° at infinite pressure, based on the stress distribution in longitudinal and circumferential direction of a thin pressurised vessel covered with inextensible fibres. This implies that actuators with initial fibre angles below 54,4° will contract during pressurisation, respectively expand for angles above 54,4°.

Experimental and mathematical analyses of actuators made from natural latex rubber bladders and polyester braids were conducted by Klute in 2000 [29]. One of his experiments has been simulated in a three dimensional simulation. Figure 2.10 shows the actuator at ambient pressure and at a pressure of 21.5 bars. The initial length, radius and thickness of the actuator are respectively 264.0 mm, 8.7 mm and 2.4 mm. The end caps are considered to be rigid. The initial fibre angle with respect to the longitudinal axis is 17.69°. The actuator is meshed with 2480 plane stress triangular membrane elements and loaded with an uniform pressure from the inside. The bladder

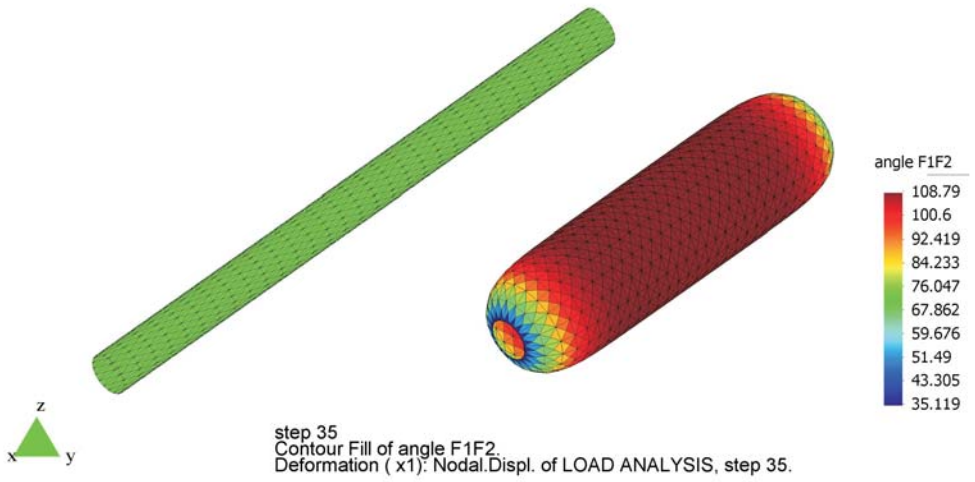


*Figure 2.10: A McKibben actuator at ambient pressure and at 21.5 bars.*

material is modelled using a Mooney-Rivlin material model in which the stored strain energy $W$ can be expressed as:

$$W = \sum_{i=0,j=0}^{n} C_{ij}(I_1 - 3)^i(I_2 - 3)^j \tag{2.50}$$

where $C_{ij}$ are empirical constants and $I_1$ and $I_2$ are the strain invariants of the left Cauchy strain tensor $\mathbf{B}$. Details on the Mooney-Rivlin material model are presented in appendix F. Two constants are sufficient to model the bladder material accurately and are given by Klute: $C_{10}$=118.4 kPa and $C_{01}$=105.7 kPa. Klute considered the fibres to be inextensible, a condition that is imposed by setting the Young's modulus of the fibres to 100 GPa. This result in a stiffness ratio between the two material fractions of approximately $10^6$, causing the system to be ill conditioned with condition numbers around $10^7$. In spite of the large condition numbers, the simulation runs without adding inertia effects. Inertia effects have a positive effect on the stability and speed of the simulation as mentioned in the research of Meinders et al. [30].

The actuator is pressurised up to 100 bars in 40 steps. Figure 2.10 shows the pressurised actuator at its minimal length at a pressure of 21.5 bars. The plot shows the angle between the two fibre families, which is twice the angle with respect to the longitudinal axis. The angle approaches the theoretical limit discussed before. The actuator expands radially and longitudinally if the pressure is increased above 21.5 bars, while the angle remains constant.

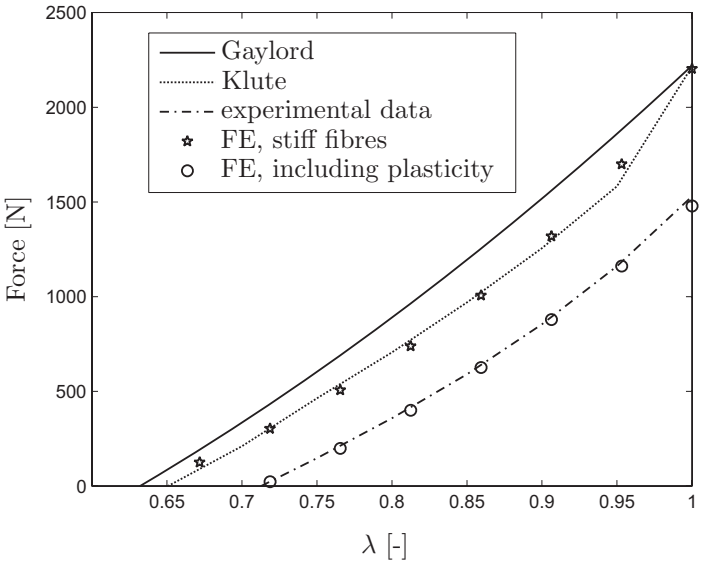


*Figure 2.11: Actuator force at a pressure of 5 bars.*

Analytical expressions for actuator forces at different contraction ratios were given by Gaylord in 1958 [31]. Gaylord assumed inextensible fibres and neglected the membrane deformations of the inflated bladder. The model results in a theoretical upper bound. Klute developed a non-linear model that incorporates the membrane deformations of a Mooney-Rivlin bladder material as well. The results from both analytical models and the FE results are plotted in figure 2.11 for this specific actuator at a pressure of 5 bars. The contraction ratio $\lambda$ is defined as the ratio between the current length and the length at ambient pressure: $\lambda = L/L_0$. The FE model shows good agreement with the model developed by Klute, although deviations with the experimental results are still significant. This can be due to elastic and/or plastic strain in the fibres. The braid manufacturer (Alpha Wire Company) kindly supplied further details on the reinforcement used. The GRP-110-1-1/4 braid consists of thermoplastic polyester fibres and has a linear density of 24 g/m. The polyester has a density of 1340 kg/m$^3$. These values result in fibre stresses between 140 and 150 MPa, well above the elastic region of polyester. The simulation has been rerun including fibre plasticity and a hardening law according to Nadai: Young's modulus = 3.5 GPa, $\sigma_0$ = 70 MPa, C = 350 MPa, $\varepsilon_0 = 5{\cdot}10^{-5}$ and $n$ = 0.6. The fibres start yielding when the pressure exceeds 2.5 bar. Figure 2.12 shows the plastic fibre strain distribution along the actuator at a pressure of 5 bars. The permanent plastic strain in the fibre reduces the actuator force and the force now corresponds

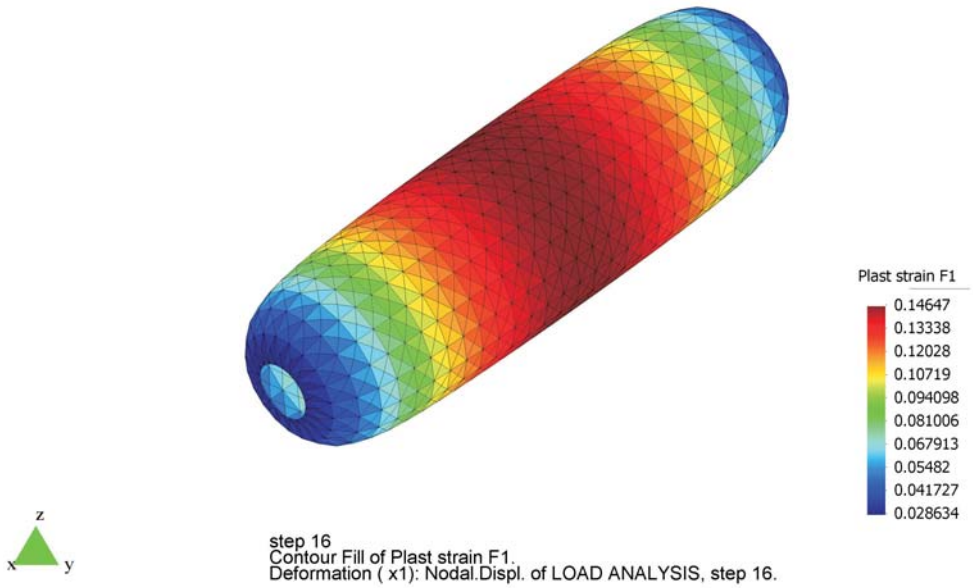


*Figure 2.12: Total plastic fibre strain at a pressure of 5 bars.*

to the experimental results as shown in figure 2.11. Accurate stress strain curves for this material should be obtained to validate the hypotheses of fibre yielding at these pressure levels. This example illustrates that the method works properly for 3D membrane elements with in and out-of-plane loading including plastically deformable fibres. The simulations are robust and show quadratic convergence, provided the pressure boundary condition is linearised consistently. This linearisation is presented in appendix G.

## 2.7 Numerical issues

Figure 2.6 shows a displacement norm that reduces to machine precision. The unbalance norm remains $10^3$ times higher. This is due to the condition of the system. The fibre stiffness is $10^3$ times higher than the bulk stiffness, causing unbalances in the same order of magnitude.

Care should also be taken when storing the deformation gradient $\mathbf{F}$. Large rounding errors can occur if deformations are small and the deformation gradient and the right Cauchy Green strain tensor are close to unity. Significant digits are lost when the local stress $\boldsymbol{\tau}$ is evaluated (2.41), due

to the subtraction of the unit tensor **I**. This can be solved by writing:

$$\mathbf{F} = \mathbf{I} + \delta\mathbf{F} \tag{2.51}$$

Storing $\delta\mathbf{F}$ instead of $\mathbf{F}$ and rewriting the strain definition in terms of $\delta\mathbf{F}$ avoids the large numerical rounding errors if small deformations are applied.

A shell or membrane formulation is commonly used in forming simulations of thin sheet materials, the so called 2.5-dimensional case. Strain in the out-of-plane direction is evaluated using constitutive equations and assuming plane stress conditions. Equations (2.39) and (2.46) show that the tangent stiffness matrices are generally symmetric, but in the 2.5 dimensional case this is only true if the volume or the thickness is assumed to be constant. Other assumptions will result in a non-symmetrical tangent matrix.

## 2.8 Conclusions

The standard finite element codes are not very suitable for large deformation simulations of highly anisotropic materials. It leads to confusing formulations as well. To avoid misalignment of the nodal forces, the material axes of anisotropy should be evaluated on the final geometry. However, this causes the accuracy of the strain prediction to drop significantly. Instead, the deformation gradient should be decomposed into a rotation tensor and a stretch tensor. The rotation reflects the rotation of the axes of anisotropy. This is an advantage when modelling fibre reinforced composites. Stresses are computed using invariant local stress and stiffness tensors. This leads to a simple and straightforward implementation of constitutive laws, which do not have to account for any rotation of the material. Consistent tangent matrices were presented for linearly elastic fibres and for a generalised anisotropic material. The scheme was implemented and tested in 2D and 3D simulations, including plasticity and large rigid rotations. The simulations converge quadratically for arbitrary deformation gradients and arbitrary degrees of anisotropy. The simulations are more robust than the standard implementations. Poorly shaped elements behave significantly better when using the right Cauchy Green strain definition instead of a linear strain definition.

## Bibliography

[1] C. Mack and H. Taylor. 'The fitting of woven cloth to surfaces'. *J Text I*, 47:477–487, 1956.

[2] P. Potluri, S. Sharma and R. Ramgulam. 'Comprehensive drape modelling for moulding 3D textile preforms'. *Compos Part A-Appl S*, 32:1415–1424, 2001.

[3] M. Aono, D. E. Breen and M. J. Wozny. 'Modeling methods for the design of 3D broadcloth composite parts'. *Comput Aided Design*, 33:989–1007, 2001.

[4] S. G. Hancock and K. D. Potter. 'The use of kinematic drape modelling to inform the hand lay-up of complex composite components using woven reinforcements'. *Compos Part A-Appl S*, 37:413–422, 2006.

[5] S. G. Hancock and K. D. Potter. 'Virtual Fabric Placement - A new strategy for simultaneous preform design, process visualisation and production of manufacturing instructions for woven composite components'. In *Proc 9th Int ESAFORM Conf*, pages 727–730. Publishing House Akapit, Krakow, Poland, 2006, 2006. ISBN 83-89541-66-1.

[6] B. Chen and M. Govindaraj. 'A physically based model of fabric drape using flexible shell theory'. *Text Res J*, 65:324–330, 1995.

[7] R. Hill. 'A theory of the yielding and plastic flow of anisotropic metals'. *Proceedings of the Royal Society of London*, 193:281–297, 1948.

[8] H. Vegter and A. H. van den Boogaard. 'A plane stress yield function for anisotropic sheet material by interpolation of biaxial stress states'. *Int J Plasticity*, 22:557–580, 2006.

[9] F. Barlat, D. J. Lege and J. C. Brem. 'A Six Component Yield Function for Anisotropic Materials'. *Int J Plasticity*, 7:693–712, 1991.

[10] J. Bonet and A. J. Burton. 'A simple orthotropic, transversely isotropic hyperelastic constitutive equation for large strain computations'. *Comput Method Appl M*, 162:151–164, 1998.

[11] C. Sansour and J. Bocko. 'On the numerical implications of multiplicative inelasticity with an anisotropic elastic constitutive law'. *Int J Numer Meth Eng*, 58:2131–2160, 2003.

[12] J. Lu and P. Papadopoulos. 'A covariant formulation of anisotropic finite plasticity: theoretical developments'. *Comput Method Appl M*, 193:5339–5358, 2004.

[13] B. Nedjar. 'Frameworks for finite strain viscoelastic-plasticity based on multiplicative decompositions. Part I: Continuum formulations'. *Comput Method Appl M*, 191:1541–1562, 2002.

[14] B. Nedjar. 'Frameworks for finite strain viscoelastic-plasticity based on multiplicative decompositions. Part II: Computational aspects'. *Comput Method Appl M*, 191:1563–1593, 2002.

[15] B. Nedjar. 'An anisotropic viscoelastic fibrematrix model at finite strains: Continuum formulation and computational aspects'. *Comput Method Appl M*, 196:1745–1756, 2007.

[16] J. Huétink. 'On Anisotropy, Objectivity and Invariancy in finite thermo-mechanical deformations'. In *Proc 9th Int ESAFORM Conf*, pages 355–358. Publishing House Akapit, Krakow, Poland, 2006, 2006. ISBN 83-89541-66-1.

[17] S.-W. Hsiao and N. Kikuchi. 'Numerical analysis and optimal design of composite thermoforming process'. *Comput Method Appl M*, 177:1–34, 1999.

[18] P. Boisse. 'Meso-macro approach for composites forming simulation'. *J Mater Sci*, 41:6591–6598, 2006.

[19] S. P. McEntee and C. M. ÓBrádaigh. 'Large deformation finite element modelling of single-curvature composite sheet forming with tool contact'. *Compos Part A-Appl S*, 29:207–213, 1998.

[20] A. Spencer. 'Theory of fabric-reinforced viscous fluids'. *Compos Part A-Appl S*, 31:1311–1321, 2000.

[21] W.-R. Yu, P. Harrison and A. Long. 'Finite element forming simulation for non-crimp fabrics using a non-orthogonal constitutive equation'. *Compos Part A-Appl S*, 36:1079–1093, 2005.

[22] X. Peng and J. Cao. 'A continuum mechanics-based non-orthogonal constitutive model for woven composite fabrics'. *Compos Part A-Appl S*, 36:859–874, 2005.

[23] P. Xue, X. Peng and J. Cao. 'Non-orthogonal constitutive model for characterizing woven composites'. *Compos Part A-Appl S*, 34:183–193, 2003.

[24] S. Reese. 'Meso-macro modelling of fibre-reinforced rubber-like composites exhibiting large elastoplastic deformation'. *Int J Solids Struct*, 40:951–980, 2003.

[25] S. B. Sharma and M. P. F. Sutcliffe. 'A simplified finite element model for draping of woven material'. *Compos Part A-Appl S*, 35:637–643, 2004.

[26] R. Akkerman. *Euler-Lagrange simulations of nonisothermal viscoelastic flows*. Ph.D. thesis, University of Twente, the Netherlands, 1993. ISBN 90-9006764-7.

[27] J. Huétink. *On the simulation of thermo-mechanical forming processes*. Ph.D. thesis, University of Twente, the Netherlands, 1986. URL www.dieka.org.

[28] K. Potter. 'Bias extension measurements on cross-plied unidirectional prepreg'. *Compos Part A-Appl S*, 33:63–73, 2002.

[29] G. K. Klute and B. Hannaford. 'Accounting for Elastic Energy Storage in McKibben Artificial Muscle Actuators'. *J Dyn Syst-T ASME*, 122:386–388, 2000.

[30] T. Meinders, A. H. van den Boogaard and J. Huétink. 'Improvement of implicit finite element code performance in deep drawing simulations by

dynamics contributions'. *J Mater Process Tech*, 134:413–420, 2003.

[31] R. H. Gaylord. 'Fluid actuated motor system and stroking device'. U.S. Patent 2,844,126, July 22 1958.

# Chapter 3

# Solutions to intra-ply shear locking in finite element analyses of fibre reinforced materials*


## Abstract

Intra-ply shear locking results in unrealistic fibre stresses and spurious wrinkling in composite forming simulations. Three remedies were investigated: aligning the mesh, applying reduced integration and using multi-field elements. Several triangular and quadrilateral elements were tested on their capability to avoid locking in a two-dimensional bias extension simulation. The resulting locking-free elements were tested in a realistic three-dimensional drape simulation of a biaxial fabric as well. The new triangular multi-field element seems to be the best locking-free element for unaligned meshes. It has a semi-quadratic in-plane and a linear out-of-plane displacement field. This combination improves the accuracy of the element and avoids contact problems in 3D simulations.


*This chapter is based on: R.H.W. ten Thije and R. Akkerman. Solutions to intra-ply shear locking in finite element analyses of fibre reinforced materials. *Manuscript submitted to Composites Part A: Applied Science and Manufacturing*, with R.H.W. ten Thije as the principal author

## 3.1 Introduction

Manufacturing processes can lead to unacceptable shape distortions in fibre reinforced products. Thin walled three dimensional products exhibiting double curvature are especially susceptible to springback, wrinkling or inefficient fibre distribution upon forming. These distortions depend on a wide variety of parameters, of which geometry, material properties, lay-up, process temperatures and friction are just a few important ones. Numerical tools are powerful instruments to analyse the distortions in the design phase and can ideally lead to a first-time-right design. There are two main approaches to composite forming simulations: the geometrical approach and the Finite Element (FE) approach. The fast and simple geometrical models are often sufficient for design purposes and date back to the 1950s, when Mack and Taylor predicted the fibre distribution of a woven cloth on simple geometries based on a pin jointed net assumption [1]. Increasingly advanced models have been built ever since [2–4] and recently even interactive tools that allow the user to manipulate woven fabrics in a virtual environment have been developed [5]. Constitutive properties have been added [6], but geometrical models remain restricted to very simple material models and geometrical boundary conditions.

FE simulations are significantly slower than geometric models, but are capable of simulating the production process in more detail. Complex constitutive behaviour and boundary conditions, like friction or tool temperatures, can be included. This makes FE simulations applicable for predicting phenomena like springback, wrinkling or fibre bridging. One of the earliest elastic FE models was applied by Chen and Govindaraj in the 1990s [7], in which a woven fabric was modelled as a continuous, orthotropic medium. Although fabrics are discontinuous at lower length scales, the continuous approach has proven to be successful in many forming simulations [8–12]. Reinforcements can be included in FE models by adding bar or truss elements to standard continuum elements. This semi-discrete approach has been used by several researchers [13, 14]. Modelling each individual constituent of the fabric as a separate object is (yet) computationally too expensive for forming simulations of fibre reinforced materials. This discrete approach is limited to analyses on a mesoscopic level, where it can provide useful information on the mechanical properties of the fabric and can replace elaborate or complicated experiments [15, 16].

An important problem that has to be solved in FE simulations of fibre reinforced materials is intra-ply shear locking. Intra-ply shear locking is

the incapability of the element displacement field to represent the correct deformation mechanism of the fibre reinforced material. It is a numerical problem that is not related to the physical jamming of the reinforcement. It leads to overestimation of fibre stresses, forces and stiffnesses and often leads to spurious wrinkles in 3D simulations. The first article that addresses the intra-ply shear locking problem and illustrates the shortcomings of the current standard element formulation was presented by Yu et al. in 2005 [17]. An extended version was published in 2006 [18].

Intra-ply shear locking can occur in all FE simulation that use the continuum or the semi-discrete approach. Both approaches use continuum elements that span multiple yarns and are restricted to deformations that are allowed by the elements' displacement fields. These might inhibit the shear deformation with intra-ply shear locking as a result. Discrete approaches are free of intra-ply shear locking due to the detailed scale of modelling. The macroscopic deformation is not restricted by the elements' displacement field in this case.

The origin and consequences of the locking problem are discussed in the next subsection. Possible solutions to the locking problem are presented in section 3.2 and in section 3.3 the performance of the different remedies is investigated in a two-dimensional case. The resulting non-locking elements were tested in a realistic three-dimensional drape simulation of a biaxial fabric in section 3.4. The paper ends with the conclusions drawn from this research in section 3.5.

### 3.1.1 Intra-ply shear locking

The locking phenomenon can be illustrated by simulating the bias extension experiment. The bias extension experiment is frequently used to examine the shear response of biaxial reinforced materials. The left hand side of figure 3.1 shows the undeformed and the deformed shape of the material. The two fibre directions are initially perpendicular to each other at $\pm 45°$. The specimen is gripped on the short edges and gradually extended. The stiffness of the fibres is dominant and the material deforms as a trellis frame, with each fibre crossing acting as a possible hinge point. Three deformation regions develop: an undeformed region (I), a central region with pure shear (II) and a region with intermediate shear (III).

Next, two finite element models are built. The first one is built using mesh A. The element borders are aligned with the fibre directions and coincide with the lines along which the material develops 'hinge' lines. Figure 3.2 shows the available options for aligning a fibre direction $\mathbf{a}$ with the element edges for

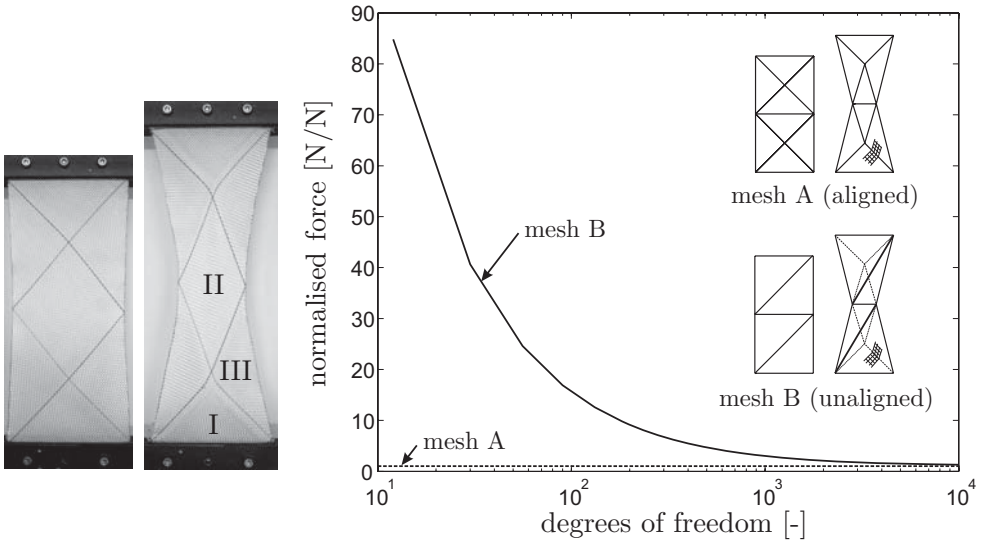


*Figure 3.1: The bias extension experiment with the three different deformation regions. The simulation with mesh B shows intra-ply shear locking.*

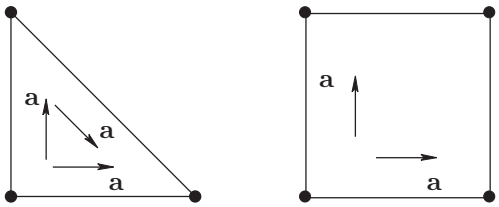


*Figure 3.2: Alignment of the fibre direction* $\boldsymbol{a}$ *in a triangular and quadrilateral element. Three and two alignment options are available, respectively.*

both a triangular element and a quadrilateral element. The aligned mesh in figure 3.1, mesh A, can represent the trellis deformation correctly and locking is absent. The second FE model is built using mesh B. This mesh shows severe locking, since the elements cannot represent the discontinuous shear field. Fibres are stretched during the simulation, resulting in unrealistically high forces. The graph in figure 3.1 shows the resulting tensile force of the bias extension simulation with both mesh types. Dimensions and material properties can be found in Table 3.1. The specimen is elongated to 115% of the original length. The force is normalised with respect to the tensile force resulting from the simulation with an aligned mesh using eight linear triangular elements (mesh A). The figure shows that locking is reduced if the number of elements increases. This is the case in most types of locking. The

| | | | | | |
|---|---|---|---|---|---|
| width | [mm] | 50 | bulk stiffness | [MPa] | 2 |
| height | [mm] | 100 | fibre stiffness | [MPa] | 4000 |
| thickness | [mm] | 1 | bulk volume fraction | [-] | 0.50 |
| mesh | [-] | 2 x 4 | fibre volume fraction (2x) | [-] | 0.25 |

*Table 3.1: Parameters of the bias extension simulation.*

excessive amount of elements necessary to eliminate locking for this problem would lead to unacceptable simulation times in a regular forming simulation. Other solutions have to be found and three options are presented in the next section.

## 3.2 Remedies against intra-ply shear locking

Forming simulations of fibre reinforced materials are often performed on relatively thin blanks where the blank is modelled using membrane or shell elements. The blank can have any arbitrary shape. Triangular meshes are preferred, since mesh generators for triangular meshes tend to be more robust than those for quadrilaterals when meshing arbitrarily shaped blanks [19]. From a programmer's point of view, the simplex elements are popular elements. These elements have linear displacement fields and constant gradients, making them easy to implement and fast in terms of calculation time. The simplex triangle is therefore an obvious choice, but, as shown in the previous paragraph, it exhibits severe locking if the mesh is unaligned.

Three possible ways to avoid locking are discussed in this paper:

1. Aligned meshes
2. Selective reduced integration
3. Multi-field elements

Some of these options make it necessary to use higher order elements or quadrilaterals. The X-FEM method has not been considered here, although it initially seems a suitable method. X-FEM elements have been designed to represent discontinuous fields within one element. This allows for efficient simulations of growing cracks or moving material boundaries without the need for continuous re-meshing. According to Yu et al. [18], the simplex triangular element needs three and the simplex quadrilateral needs five additional intra-ply shear modes to represent the correct shear behaviour for a biaxial fabric. According to our opinion, each element needs an infinite number of additional

shear modes. Yu et al. assumed that the discontinuity crosses at least one node of the element. However, in an unaligned mesh the discontinuity can cross the element at any arbitrary place. The origin of the discontinuity is also unknown beforehand. This makes the implementation of the X-FEM method problematic and computationally too intensive.

### 3.2.1 Aligned meshes

Aligning the mesh with the fibre directions is probably one of the best remedies against intra-ply shear locking. Special attention is needed at curved edges of the blanks during meshing, where element edges cannot simply follow the curved boundary. This was already shown in the drape simulation in the article of Yu et al. [18]. This limits the use of automatic mesh generation. Alignment becomes impossible if the element contains more than two fibre directions. This can occur in multi-layer elements, where several layers are efficiently modelled within one element through the thickness [20, 21]. Alignment also limits the use of Arbitrary Lagrangian Eulerian (ALE) methods, in which the alignment of the fibres and the mesh will disappear during the simulation.

### 3.2.2 Selective reduced integration (SRI)

Reduced integration or under-integration of elements is a well known method to eliminate several types of locking [19, 22, 23]. Yu et al. [18] illustrated the use of reduced integration to eliminate intra-ply shear locking for woven fabrics. An unaligned fully integrated element will lock in a region where the shear field is discontinuous. The discontinuity results in fibre strains in at least one of the integration points. Reduced integration relieves this condition. Fibres can stretch freely in the integration points that are left out, eliminating the locking. The corresponding element deformation is a zero energy mode. Yu et al. did not consider reduced integration to be a useful option, due to the unwanted hourglassing effect that can occur. Hourglassing is a repetitive pattern of zero energy modes and can be suppressed by hourglass control. This, however, gives rise to locking again as Yu et al. show in one of their simulations. In our opinion, Selective Reduced Integration (SRI) should be used instead of complete reduced integration. The term selective denotes that reduced integration should only be applied to the fibre constituent of the material model. This avoids the hourglassing problem.

The locking problem cannot be solved for the linear triangle by reduced integration, since it is already fully integrated with only one integration point. Quadratic elements are required for reduced integration of triangular elements and that is a drawback, firstly because of the implementation and

simulation time arguments mentioned before and secondly because of the known problems in simulations including contact and quadratic elements. The midside nodes of quadratic elements especially tend to oscillate during the simulation, slowing down the simulation progress and causing unrealistic results at the interface [19, 24]. Finally, the improved accuracy of higher order elements drops in nonlinear simulations with large deformations [19]. The order of the displacement field of an element can be increased by adding degrees of freedom to existing nodes instead of adding new nodes. An example is the Allmann88 triangle with vertex rotations [25–27]. This Allman88 triangle is derived from the quadratic triangle, where the midside nodes are replaced by vertex rotations and additional constraints. This element is included in this research, because it is expected to be more robust in simulations using contact.

### 3.2.3 Multi-field element (MF)

Multi-field elements are also known as mixed elements. These elements contain degrees of freedom of different types, e.g. displacement and temperature. We developed a multi-field element, where fibre strain is chosen as an additional degree of freedom. The new element is an assumed strain element, the fibre strain is interpolated independent of the displacement field. Locking of the elements is avoided by choosing the correct order of both the interpolation fields. A non-locking combination is e.g. the quadratic displacement - constant fibre strain triangle. Normally, a quadratic element has a linear fibre strain field. By assuming this strain to be constant, the number of fibre strain constraints is reduced and locking is avoided.

A fibre $f$ with direction $\mathbf{a}$ is located in a continuum body at position $\mathbf{x}$. The element strain in the direction of the fibre must equal the assumed strain $\boldsymbol{\varepsilon}_f$ of the fibre. This results in a total of three equations for the body under consideration, an equilibrium equation, a boundary traction condition and a fibre strain constraint:

$$\boldsymbol{\sigma} \cdot \overleftarrow{\nabla} + \mathbf{f} = 0 \qquad (\sigma_{ij,j} + f_i = 0) \qquad in\ V \tag{3.1}$$

$$\boldsymbol{\sigma} \cdot \mathbf{n} = \mathbf{t} \qquad (\sigma_{ij} n_j = t_i) \qquad on\ \Gamma \tag{3.2}$$

$$\mathbf{a} \cdot \mathbf{u}\overleftarrow{\nabla} \cdot \mathbf{a} - \varepsilon_f = 0 \qquad (a_i u_{i,j} a_j - \varepsilon_f = 0) \qquad in\ V, \tag{3.3}$$

with $V$ the volume of the body and $\Gamma$ the boundary. The vector $\mathbf{f}$ denotes the body forces, $\mathbf{t}$, the boundary tractions and $\mathbf{n}$, the outward normal on the boundary. The total stress $\boldsymbol{\sigma}$ consists of an element stress $\boldsymbol{\sigma}^{el}$ that is derived through the normal finite element equations and a scalar fibre stress $\sigma_f$ that

results from the additional field:

$$\boldsymbol{\sigma} = \boldsymbol{\sigma}^{el} + \sigma_f \mathbf{aa} \qquad (\sigma_{ij} = \sigma_{ij}^{el} + \sigma_f a_i a_j), \tag{3.4}$$

The fibre stress and strain are related through $\sigma_f = E_f \varepsilon_f$, with $E_f$ the Young's modulus of the fibre. Equations (3.1) and (3.2) are weighted with a set of weight functions $\mathbf{w}$ and equation (3.3) with a weight function $q$. Applying integration by parts and the divergence theorem of Gauss results in the following weak form:

$$\int_V \mathbf{w}\overleftarrow{\nabla} : \boldsymbol{\sigma}^{el}\, dV + \int_V \mathbf{w}\overleftarrow{\nabla} : \sigma_f \mathbf{aa}\, dV + \int_V q(\mathbf{a}\cdot\mathbf{u}\overleftarrow{\nabla}\cdot\mathbf{a})\, dV - \int_V q\varepsilon_f\, dV = \int_\Gamma \mathbf{w}\cdot\mathbf{t}\, d\Gamma + \int_V \mathbf{w}\cdot\mathbf{f}\, dV. \tag{3.5}$$

Following Galerkin's method, equation (3.5) results in the following system of equations:

$$\begin{bmatrix} \mathbf{K} & \mathbf{G} \\ \mathbf{H} & \mathbf{L} \end{bmatrix} \cdot \begin{Bmatrix} \mathbf{u}^k \\ \varepsilon_f^k \end{Bmatrix} = \begin{Bmatrix} \mathbf{F} \\ \mathbf{0} \end{Bmatrix}, \tag{3.6}$$

with $\mathbf{u}^k$ and $\varepsilon_f^k$, the nodal degrees of freedom and $k$, the nodal counter. The vector and matrix components are given by:

$$K^{\alpha\beta} = \int_V \tfrac{1}{2}(\mathbf{N}^\alpha\overleftarrow{\nabla} + \overrightarrow{\nabla}\mathbf{N}^\alpha) :^4 \mathbf{E} : \tfrac{1}{2}(\mathbf{N}^\beta\overleftarrow{\nabla} + \overrightarrow{\nabla}\mathbf{N}^\beta)\, dV \tag{3.7}$$

$$G^{\alpha\gamma} = \int_V \tfrac{E_f}{2}(\mathbf{N}^\alpha\overleftarrow{\nabla} + \overrightarrow{\nabla}\mathbf{N}^\alpha) : \mathbf{aa}\mathbf{M}^\gamma\, dV \tag{3.8}$$

$$H^{\eta\beta} = \int_V \tfrac{1}{2}(\mathbf{N}^\beta\overleftarrow{\nabla} + \overrightarrow{\nabla}\mathbf{N}^\beta) : \mathbf{aa}\mathbf{M}^\eta\, dV \tag{3.9}$$

$$L^{\eta\gamma} = -\int_V \mathbf{M}^\eta\mathbf{M}^\gamma\, dV \tag{3.10}$$

$$F^\alpha = \int_\Gamma \mathbf{N}^\alpha\cdot\mathbf{t}\, d\Gamma + \int_V \mathbf{N}^\alpha\cdot\mathbf{f}\, dV, \tag{3.11}$$

where $\mathbf{N}$ denotes the corresponding set of interpolation functions for the displacement field and $\mathbf{M}$ the interpolation function for the strain field. The system of equations (3.6) is non-symmetric. It will become symmetric if the fibre stress is chosen as the additional degree of freedom, but large deformation simulations revealed a more robust behaviour of the multi-field element with the strain degree of freedom. Strain values are closer to the displacement values, which result in a decreased loss of significant digits and less ill-conditioned numerical systems. In this case we have chosen robustness over symmetry of the set of equations.

Arbitrary combinations of interpolation for the separate fields may lead to poor numerical performance or even non-convergence [23, p. 200]. Interpolation fields of equal order will always result in a non-convergent element, unless additional effort is made to stabilise the field(s) as done by Hughes [28]. Two non-locking multi-field elements are included in this research: the quadratic displacement - constant fibre strain triangle and the linear displacement - constant fibre strain quadrilateral. Both these elements are convergent without additional stabilisation.

The general theorem of Malkus and Hughes [29] established the equivalence between many selective reduced integration of elements and multi-field elements. Although not investigated thoroughly, the SRI and the multi-field elements presented here are likely to be equivalent in small deformations. Given a small deformation, both elements respond with the same Cauchy stress and nodal forces. However, the convergence rate of the multi-field element appeared to be far better than the convergence rate of the SRI-elements in large deformation simulations. For this reason, both element types are included in this research.

## 3.3 Implementation and results

Nine different elements were selected based on the remedies against intra-ply shear locking that were discussed in the previous section, as shown in figure 3.3.

1. Simplex (linear) triangle (LTR)
2. Quadratic triangle (QTR)
3. Quadratic triangle with selective reduced integration (QTR_SRI)
4. Allman88 triangle (DRIL)
5. Allman88 triangle with selective reduced integration (DRIL_SRI)
6. Multi-field quadratic triangle with a constant strain field (QTR_CMF)
7. Simplex (linear) quadrilateral (QUAD)
8. Simplex (linear) quadrilateral with selective reduced integration (QUAD_SRI)
9. Multi-field simplex quadrilateral with a constant strain field (QUAD_CMF)

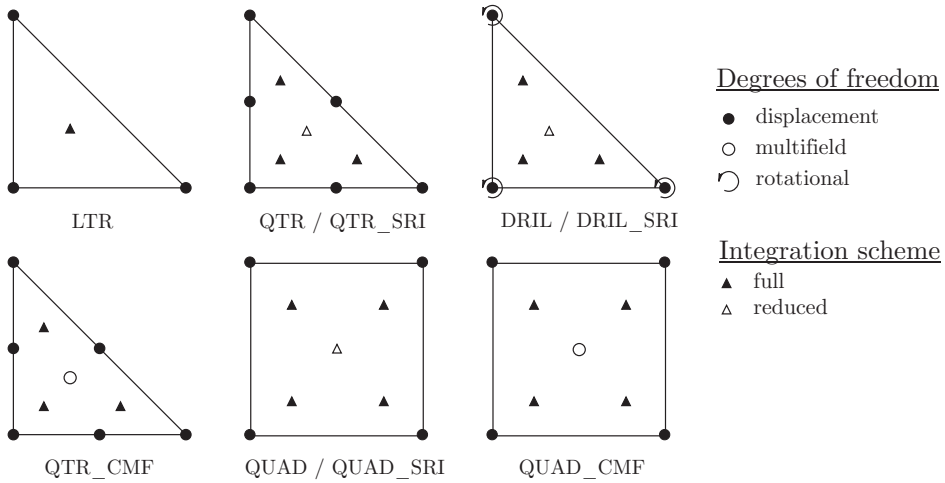


*Figure 3.3: Nine different elements that were tested on their performance in a bias extension simulation.*

The elements were tested in a bias extension simulation as shown in figure 3.1 in a relatively coarse mesh. The number of elements ranged between 8 and 16, depending on the element type and mesh type. The material model consists of several material fractions. The deformation is equal for each fraction and each fraction contributes to the total stress proportional to its volume fraction $\nu$:

$$\boldsymbol{\sigma} = \Sigma_i \nu_i \boldsymbol{\sigma}_i \ , \tag{3.12}$$

where $i$ denotes the fraction number and the sum of the volume fractions equals unity. This allows for implementation of several material models into one element. The biaxial material is represented by an elastic isotropic bulk fraction and two fibre fractions. The geometry and the material parameters of the bias extension simulation can be found in Table 3.1. The prescribed elongation was 1 mm. Aligned and unaligned meshes of triangles were used, whereas the mesh of the quadrilaterals was necessarily unaligned. Figure 3.4 shows the resulting tensile forces of the simulations. The exact solution is not trivial for this simulation where fibres are not infinitely stiff. The borders between the different shear regions will develop a slight curvature instead of remaining straight as would be the case with infinitely stiff fibres. The simulation with the aligned mesh using simplex triangles is expected to be close to the exact solution and the tensile forces are normalised with respect to the result of this simulation.

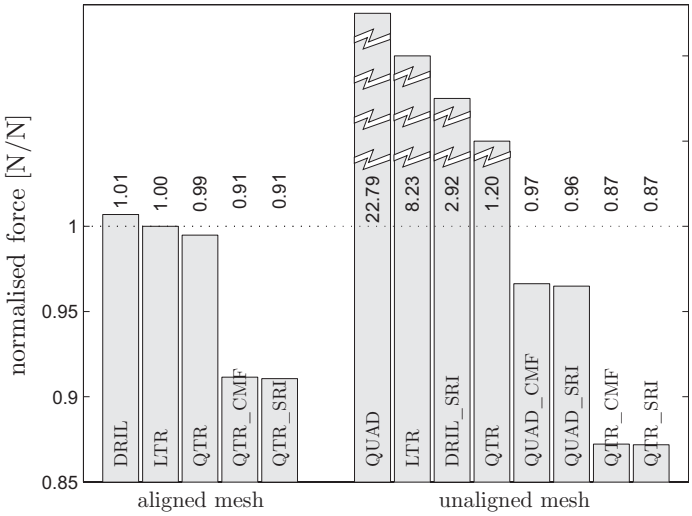


*Figure 3.4: Tensile forces from simulation of the bias extension test. The forces are normalised with respect to the simulations with aligned simplex triangles.*

The fully integrated elements show accurate results in aligned meshes and show locking in unaligned meshes, as expected. The quadratic triangle (QTR) has an overshoot of only 20% in the unaligned case, due to the small displacement in this particular case. Locking becomes more severe for this element if the elongation is increased. The results from the constant multi-field (CMF) elements and the elements with selective reduced integration (SRI) are almost identical. SRI reduces the number of evaluated fibre strains in an element to one, equal to the number of fibre strains in the CMF element. Both SRI and MF elements effectively eliminate locking. Elements become significantly more compliant, even more than the aligned, fully integrated elements. This effect is known from other types of locking: reduced integration over-eliminates the locking effect. The MF and SRI quadrilaterals give the most accurate results in unaligned meshes. The deviation in the predicted tensile force is around 4% for this specific configuration, using a relatively coarse mesh. The error decreases when the number of elements increases. A dens mesh of 25 by 50 elements reduced the error to 0.5% for the quadrilaterals and to 5% for the quadratic triangles using MF or SRI. The Allman88 element (DRIL), with drilling degrees of freedom and with SRI, still locks in an unaligned mesh. The added degrees of freedom (and zero energy modes) are apparently insufficient to eliminate locking. It would be convenient to assess the element's tendency to lock beforehand. A procedure to do this is the constraint counting method.

### 3.3.1 Constraint counting

Constraint counting is a heuristic method and has proven to be effective in predicting the tendency of elements to lock [23, p. 209]. It is not based on a mathematical analysis and an optimal constraint count does not necessarily imply that the complete element performance is optimal. Figure 3.5 shows a standard mesh that is suppressed at two sides. If the number of elements approaches infinity, the constraint ratio is given by:

$$r = \frac{n_u}{n_i} \tag{3.13}$$

where $n_u$ is the number of displacement degrees of freedom and $n_i$ is the number of inextensibility constraints or the number of stiff fibre directions within the element. Figure 3.5 shows the constraint ratios for several elements used to simulate the deformation of a biaxial fabric. For example, in figure 3.5a the constraint ratio of the linear triangle is $\frac{1}{2}$. For each node with two degrees of freedom that is added to this mesh, two integration points are added, both of which contain two inextensibility constraints. Constraint ratios for elements with reduced integration and those for the corresponding multi-field elements are equal. One integration point imposes the same number of constraints as a constant multi-field.

The constraint ratio for an unaligned mesh has to be larger than or equal to one, to avoid locking. This can be illustrated by comparing figure 3.4 and 3.5. The fully integrated quadrilateral has the smallest constraint ratio and shows severe locking. The quadratic triangle with reduced integration or a constant multi-field has the largest constraint ratio and results in the lowest bias extension force. The SRI and MF quadrilateral have an optimal constraint ratio and are the most accurate in the two-dimensional bias extension simulation. The Allman88 triangle has a constraint ratio below one and will always lock, even if rotations at the clamped edges are allowed. The constraint ratio appears to be consistent with the behaviour found in the bias extension simulations.

However, constraint counting by itself is insufficient to predict the locking behaviour of elements. Element with additional displacements tangent to element sides and constraint ratios above one still showed severe locking. Additional bubble modes or incompatible modes appeared to be ineffective as well. The displacement field of the element (or several elements) has to be able to conform to displacements as shown in figure 3.1. Mesh edges must be able to deform in a direction normal to that edge for this type of locking. Otherwise the element will still lock.

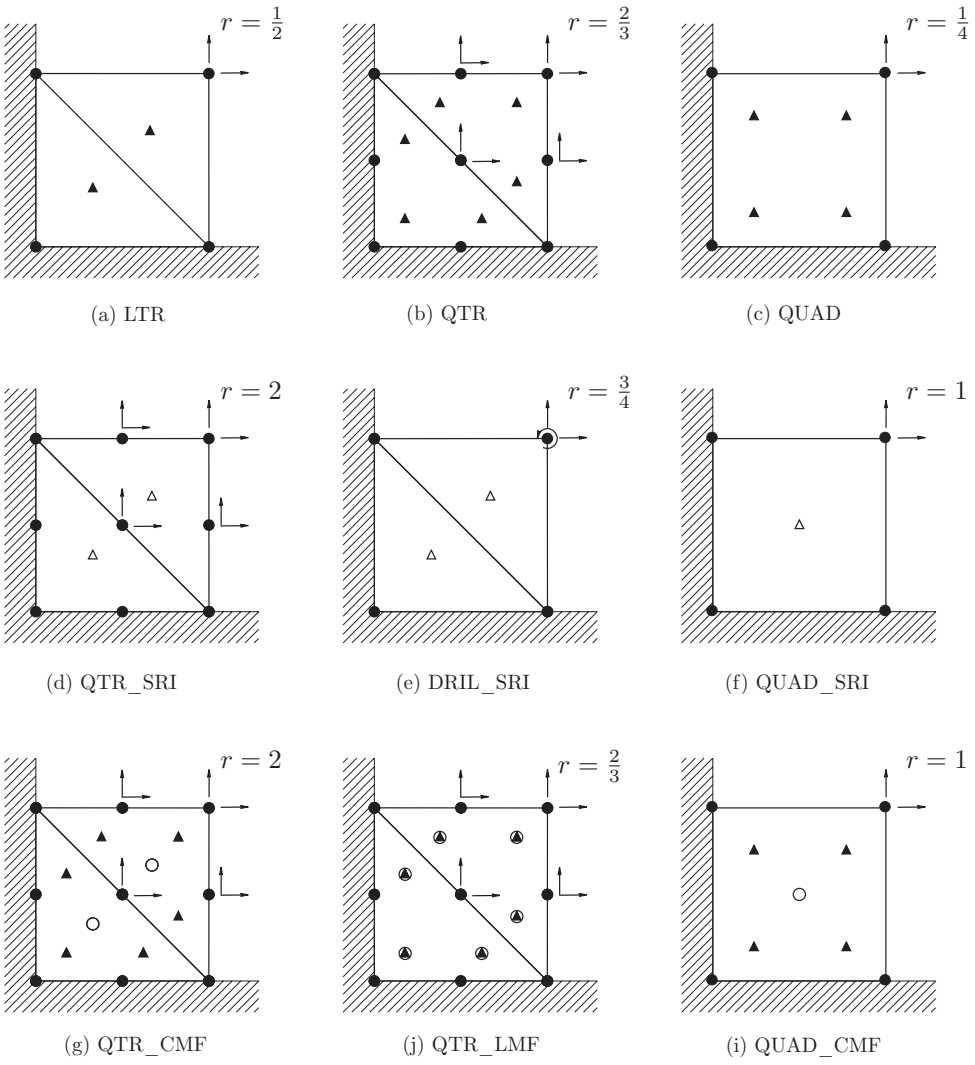


(a) LTR (b) QTR (c) QUAD

(d) QTR_SRI (e) DRIL_SRI (f) QUAD_SRI

(g) QTR_CMF (j) QTR_LMF (i) QUAD_CMF

*Figure 3.5: Constraint ratio.*

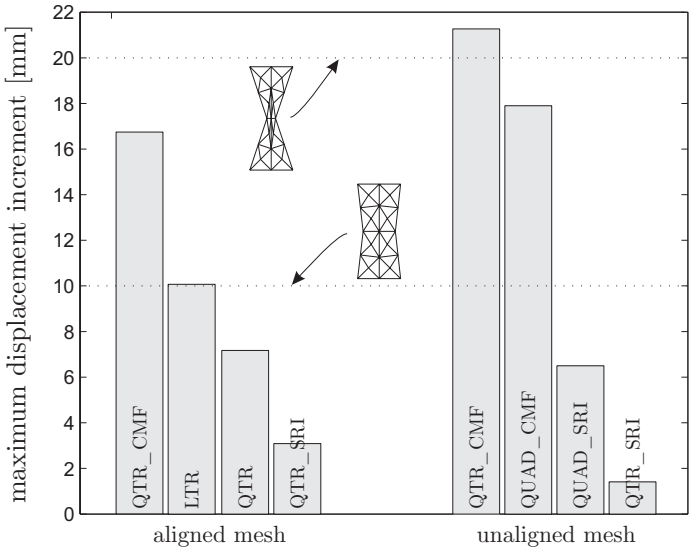


*Figure 3.6: Maximum incremental displacement within one step.*

### 3.3.2 Element performance

Forming simulations of fibre reinforced composites must perform well in large deformations of highly anisotropic material. The locking-free elements from figure 3.4 were tested on their performance in large deformations. The fibre stiffness was increased by a factor $10^3$ to create an extremely anisotropic material and to test the limits of the elements. The tangent matrix was calculated numerically for all element types. The unbalance norm $\epsilon_r$ and the displacement norm $\epsilon_u$ are given by:

$$\epsilon_r = \frac{\|R - F\|}{\|R\|}, \qquad \epsilon_u = \frac{\|\triangle u\|}{\|u\|}, \tag{3.14}$$

where $R$ are the reaction forces, $F$, the applied nodal loads, $\triangle u$, the displacement found during the iteration and $u$, the total displacement. A strict maximum value of $10^{-8}$ was used for both norms as a convergence criterion and the maximum number of iterations was set to eight. The maximum allowable incremental displacement of one step was then determined iteratively. Figure 3.6 shows the results of this analysis. The element performance deteriorates when reduced integration is used and improves for multi-field elements. The maximum step size for the aligned quadratic triangles is around 7% of the total specimen's length. This value increases by almost 2.5 times for the multi-field element and decreases by almost 2.5 times for the element that uses SRI. For unaligned meshes the difference is even larger. The quadrilaterals perform

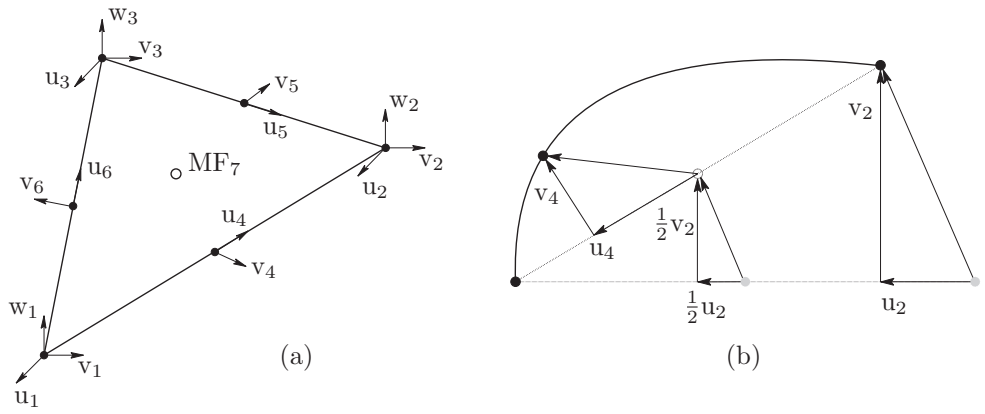


*Figure 3.7: Triangular element with a quadratic in-plane and a linear out-of-plane displacement field.*

quite well and the difference between SRI and the multi-field element is not as large as it is for the quadratic triangle.

### 3.3.3 Advanced triangular membrane element

Aligning the mesh, selective reduced integration and multi-field elements all solve the locking problem in 2D simulations with biaxial fabrics. Only SRI and MF elements are locking-free in unaligned meshes and can be used in combination with automatic mesh generation and multi-layer elements. The multi-field quadrilateral element is the best choice based on the 2D simulation results. It is accurate and performs well in large deformations. The quadratic displacement - constant fibre strain multi-field element performs even better in large deformations, but it is less accurate.

Triangular elements are preferred to quadrilaterals in automatic mesh generation and 3D simulations with large deformations. Locking-free triangular elements are all higher order elements and to solve their known problems in simulations including contact, the element is given separate displacement fields for the in-plane and out-of-plane displacement. The elements contain only a higher order in-plane displacement field and the out-of-plane displacement remains linear to avoid oscillations of the midside nodes in this direction. Figure 3.7a shows the QTR_CMF element. Midside node displacements are defined with respect to the average nodal displacement of the corresponding corner nodes as shown in figure 3.7b. The midside node can have an additional displacement tangential to the straight line between

the corner nodes and a displacement in the direction of the outward normal.

This QTR element still behaves too compliant. Suppressing the $u$-displacement of the midside nodes lowers the constraint ratio and improves the accuracy. Only an in-plane displacement normal to the element edge is allowed. The resulting semi-quadratic (SQTR) element has a constraint ratio of $\frac{5}{4}$. A bias extension simulation with this element results in a normalised tensile force of 0.94 N/N, which is, as expected, based on the constraint ratios. The SQTR element developed here will be included in the 3D drape simulations in the next section to assess the performance in realistic 3D drape simulations.

## 3.4 Application: a 3D drape simulation

A drape process has been simulated to test the performance of the locking-free elements in three-dimensional composite forming processes. A biaxial reinforced fabric is drawn into a hemispherically shaped mould. The setup is shown in figure 3.8. The simulation parameters can be found in Table 3.2. The ratio between fibre stiffness and bulk stiffness is $10^4$, resulting in a highly anisotropic material that shears easily and has a negligible elongation in the fibre direction. Mass scaling has been applied to speed up the simulations [30]. The amount of mass scaling has a negligible effect on the simulation results, with observed deviations up to a maximum of 2% in punch force and final fibre stresses. Contact between the fabric and the tools is modelled using a penalty formulation. The fabric can slide along the tools without friction. The fabric will develop so called 'ears' during draping and will have regions where the shear deformation is high. The simulations were run using the following membrane elements and meshes:

1. LTR, aligned mesh
2. QUAD, aligned mesh
3. SQTR_SRI, unaligned mesh
4. SQTR_CMF, unaligned mesh
5. QUAD_SRI, unaligned mesh
6. QUAD_CMF, unaligned mesh

The list contains triangular and quadrilateral elements and all three remedies against intra-ply shear locking are included. Figure 3.9 shows the top view

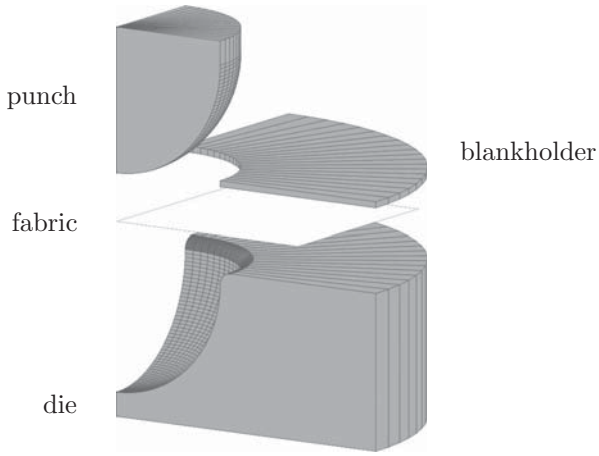


*Figure 3.8: Drape setup.*

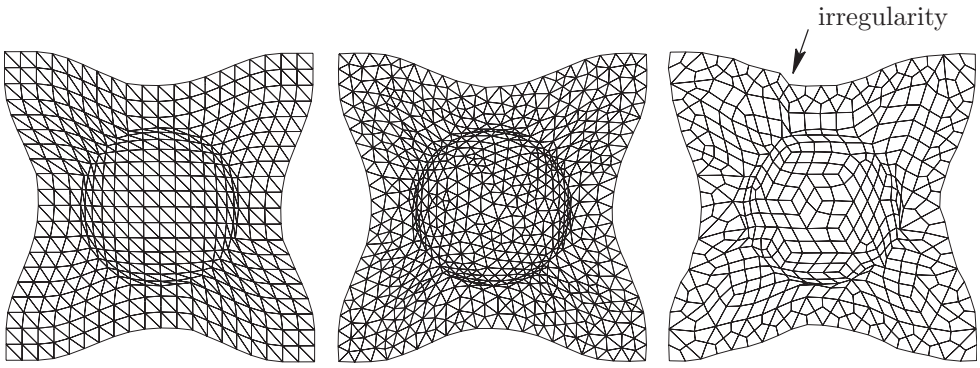


*Figure 3.9: Top view of the fabric at the end of the drape simulation.*

| | | | | | |
|---|---|---|---|---|---|
| fabric dim. | [mm] | 400 x 400 | bulk stiffness | [MPa] | 0.2 |
| fabric thickn. | [mm] | 1 | bulk vol. frac. | [-] | 0.50 |
| die radius | [mm] | 100 | fibre stiffness | [MPa] | 4000 |
| die shoulder | [mm] | 20 | fibre vol. frac. | [-] | 0.25 |
| mesh | [-] | 20 x 20 | fabric density | [kg/m$^3$] | 2000 |
| punch velocity | [mm/s] | 10 | mass scaling | [-] | $10^4$ |

*Table 3.2: Parameters of the drape simulation.*

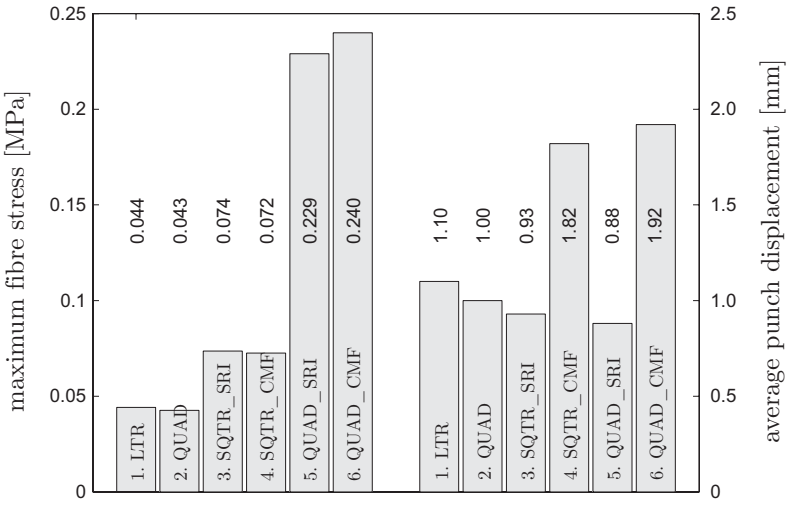


*Figure 3.10: Maximum fibre stress and average punch displacement during the drape simulation.*

of the final fabric geometry of several simulations. Figure 3.9a shows the results when using an aligned triangular mesh. Figure 3.9b and 3.9c show the results of an unaligned mesh using triangular and quadrilateral elements, respectively. The deformed shape of the simulation with an unaligned mesh using quadrilaterals shows regions where mesh edges exhibit irregularities. It also shows some elements, which are poorly shaped due to large shear deformations. The deformed shape of the fabric meshed with SQTR elements is nearly identical to the simulation with an aligned mesh and does not show any poorly shaped elements. On average, triangular elements seem less susceptible to become poorly shaped than quadrilaterals.

The maximum fibre stress that occurred during the simulation for the different element types and meshes is shown on the left hand side of figure 3.10. The quadrilateral element over-predicts the maximum fibre stress by more than five times, when the simulation with the aligned linear triangles is regarded as the reference. This simulation results in the highest punch force in figure 3.11 as well. The mesh irregularity, the high fibre stress and the high punch force indicate that the quadrilateral elements still exhibit locking in unaligned meshes. The semi-quadratic triangular elements predict a maximum fibre stress that is much closer to the aligned mesh results. Punch forces are also significantly lower for this element, even lower than the punch forces predicted by the aligned elements. The fibre stress and punch force are very

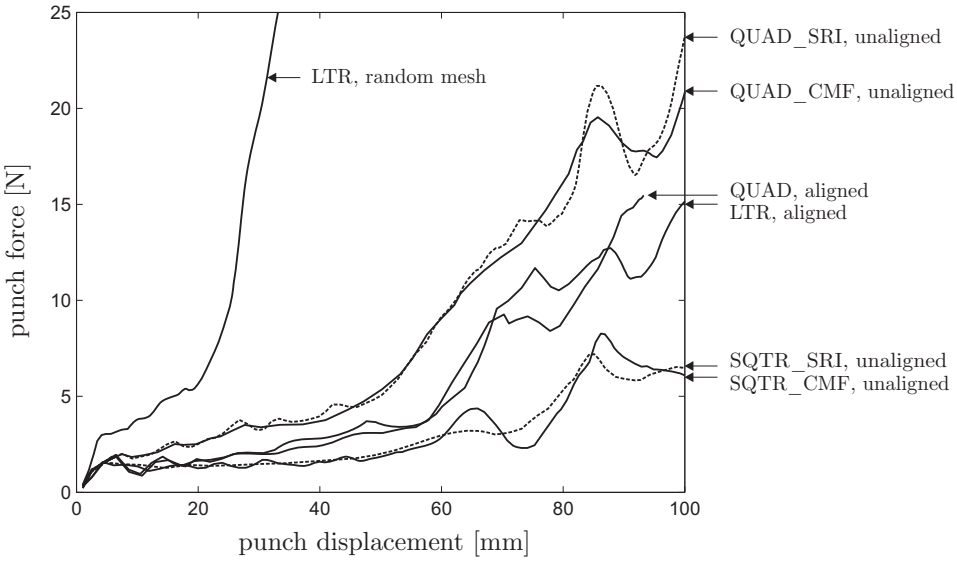


*Figure 3.11: Punch force.*

sensitive to mesh configuration and fibre stiffness. Reducing the anisotropy by lowering the fibre stiffness and refining the mesh will bring the results closer together. However, the objective is to have a non-locking element that gives accurate results for coarse meshes and highly anisotropic materials. The punch force of the simulation, which uses linear triangles in an unaligned mesh, is included in figure 3.11 to illustrate the unrealistic results for locking elements. Punch forces and fibre stresses are easily over-predicted by a factor of 1000 in this case.

The total punch displacement is imposed incrementally. A robust element allows for large increments and short simulation times. The right hand side of figure 3.10 shows the average punch displacement for each element type. Reduced integration reduces the allowable increment size, while the multi-field elements allow increments that are nearly twice as large. The difference is not as extreme as in the 2D case discussed in section 3.3.2. The performance is affected by other factors as well, in particular by the contact algorithm. Multi-field elements increase the simulation time of a single increment by 10 to 15% compared to SRI elements. This results in a nett reduction of the total simulation time of nearly 40% with the observed increase in increment size.

## 3.5 Conclusions

Three remedies against intra-ply shear locking were investigated in this paper: aligning the mesh, applying selective reduced integration (SRI) and using multi-field elements. All fully integrated standard elements have to be aligned with the fibre directions in the material to avoid locking. SRI and multi-field elements are free of locking for any mesh configuration. SRI indicates that only the fibre constituents of the material model are under-integrated. The new multi-field elements combine the standard displacement degrees of freedom with an additional field that interpolates the fibre strain. Choosing strain instead of stress results in a more robust element in large deformation simulations.

Aligning the mesh is the best option with respect to accuracy, but limits the use of automatic mesh generation and makes implementation of multi-layer elements impossible. Elements based on SRI and multi-field elements underestimate the stiffness, typically from 5% down to 15% in this particular study. The constraint counting method proved to be a useful method to predict beforehand, the element's accuracy and tendency to lock. The performance of the different elements in large deformation simulations was tested as well. The multi-field element allows for the largest step sizes, followed by the aligned elements and then by the SRI elements.

A triangular multi-field membrane element was developed with a semi-quadratic in-plane and a linear out-of-plane displacement field. This combination improves the accuracy of the element and avoids contact problems in 3D simulations. It is the best element to use in large deformations of fibre reinforced materials in unaligned meshes, based on the results from this analysis, where the element was tested in a 2D simulation and a realistic 3D drape simulation.

## Bibliography

[1] C. Mack and H. Taylor. 'The fitting of woven cloth to surfaces'. *J Text I*, 47:477–487, 1956.

[2] P. Potluri, S. Sharma and R. Ramgulam. 'Comprehensive drape modelling for moulding 3D textile preforms'. *Compos Part A-Appl S*, 32:1415–1424, 2001.

[3] M. Aono, D. E. Breen and M. J. Wozny. 'Modeling methods for the design of 3D broadcloth composite parts'. *Comput Aided Design*, 33:989–1007, 2001.

[4] S. G. Hancock and K. D. Potter. 'The use of kinematic drape modelling to inform the hand lay-up of complex composite components using woven reinforcements'. *Compos Part A-Appl S*, 37:413–422, 2006.

[5] S. G. Hancock and K. D. Potter. 'Virtual Fabric Placement - A new strategy for simultaneous preform design, process visualisation and production of manufacturing instructions for woven composite components'. In *Proc 9th Int ESAFORM Conf*, pages 727–730. Publishing House Akapit, Krakow, Poland, 2006, 2006. ISBN 83-89541-66-1.

[6] A. C. Long. 'An iterative draping simulation based on fabric mechanisms'. In *Proc 4th Int ESAFORM Conf*, pages 99–102. 2001.

[7] B. Chen and M. Govindaraj. 'A physically based model of fabric drape using flexible shell theory'. *Text Res J*, 65:324–330, 1995.

[8] A. Spencer. 'Theory of fabric-reinforced viscous fluids'. *Compos Part A-Appl S*, 31:1311–1321, 2000.

[9] W.-R. Yu, P. Harrison and A. Long. 'Finite element forming simulation for non-crimp fabrics using a non-orthogonal constitutive equation'. *Compos Part A-Appl S*, 36:1079–1093, 2005.

[10] X. Peng and J. Cao. 'A continuum mechanics-based non-orthogonal constitutive model for woven composite fabrics'. *Compos Part A-Appl S*, 36:859–874, 2005.

[11] P. Xue, X. Peng and J. Cao. 'Non-orthogonal constitutive model for characterizing woven composites'. *Compos Part A-Appl S*, 34:183–193, 2003.

[12] R. H. W. ten Thije, R. Akkerman and J. Huétink. 'Large deformation simulation of anisotropic material using an updated Lagrangian finite element method'. *Comput Method Appl M*, 196:3141–3150, 2007.

[13] S. Reese. 'Meso-macro modelling of fibre-reinforced rubber-like composites exhibiting large elastoplastic deformation'. *Int J Solids Struct*, 40:951–980, 2003.

[14] S. B. Sharma and M. P. F. Sutcliffe. 'A simplified finite element model for draping of woven material'. *Compos Part A-Appl S*, 35:637–643, 2004.

[15] D. Durville. 'Numerical simulation of entangled materials mechanical properties'. *J Mater Sci*, 40:5941–5948, 2005.

[16] S. V. Lomov, D. S. Ivanov, I. Verpoest, M. Zako, T. Kurashiki, H. Nakai and S. Hirosawa. 'Meso-FE modelling of textile composites: Road map, data flow and algorithms'. *Compos Sci Technol*, 67:1870–1891, 2007.

[17] X. Yu, L. Ye and Y. Mai. 'Spurious Wrinkles in Forming Simulations of Woven Fabric'. *Int J Form Process*, 8/SI:141–155, 2005.

[18] X. Yu, B. Cartwright, D. McGuckin, L. Ye and Y.-W. Mai. 'Intra-ply shear locking in finite element analyses of woven fabric forming processes'. *Compos Part A-Appl S*, 37:790–803, 2006.

[19] T. Belytschko, W. K. Liu and B. Moran. *Nonlinear Finite Elements for Continua and Structures*. John Wiley & Sons Ltd, West Sussex, England, 2000. ISBN 0-471-98774-3.

[20] R. H. W. ten Thije, R. Loendersloot and R. Akkerman. 'Drape simulation of non-crimp fabrics'. In *Proc 8th Int ESAFORM Conf*, pages 991–994. Publishing house of Romanian Academy, Bucharest, Romania, 2005. ISBN 973-27-1174-6.

[21] R. Akkerman, E. A. D. Lamers and S. Wijskamp. 'An integral process model for high precision composite forming'. *Eur J Comput Mech*, 4:359–378, 2006.

[22] O. C. Zienkiewicz and R. L. Taylor. *The Finite Element Method for Solid and Structural Mechanics, Sixth Edition*. Butterworth-Heinemann, 2002. ISBN 978-0750663212.

[23] T. J. R. Hughes. *The Finite Element Method: linear static and dynamic finite element analysis*. Dover publications, Mineola, New York, 2000. ISBN 0-486-41181-8.

[24] A. W. A. Konter. 'Advanced Finite Element Contact Benchmarks'. Technical Report Report No: FENET-UNOTT-DLE-09, Netherlands Institute for Metals Research, the Netherlands, 2005.

[25] D. J. Allman. 'A Compatible Triangular Element Including Vertex rotations for plane elasticity analysis'. *Comput Struct*, 19:1–8, 1984.

[26] D. J. Allman. 'Evaluation of the constant strain triangle with drilling rotations'. *Int J Numer Meth Eng*, 26:2645–2655, 1988.

[27] C. A. Felippa. 'A study of optimal membrane triangles with drilling freedoms'. *Comput Method Appl M*, 192:2125–2168, 2003.

[28] T. J. R. Hughes, L. P. Franca and M. Balestra. 'A new finite element formulation for computational fluid dynamics: V. Circumventing the Babuska-Brezzi condition: a stable Petrov-Galerkin formulation of the Stokes problem accommodating equal-order interpolations'. *Comput Method Appl M*, 59:85–99, 1986.

[29] D. S. Malkus and T. J. Hughes. 'Mixed finite element methods - Reduced and selective integration techniques: A unification of concepts'. *Computer Methods in Applied Mechanics and Engineering*, 15:63–81, 1978.

[30] T. Meinders, A. H. van den Boogaard and J. Huétink. 'Improvement of implicit finite element code performance in deep drawing simulations by dynamics contributions'. *J Mater Process Tech*, 134:413–420, 2003.

# Chapter 4

# A multi-layer element for simulations of laminated composite forming processes*


## Abstract

Continuous fibre reinforced thermoplastics offer a cost reduction compared to thermosets due to promising fast production methods like diaphragm forming and rubber pressing. Forming experiments of pre-consolidated four-layer 8H satin weave PPS laminates on a dome geometry demonstrated that inter-ply friction is a dominant parameter in forming doubly curved components. Therefore, simulations of this process of sequential draping the individual layers are invalid. A multi-layer element has been developed for efficient simulations of laminated composite forming processes with only one element in the thickness direction. Contact logic between the individual plies is avoided. The simulations were validated against the experiments mentioned and agree very well. The multi-layer membrane elements proved capable of predicting the material instabilities during forming. They appeared to be unsuited for realistic wrinkling simulations due to their lack of a bending stiffness.


*This chapter is based on: R.H.W. ten Thije and R. Akkerman. A multi-layer element for simulations of laminated composite forming processes. *Manuscript submitted to Composites Part A: Applied Science and Manufacturing*, with R.H.W. ten Thije as the principal author

## 4.1 Introduction

Continuous Fibre Reinforced Thermoplastics (CFRTP) have made their way into the aerospace industry, both as structural and non-structural components. Their usage will increase in the future due to the evolving low cost manufacturing techniques for these products. The ability to weld components in subsequent process steps is one of the main cost savers [1, 2]. CFRTP components are typically thin-walled and primarily made by forming layered pre-consolidated laminates through thermo-folding, pressing or diaphragm forming. These processes can introduce unacceptable shape distortions in the component upon forming, such as springback or wrinkling. Reduction of these shape distortions can be achieved by optimising the product and process conditions in the design phase. This requires accurate predictive models that can include complex process conditions and sophisticated material models. For these analyses, the finite element method is a well suited method.

Modelling each individual constituent of the laminate as a separate object is (yet) computationally too expensive for forming simulations of fibre reinforced materials. This discrete approach is limited to analyses on a mesoscopic level [3–5]. Although fabrics are discontinuous at lower length scales, an efficiently and accurately continuum model can be obtained by homogenisation of the mechanical properties [6, 7]. The continuum approach has proven to be successful and is widely used for forming simulations of fibre reinforced materials [8–12]. In the semi-discrete approach, bar or truss elements are added to standard continuum elements [13–15]. In this research, the continuum approach was adopted.

Forming experiments of pre-consolidated thermoplastic laminates with alternate lay-ups demonstrated that inter-ply friction is a dominant parameter when forming doubly curved components (*section 4.4*). Therefore, simulations of the process by sequential draping of the individual layers are invalid. Stacking several plies with contact logic and an appropriate friction characterisation between each layer is a logical next step. This approach was successfully used by some researchers [16, 17]. Stacking elements will cause models to grow rapidly. Combined with the computationally expensive contact logic and associated instabilities, this approach can result in unacceptable simulation times for large models.

Modelling the multi-layer laminate with a single element in the thickness direction is computationally more attractive than modelling the layers individually. The number of degrees of freedom decreases and a contact

logic algorithm between the individual layers is avoided. Lamers [18, 19] developed a triangular membrane element that contains multiple layers but is connected to the global finite element system with only nine degrees of freedom. The displacements of the individual layers were solved locally by an energy minimisation algorithm. The resulting element is fast, but failed to accurately capture the tool-ply interaction. This interaction can be of significant importance when simulating the forming of a thermoplastic laminated composite, as shown by Wijskamp [20, 21] and Soulat et al. [17]. In his research, Wijskamp recommended to use global degrees of freedom for at least the top and bottom ply of the multi-layer element for accurate modelling of the tool-ply interaction. Based on these recommendations, a new multi-layer element has been developed. The element can be regarded as a stacked pile of elements, in which the contact logic is replaced by constraints on the out-of-plane displacements. This element will be presented in the next section.

## 4.2 Multi-layer element

The multi-layer element presented here is an extension of the single-layer membrane element that was presented in by ten Thije [22]. The out-of-plane deformations are linear, while the in-plane deformations are of a quadratic form. This results in an element that remains planar during forming, which avoids midside node oscillations during simulations involving contact. The higher order in-plane displacement fields are inevitable, because the intra-ply shear locking problem has to be solved. Intra-ply shear locking is a numerical artefact, resulting in unrealistically high fibre stresses and spurious wrinkling. It can be solved either by using selective reduced integration or by using multi-field elements [22]. Both solutions are used in this research. The two-layer version of the element is shown in figure 4.1.

The layers of the multi-layer element do not separate during forming. Only the top layer of the element includes out-of-plane displacements and has 15 displacement degrees of freedom. The displacement of the subsequent layers is two dimensional and parallel to the top layer. These layers have 12 displacement degrees of freedom each. The multi-field version of the element has an additional internal node, which contains the degrees of freedom for the assumed fibre strain field(s). The three dimensional displacement $\mathbf{u}$ of the element is easily decomposed into a rigid rotation $\mathbf{G}$ and an in-plane displacement $\mathbf{u'}$, because the element is plane. This decomposition is graphically illustrated in figure 4.2. The element stresses and nodal forces are evaluated in the $xy$-plane, where the separate layers of the multi-layer element reduce to regular quadratic plane elements. Finally, the evaluated

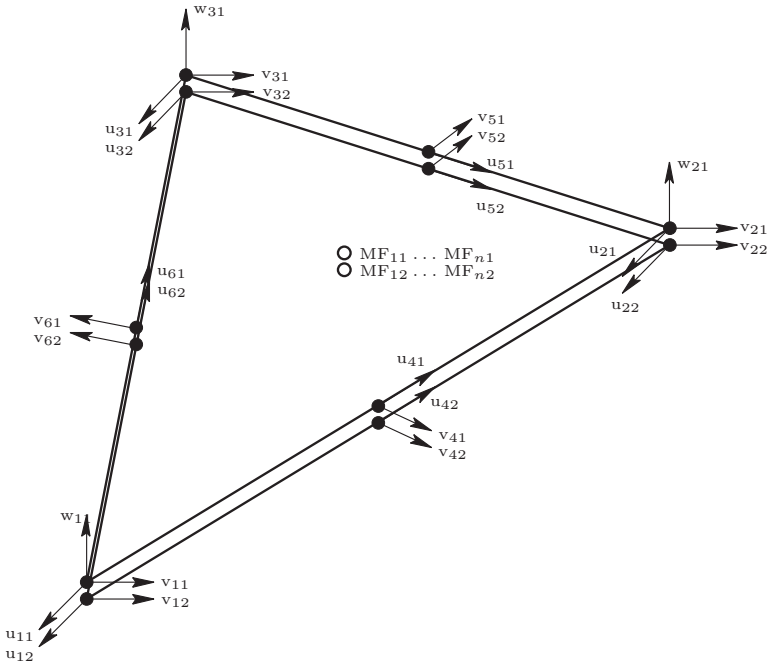


*Figure 4.1: The multi-layer element in a two-layer configuration.*

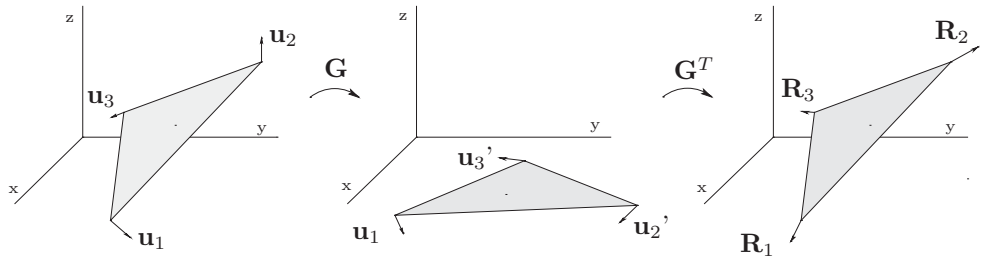


*Figure 4.2: Decomposition of the element displacements into a rotation and an in-plane displacement.*

nodal reaction forces $\mathbf{R}$ are rotated to the global coordinate system.

### 4.2.1 Layer and interface mechanics

The nodal displacements of the element layers are all expressed in the same local coordinate system after rotation to the $xy$-plane. The response of the element is found by processing the layers one by one. Figure 4.3 shows the evaluation of the layer with index $i$, attached to nodes $p$ and $q$.

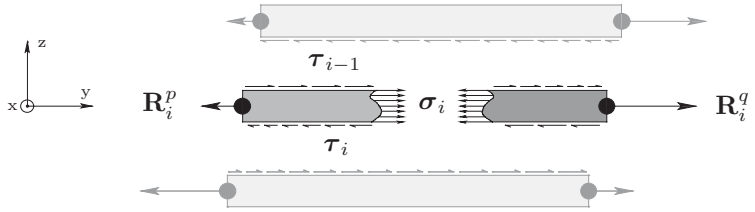


*Figure 4.3: Layer mechanics.*

In this figure, $\boldsymbol{\sigma}$ denotes the internal layer stress and $\boldsymbol{\tau}$, the boundary traction. The total reaction force vector $\mathbf{R}_i$ of the layer is given by:

$$\mathbf{R}_i = \mathbf{R}_i^{\ell} + \mathbf{R}_{i-1}^{IF} + \mathbf{R}_i^{IF}, \tag{4.1}$$

where $\mathbf{R}_i^{\ell}$ is the response of the layer material to the deformation. The forces $\mathbf{R}_{i-1}^{IF}$ and $\mathbf{R}_i^{IF}$ are contributions due to the interface tractions of the top and bottom interface respectively. The deformations are evaluated using the method introduced by ten Thije et al. [12]. The deformation of the layer is split into a rotational part and a stretch part for each fibre family that is present in the layer. This allows for exact tracking of the fibre directions during the simulation and avoids spurious layer deformations. The method proved to be accurate and robust in simulating large deformations in anisotropic materials. After evaluation of the stress, the layer contribution to the nodal reaction force is evaluated by:

$$\mathbf{R}_i^{\ell} = \int_{V_i} \mathbf{w}\overleftarrow{\nabla} : \boldsymbol{\sigma}_i \, dV_i, \tag{4.2}$$

with $\mathbf{w}$ the element weight functions and $V_i$ the layer volume.

The slip velocity $\mathbf{v}^{sl}$ on the interface is found by:

$$\mathbf{v}_i^{sl} = \mathbf{v}_{i+1}^{\ell} - \mathbf{v}_i^{\ell}, \tag{4.3}$$

where $\mathbf{v}^{\ell}$ denotes the layer velocity and $i$ the layer counter. An appropriate friction law relates the slip velocity to the interface traction $\boldsymbol{\tau}_i$. The friction can be of a Coulomb type if friction in dry fabrics is modelled or of a viscous type when lubricated friction between thermoplastics is considered. A popular model for lubricated friction is found by assuming that a film of a viscous material with a thickness $h$ is present between the two layers. Given the slip velocity, this assumption results in the following shear rate $\dot{\boldsymbol{\gamma}}$ in the film:

$$\dot{\boldsymbol{\gamma}}_i = \frac{\mathbf{v}_i^{sl}}{h}. \tag{4.4}$$

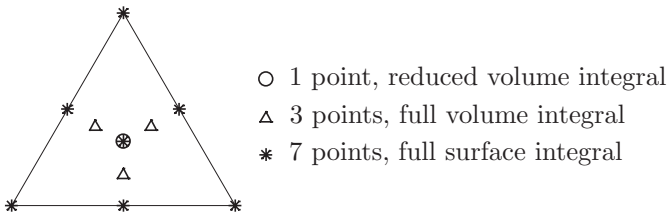


*Figure 4.4: Gaussian quadrature scheme for the multi-layer element.*

The traction $\boldsymbol{\tau}$ is then given by

$$\boldsymbol{\tau}_i = \eta \dot{\boldsymbol{\gamma}}_i, \tag{4.5}$$

with $\eta$ the viscosity of the polymeric film. The interface tractions are included as boundary conditions on the element faces:

$$\mathbf{R}_i^{IF} = \int_{\Gamma_i} \mathbf{w} \cdot \boldsymbol{\tau}_i \, d\Gamma_i, \tag{4.6}$$

with $\Gamma$ the surface area.

Gaussian quadrature schemes are used to evaluate the volume and surface integrals. Figure 4.4 shows the locations of the integration points of three different schemes. The three point numerical integration is used for full integration of the material contribution to the nodal forces, equation (4.2). The single point scheme is used for reduced integration of this equation. The seven point scheme is used to evaluate the nodal forces due to the interface tractions, equation (4.6). A six point scheme would be sufficient for this equation, but the seven point scheme avoids over- and undershoot of tractions at the nodes.

Forming simulations are generally split into smaller sub-steps or increments. The layers of the element move with respect to each other during these forming increments. The assumption that all layers remain parallel is only valid for small relative displacements. This is solved by re-mapping the mesh of the layers at the end of each increment. This process is schematically illustrated in figure 4.5. Each forming increment consists of an iterative, updated, Lagrangian procedure to find equilibrium, followed by a re-map of the mesh to align all layers in the vertical direction before starting the new increment. The re-map is a Eulerian operator, resulting in material movements with respect to the mesh. The state variables, stored in the integration points, are updated accordingly using a convection scheme. This convection scheme will be discussed next.

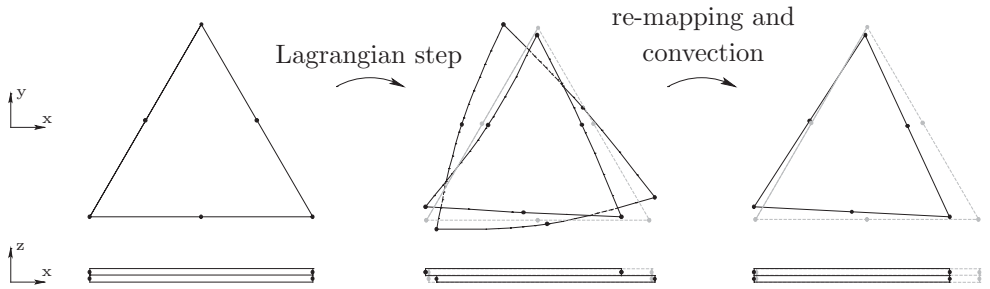


*Figure 4.5: Re-mapping and convection of a two-layer element after a Lagrangian step.*

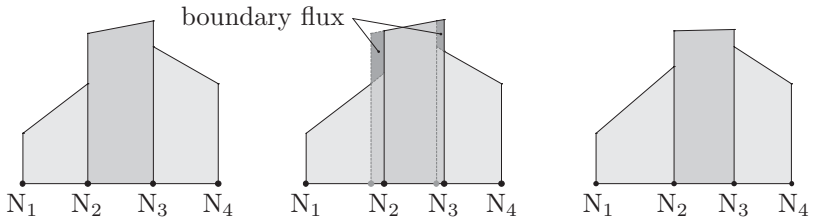


*Figure 4.6: Second order convection. From left to right the initial state, the mesh movement and the final state.*

### 4.2.2 Convection

Incremental displacements of the element are evaluated using an updated Lagrangian method. This is followed by a Eulerian step, in which the mesh is updated. The state variables are updated accordingly, using a second order convection scheme developed by Geijselaers [23]. The method convects linearly distributed element data, which are allowed to be discontinuous across the element borders. The convection is schematically illustrated in figure 4.6. Nodes two and three move, causing boundary fluxes in the element data. These fluxes are redistributed by the convection algorithm. The advection scheme is local, conservative, shows little diffusion and is stable up to Courant numbers of 0.95. This number indicates stability up to convective displacements of almost the size of the element.

The convection algorithm has been implemented in the multi-layer element routines. The element data of the three point integration scheme from figure 4.4 are directly suitable as input for the convection algorithm, because three points fully determine a linear surface. The element data of the single and seven point integration scheme are first converted to a linear field by a least

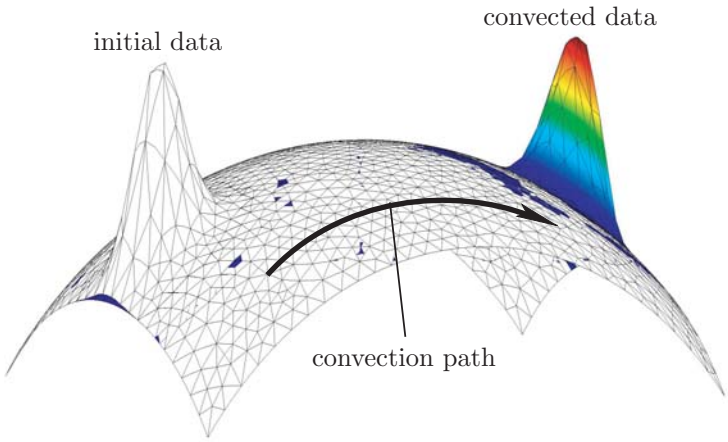


*Figure 4.7: Convection of element data through a doubly curved mesh.*

squares fit and subsequently convected. The incremental integration point values are found by interpolation and added to the integration point data.

The convection algorithm was tested on the spherical surface given by the equations

$$R^2 = (x-2)^2 + y^2, \qquad R = 3, \qquad x = [0,4], \qquad y = [-1.5, 1.5]. \tag{4.7}$$

The initial values of the field to be convected are given by a Gaussian bump equation:

$$f = 0.01^{4((x-0.5)^2+y^2)}. \tag{4.8}$$

The surface is randomly meshed with 1379 two-layer elements. The top layer was fixed and the bottom layer was given a total displacement of 3 in the direction tangential to the convection path indicated in figure 4.7. The displacement was divided into 200 substeps. The maximum Courant number during convection was 0.49. Figure 4.7 shows the meshed surface with the initial and convected data plotted as vertical displacements.

The initial and convected data values along the convection path were extracted from the results and plotted in figure 4.8. The convected data was shifted by the total displacement to compare the initial and convected results. The results indicate that the data is accurately convected, given the type of computation and the level of discretisation. The values shown in figure 4.7 and 4.8 are nodal values, extrapolated from the integration points. The data would have been discontinuous across the element boundaries if the integration point values would have been plotted.

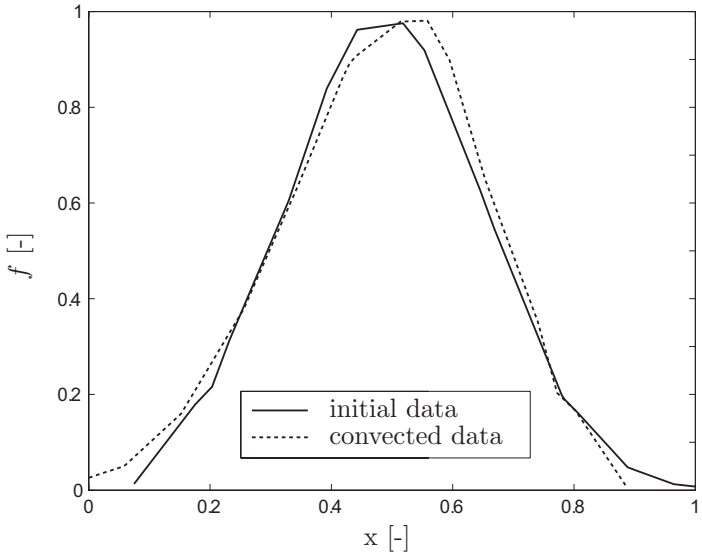


*Figure 4.8: Initial and convected values of the Gaussian bump.*

## 4.3 Material characterisation

Material characterisation experiments were performed on four-layered PPS (polyphenylene sulfide) laminates, reinforced with a glass fibre 8H satin weave (Ten Cate Cetex© SS303). The intra-ply properties were investigated in the research of Lamers [18], using trellis frame experiments. The inter-ply friction properties were determined with pull-out experiments. The experimental results, the material models used to represent the response and the fitted material parameters are given in the next section.

### 4.3.1 Intra-ply properties

The trellis frame experiment is used to impose a pure shear deformation on a biaxial fabric. The trellis frame rig is shown on the left in figure 4.9. The fibre directions are aligned with the frame and the upper crosshead moves with a constant velocity in the vertical direction. The rate of deformation increases during the test, due to the frame geometry. Several yarns near the central region were removed to reduce wrinkling in the fabric. The right hand side of figure 4.9 shows the fabric after the experiment.

Figure 4.10 shows the experimental results found by Lamers [18], using trellis frame experiments, at a temperature of 300 °C and a crosshead velocity of 1000

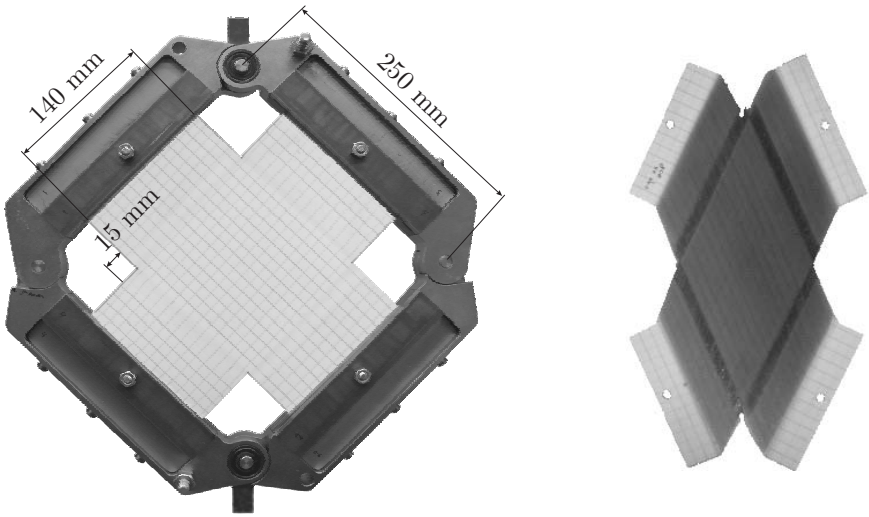


*Figure 4.9: The trellis frame experiment. On the left the frame and composite prior to testing and on the right the composite after testing [18].*

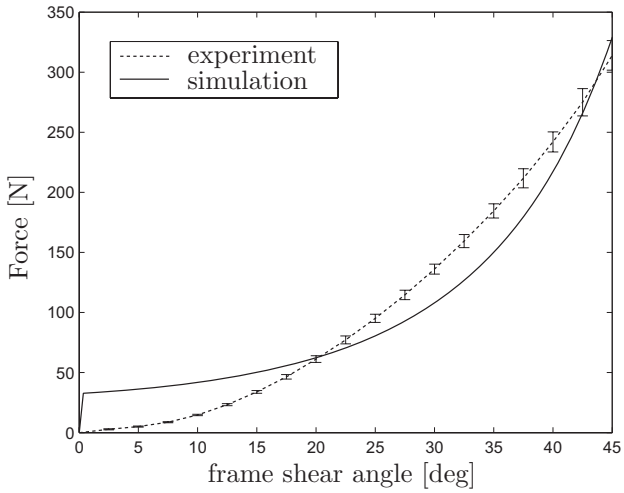


*Figure 4.10: Experimental [18] and simulated response of the trellis frame experiment. The error bars represent the standard deviation.*

| | | | | | |
|---|---|---|---|---|---|
| layer thickness | [mm] | 0.2375 | $\eta_0$ | [MPa·s] | 1.55 |
| fibre volume fraction (2x) | [-] | 0.25 | $C$ | [ms] | 6.2 |
| matrix volume fraction | [-] | 0.50 | $n$ | [-] | 0.2 |
| fibre stiffness | [GPa] | 72.4 | | | |

*Table 4.1: Intra-ply properties of the 8H satin weave PPS composite and fitted material parameters at 300 °C.*

mm/s. The material is characterised by using a material model, which consists of several material fractions. The deformation is equal for each fraction $j$ and each fraction contributes to the total stress proportional to its volume fraction $\nu_j$:

$$\boldsymbol{\sigma} = \Sigma_j \nu_j \boldsymbol{\sigma}_j, \tag{4.9}$$

where the sum of the volume fractions equals unity. The volume fraction of the biaxial reinforcement is estimated at 50% and is modelled as linearly elastic with a Young's modulus of 72.4 GPa. This value is found in literature for E-glass fibres [24]. The matrix material is modelled as a viscous material, for which the stress is given by

$$\boldsymbol{\sigma} = p\mathbf{I} + 2\eta\mathbf{D}^d, \tag{4.10}$$

in which $p$ denotes the hydrostatic pressure, $\mathbf{I}$ the second order unit tensor, $\eta$ the viscosity and $\mathbf{D}^d$ the deviatoric part of the rate of deformation tensor. The viscosity is shear rate dependent and is modelled with a Cross model:

$$\eta = \frac{\eta_0}{1 + (C\dot{\gamma})^n}, \tag{4.11}$$

in which $\eta_0$, $C$ and $n$ are material parameters and $\dot{\gamma}$ the equivalent shear rate given by:

$$\dot{\gamma} = \sqrt{\tfrac{2}{3}\mathbf{D} : \mathbf{D}}. \tag{4.12}$$

The fitted material parameters are found in table 4.1 and the simulated response of the trellis frame experiment is plotted in figure 4.10.

### 4.3.2 Tool-ply and inter-ply friction

Tool-ply friction and inter-ply friction were measured using pull-out experiments. The pull-out setup was designed to experimentally determine the influence of normal pressure, temperature and relative velocity on the frictional behaviour. Pre-consolidated laminates were clamped between two

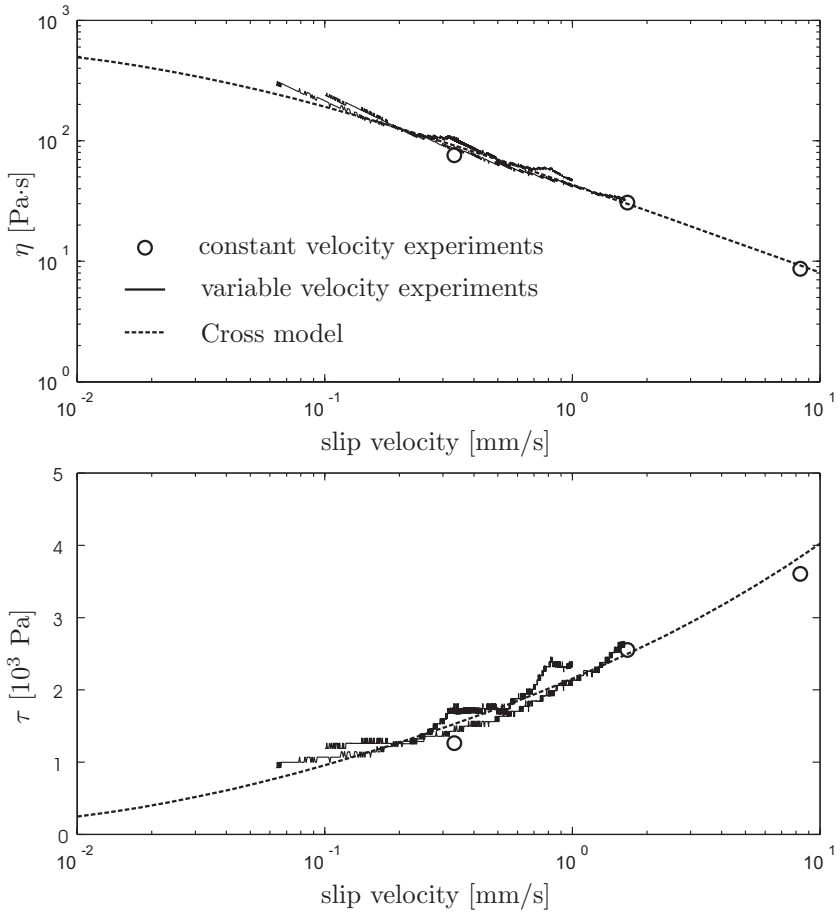


*Figure 4.11: Viscosity of the resin film and the interface traction.*

| | | | | | |
|---|---|---|---|---|---|
| film thickness | [mm] | 0.02 | $\eta_0$ | [Pa·s] | 750 |
| $C$ | [s] | 0.833 | $n$ | [-] | 0.75 |

*Table 4.2: Cross model parameters for the tool-ply and inter-ply friction model at 305 °C.*

heated polished platens. Depending on the type of friction to be measured, the complete laminate or a set of plies were then pulled from between these platens. Details of the experimental setup were presented by Akkerman et al. [25].

The tool-ply and ply-ply frictional behaviour are assumed to be equal. Experiments indicated that the steady state friction on these two surface combinations is almost equal with an observed maximum deviation around 10%. The normal pressure on the laminate, exerted by the tools, is relatively low during the most part the press cycle. Pressure starts to build up only at the end of the cycle. For this reason, the experimental results at a relatively low normal pressure of 20 kPa were used for characterisation of the friction.

Fully hydrodynamic lubrication is assumed between two surfaces, which are in contact. A thin film of resin with an assumed constant thickness is sheared by the displacement of the surfaces, resulting in a traction $\boldsymbol{\tau}$ given by equation (4.5). The assumption of fully hydrodynamic lubrication is confirmed by the work of Murtagh [26] and successfully used in simulations done by other researchers [17, 27]. The viscosity of the resin film is modelled with the Cross model given by equation (4.11). The parameters of this model and the assumed film thickness are given in table 4.2.

Figure 4.11 shows the experimental results and the simulated results of the pull-out experiments. The experiments were performed at a normal pressure of 20 kPa and a temperature of 305 °C. Experiments were conducted at a constant and a varying pull-out velocity. The experiments with a constant velocity were performed in triplicate and the averaged results are plotted in figure 4.11. The results of two additional experiments, in which the pull-out velocity was varied, are plotted in this figure as well. The viscosity of the resin film in the experiments is found by assuming the same film thickness as used in the model. The lubricated friction model, combined with the Cross model for the film viscosity, gives a proper description of the experimental results.

## 4.4 Drape simulations and validation

Forming experiments on a dome geometry were performed at Fokker AESP in Hoogeveen, the Netherlands. Four-layered glass weave reinforced PPS laminates with varying lay-ups were formed using the Rubber Press Forming (RPF) process. Shear angles and contours of these products were determined and compared with simulation results.

### 4.4.1 Experimental setup

Ten Cate Advanced Composites, Nijverdal, the Netherlands, supplied a dedicated glass fibre 8H satin weave for experiments. A standard Cetex© SS303 weave was equipped with blue tracer yarns that were woven into the

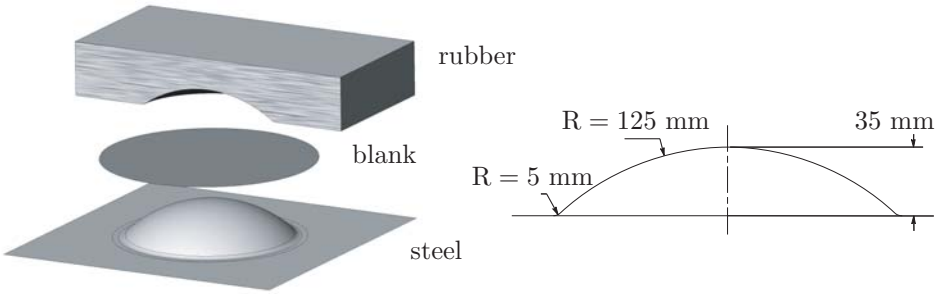


*Figure 4.12: Geometry of the dome mould.*

| | | | | | |
|---|---|---|---|---|---|
| press velocity 1 | [mm/s] | 100 | laminate temp. | [°C] | 325 |
| press velocity 2 | [mm/s] | $\sim 10$ | heating time | [s] | 180 |
| blank diameter | [mm] | 217.5 | steel mould temp. | [°C] | 166 |

*Table 4.3: Parameters of the experimental setup.*

glass weave in a 10 x 10 mm grid pattern. The volume fraction of the tracers is less than 5% and their mechanical influence during forming is considered to be negligible. The experimental setup and the dimensions of the mould are shown in figure 4.12.

The circular blanks with a diameter of 217.5 mm were cut from pre-consolidated laminates. They were loosely clamped at 4 points on the circumference and heated by infra-red panels. The temperature of several laminates was logged using a thermocouple wire. It took approximately 80 seconds for the laminate to reach 300 °C. It was then heated for another 100 seconds, during which the temperature gradually increased to 325 °C. The laminate was then formed by moving down the rubber mould with a speed of 100 mm/s. A few millimetres upon closing, the speed drops to approximately 10 mm/s. The press then switches to a pressure controlled movement.

Four different lay-up configurations were formed in triplicate. They range from a Cross-Ply (CP) $[0/90,90/0]_s$ configuration to a Quasi-Isotropic (QI) $[0/90,45/\text{-}45]_s$ configuration with increments of 15°. The lay-ups are presented in table 4.4. They will be referred to as laminate A through D. The parameters of the experimental setup are found in table 4.3.

### 4.4.2 Finite element simulation setup

The multi-layer element was implemented in an in-house finite element code written in MATLAB©. One quarter of the blank was meshed with an unstructured mesh of 392 multi-layer elements. Symmetry was prescribed at the axes. The material model of the individual plies and the corresponding parameters are found in section 4.3.1 and table 4.1 respectively. The inter-ply frictional model and the corresponding parameters are found in section 4.3.2 and table 4.2 respectively. Contact between the mould and the laminate is modelled using a penalty formulation. Tool-ply friction was not implemented in the experimental FE code. The in-plane ply properties and the ply-ply friction are expected to dominate the formability of the laminated composite. The closing velocity of the female mould was set to 100 mm/s.

### 4.4.3 Experimental results

The experimental results shown in figure 4.13 clearly indicate that the behaviour of the layered composites heavily depends on the lay-up. The cross-ply laminate was formed without wrinkles. Laminate B shows a few small wrinkles. The number of wrinkles and their size increases if the offset in the lay-up angle increases. The QI laminate shows severe wrinkling. The wrinkling patterns and wrinkle sizes were very consistent among different laminates with the same lay-up. The contour of the deformed shape tends towards a more circular shape when the offset in the lay-up angle increases. This is illustrated in figure 4.14, where in each quadrant the deformed contour of one of the experimental products has been plotted. The dotted line is a circle that has been fitted on the deformed contour of the QI laminate.

Both layers of the cross-ply laminate deformed equally in the bias direction, as seen in figure 4.14. The maximum deviation from the circle is approximately 6 mm. The deformed contour of the QI laminate is nearly circular. This indicates that there was hardly any inter-ply slip, otherwise the individual plies would have deformed in their bias direction as well. This deformation was blocked by the stiff fibres in the other plies. The loads are transferred between the individual plies by the interface tractions. As a consequence, severe wrinkling occurred.

The movement of the rubber mould was stopped at 10.6, 7.3 and 4 mm upon closing for three additional QI laminates, to visualise the forming of wrinkles. Figure 4.15 shows the development of two wrinkles in the flange. This is the point where the laminate was loosely clamped and most wrinkles are initiated. At the clamping point, the laminate is not as thoroughly heated

A. $[0/90,90/0]_s$, cross-ply
B. $[0/90,75/\text{-}15]_s$
C. $[0/90,60/\text{-}30]_s$
D. $[0/90,45/\text{-}45]_s$, quasi-isotropic

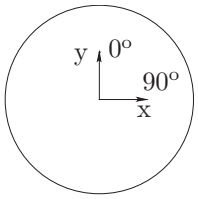


*Table 4.4: The four lay-ups used in the experiments.*

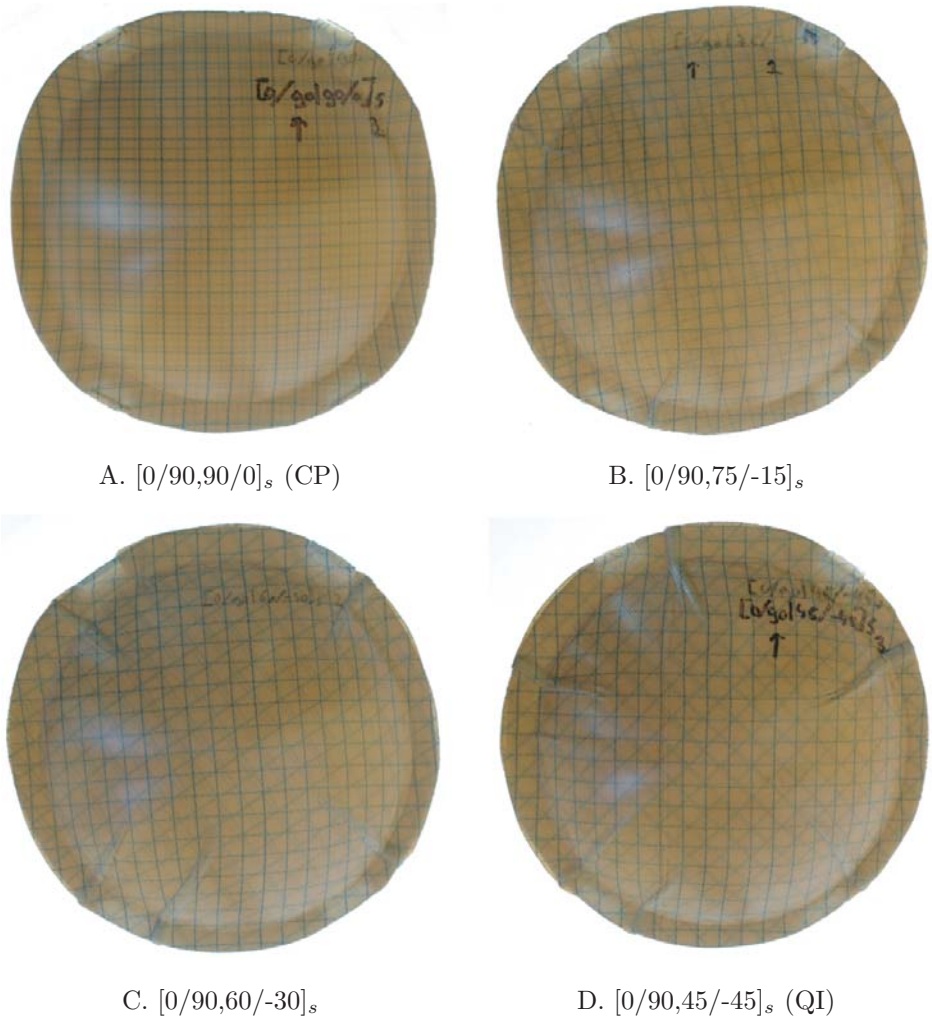

A. $[0/90,90/0]_s$ (CP)
B. $[0/90,75/\text{-}15]_s$
C. $[0/90,60/\text{-}30]_s$
D. $[0/90,45/\text{-}45]_s$ (QI)

*Figure 4.13: Top view of the four composite laminates after forming. Wrinkling increases with an increasing offset in lay-up angle.*

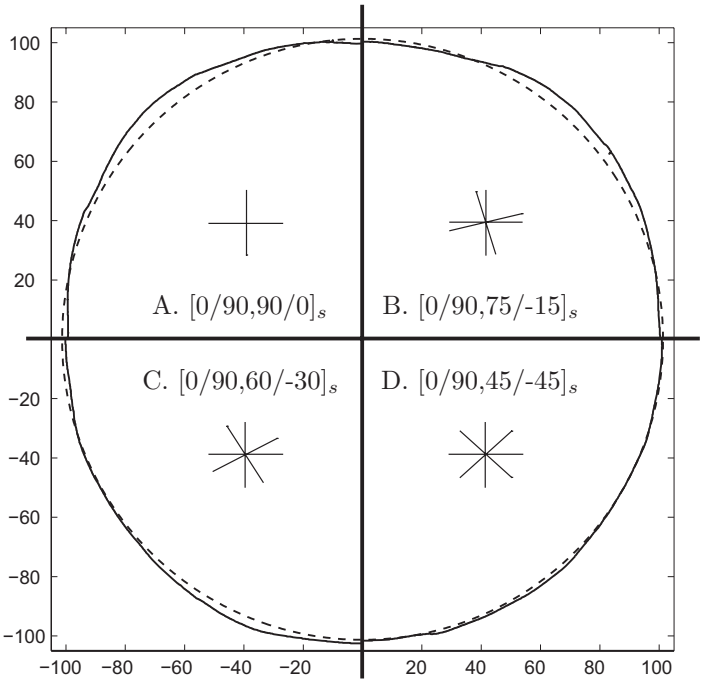


*Figure 4.14: Contours of the experimental products. The dotted line is a circle fitted on the QI laminate contour.*


*Figure 4.15: Development of wrinkles in a QI laminate at different stages during the rubber pressing process.*

as the rest of the composite. This can be observed by examining the local laminate colour. The colour of the PPS matrix material evolves from a creamy colour to a brown colour during the RPF process. The colour at the clamping points is less brownish, indicating that the temperature during the heating process was lower. However, the material was still heated well above the melting temperature, because local ply slip and laminate deformation has been observed at these points. Local temperature measurements could provide more information on the level of heating. In these particular experiments, it seems that the clamping points do not significantly increase the number and size of the wrinkles. However, they do determine the wrinkling pattern. Wrinkles initiate near the clamping points.

Shear angles between the two fibre families in the top layer have been measured along a line, intersecting with the dome surface in the bias direction. The results are depicted in figure 4.16. The location of the line is indicated in the top left sub-figure. A zero shear angle indicates that there is no bias deformation, a shear angle of -10$^o$ indicates that the angle enclosed between the two fibre families decreased from the original 90$^o$ to 80$^o$ degrees. The conclusions that can be drawn from this figure agree with the conclusions drawn from the contour plots. The cross-ply laminate shows significant in-plane shear deformation, resulting in a smooth product without wrinkles. As the offset in the lay-up angle increases, the inter-ply friction restricts this deformation mode and the laminate starts to wrinkle. The location of the wrinkles is indicated in figure 4.16 by the thick black line at the bottom of the figure.

### 4.4.4 Simulation results

The simulation results of the forming of the cross-ply laminate agreed very well with the experimental results. The maximum deviation found between the deformed contours of the simulation and the experiment was 0.25 mm. The predicted shear angle is shown in figure 4.16. The agreement between the simulated and experimentally obtained shear angles is reasonably good. The simulation slightly over-estimates the shear deformation. The experimental results show that there is no significant shear deformation in a circular area with a radius of 20 mm around the centre of the dome. This could be a result of rapid cooling of the laminate. It touches the relatively cold steel mould first and the subsequent solidification restricts the formability. Another explanation could be the presence of tool-ply friction. Both effects were neglected in the simulation.

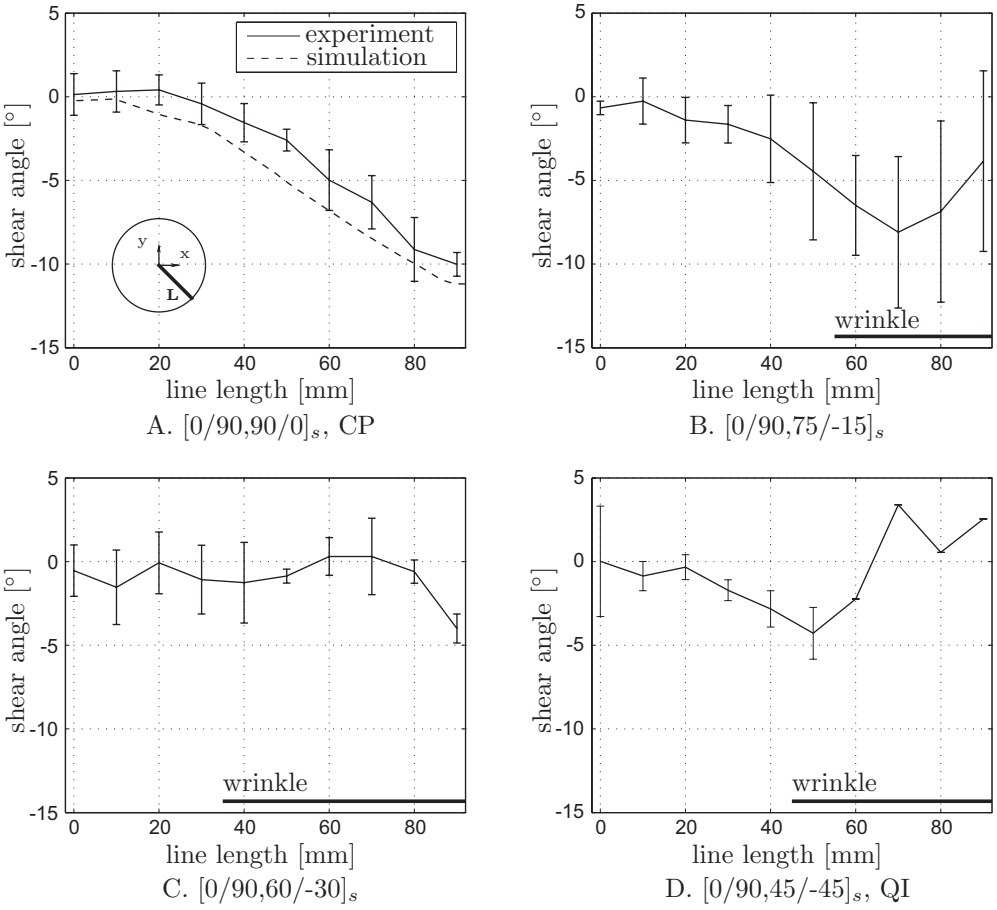


*Figure 4.16: Shear angles of the top layer along the indicated line L at 135°. The location of the wrinkles is indicated by the thick black line. The error bars indicate the standard deviations. Severe wrinkling of the QI laminate allowed the shear angle measurement at the last four points of one product only. This causes the absence of standard deviation at these points.*

Two simulated deformed shapes of the QI laminate are shown in figure 4.17. The figures are snapshots, taken 10 and 5 mm before completion of the process, respectively. The compressive membrane stresses induced by the forming into the doubly curved shape cause material instabilities and the laminate starts to wrinkle. The top figure shows one large and one small wrinkle, just beside the lines of symmetry. This is caused by the absence of bending stiffness in the membrane elements. The wrinkles initiate along lines where the mesh is the least unstructured.

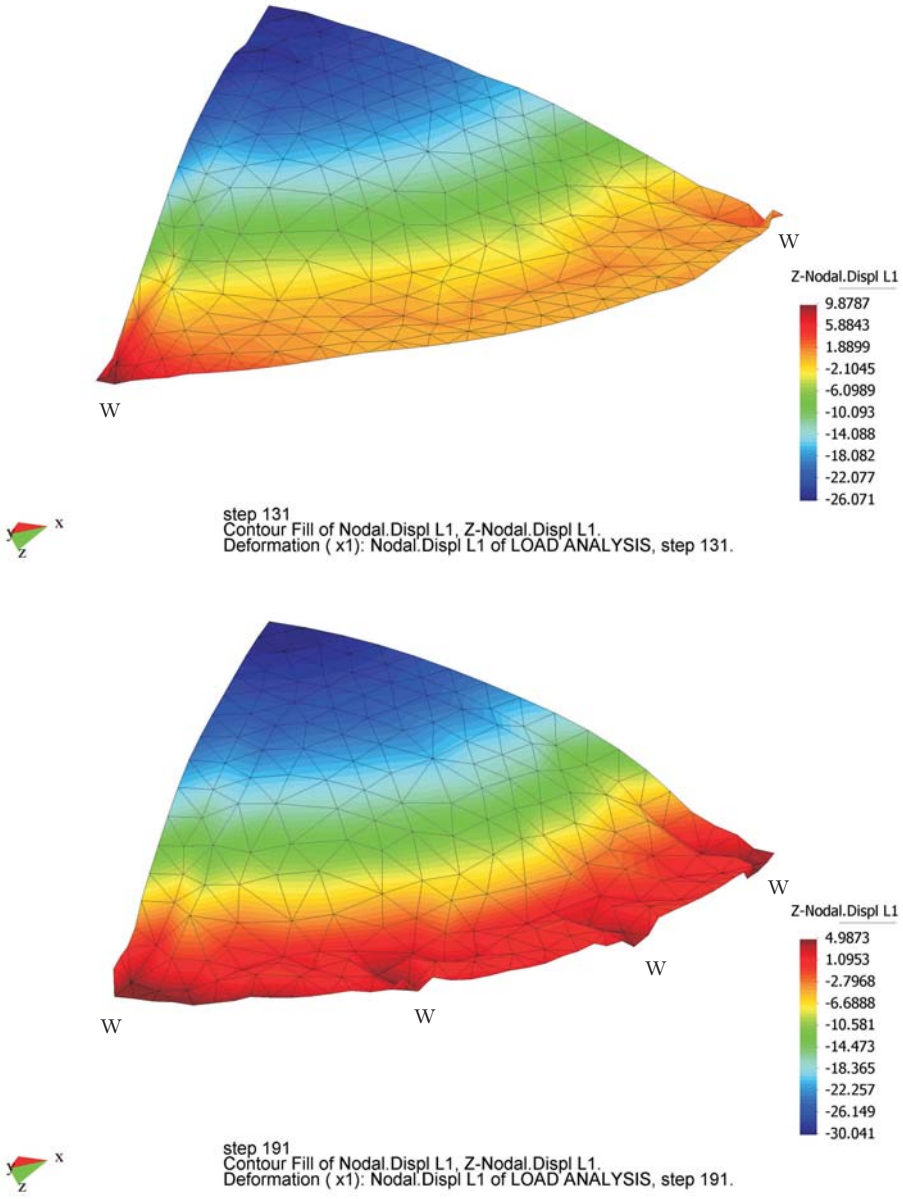


*Figure 4.17: Forming simulation of a quasi-isotropic laminate at 10 and 5 mm upon mould closure.*

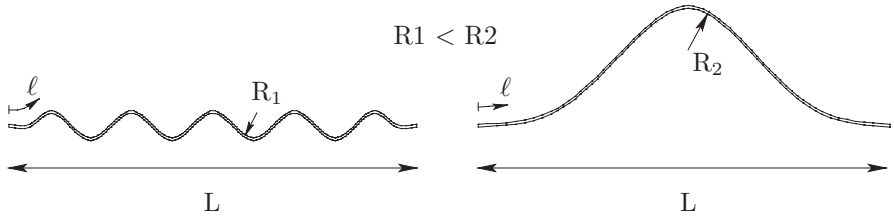


*Figure 4.18: The stored membrane energy is equal for both laminates. The bending energy of the laminate on the left is higher.*

The bottom figure shows that two more wrinkles have developed as a result of increasing compressive stresses. Instead of the growth of the existing wrinkle, the large wrinkle has split into multiple smaller wrinkles. This behaviour is also due to the absence of bending stiffness. In figure 4.18, two cross-sections of laminates are plotted with an equal thickness, length $\ell$ and projected length L. This results in an equal amount of membrane energy stored in the laminates, if elastic deformation is assumed. The bending energy stored in the multiple small wrinkles in the laminate on the left is higher than the bending energy stored in the large bend in the laminate on the right. The preferred deformed shape of the laminate then would be the latter one. However, simulations with membrane elements neglect the bending stiffness and will often deform in a similar manner as the laminate plotted at the left hand side of figure 4.18.

## 4.5 Discussion

Shell elements should be used for a realistic wrinkling behaviour in simulations. The element size must at least be one third of the smallest wrinkle that can occur in the composite. Altogether, this will increase the simulation time significantly. In addition to that, characterisation of the bending behaviour of thermoplastic laminates is still in its infancy. An alternate solution would be the use of a wrinkling indicator. It is often sufficient to predict the occurrence of wrinkling. A wrinkling indicator predicts wrinkling, based on the local stress state in the element and the local mesh geometry. A very rough wrinkling indicator is the second principal stress $S_2$. The plane stress assumption causes the third principal stress to be absent. The second principal stress is the minimum value of the two principal stresses left. Theoretically, wrinkling occurs if this stress becomes negative and bending stiffness is neglected, like in membrane elements. The minimum value for $S_2$ found during the simulations is plotted in figure 4.19. The simulations predicting higher compressive stresses

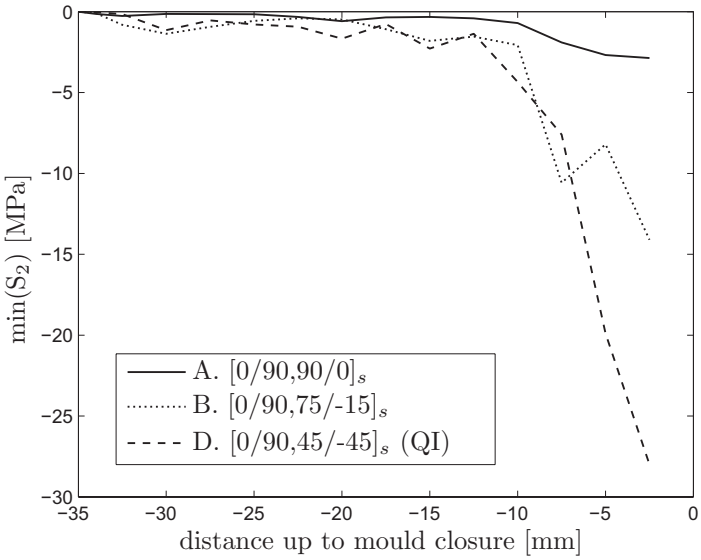


*Figure 4.19: Minimum 2nd principal stress: a rough wrinkling indicator.*

$S_2$ indeed correspond to press trials with more severe wrinkling. The values of $S_2$ for the laminates B and D increases significantly between 15 and 10 mm upon mould closure. Wrinkles start to develop in the actual specimen at this stage of the forming process as well. The compressive stress in the wrinkle-free cross-ply laminate, laminate A, is considerably lower.

The development of a reliable and robust wrinkling indicator is not a trivial task, but can speed up the simulations significantly. This allow for fast simulations with relatively coarse meshes, which can still provide information on the feasibility of the desired mould shape or lay-up. Dessenberg and Tucker [28] successfully used forming limit diagrams to predict the presence of defects after the preforming of random fibre mats. These forming diagrams were constructed using principal stretch ratios and indicate the feasible forming regions. Wrinkling or tearing is likely to occur outside the feasible region, with an increased risk if the distance to the feasible region increases. Skordos et al. [15] numerically and experimentally investigated the formability of a woven fabric, which was draped on a hemispherical mould. A relation between the wrinkling strain, a compressive principal strain, and the amount of wrinkles in the experimental product was shown in this research. Lin et al. [29] successfully minimised the wrinkling in a textile by varying blankholder forces. Lin et al. stated that the amount of wrinkling depends on the compressive forces and the shear deformation of the fabric. The question rises whether

the two principal strains are sufficient as input parameters for the forming limit diagram of fibre reinforced sheet material. Although successful in metal forming simulations, a more complex diagram might be necessary to define the forming envelope of these highly anisotropic materials. Virtual tests can provide useful insight on this aspect as well. Complex numerical models on a repetitive unit cell level can accurately mimic the response of a fabric and can avoid experimental tests that are elaborate or difficult to perform [5, 30].

The intra-ply shear locking problem has been solved successfully. The fibre stresses are not unrealistically high, as in the research of Lamers [18]. Lamers observed fibre stresses of 3 GPa during drape simulations on a double dome geometry. The maximum fibre stresses that occurred during the simulations in this research typically ranged from 5 MPa for the cross-ply laminate to 50 MPa for the QI-laminate. A trial simulation, with the selective reduced integration switched of, resulted in fibre stresses in the GPa-range. The elements using selective reduced integration and the multi-field elements gave nearly similar results. However, the convergence behaviour of the multi-field elements is significantly better and hence allowed for larger incremental mould displacements. These observations correspond to the conclusions presented by ten Thije and Akkerman [22].

The execution speed of the experimental MATLAB© code is poor. The running times of the simulations using the multi-field elements typically ranged from 20 to 24 hours on a PC with a 3400 MHz AMD processor and 1 GB of RAM. The simulations that used elements with selective reduced integration were typically 30 to 60% slower. Based on experiences in the past, a dedicated code can improve the execution speed with at least two decades.

## 4.6 Conclusions

Inter-ply friction during forming of pre-consolidated laminated composites is of significant importance. Quasi-isotropic laminates ($[0/45,45/\text{-}45]_s$) that were formed using the rubber press forming process, showed hardly any inter-ply slip due to high interface traction. This caused severe wrinkling of the laminate. The inclusion of inter-ply friction is required for accurate forming simulations of these pre-consolidated laminated composites. Therefore, a multi-layer membrane element was developed. The top layer of this element has out-of-plane displacement degrees of freedom, while the other layers of the element can only move in-plane, parallel to the top layer. This avoids the use of a computationally expensive contact logic algorithm between the layers, as would be necessary for stacked elements. The simulation results agree

very well with the experimental results for a cross-ply laminate ($[0/90,90/0]_s$), where wrinkling is absent.

The simulation with the membrane multi-layer element accurately predicted the point at which wrinkling started. Accurate and realistic simulations of the wrinkling behaviour is not possible, because the elements lack bending stiffness. Shell elements should be used for this, but are expected to significantly increase the simulation times. It is recommended to develop and implement Forming Limit Diagrams (FLD) instead. Predicting the occurrence of defects is more important than the exact shape of the defect. A procedure on how to construct such an FLD for a continuous fibre reinforced material is not available yet. The assumption that the FLD depends on the principal strains only, as in the metal forming approach, is most doubtful for these materials.

The intra-ply shear locking problem has been solved successfully. No unrealistically high fibre stresses were observed. Both elements using selective reduced integration and the multi-field elements were used in this research. Both gave similar results, but the multi-field element allows for larger incremental mould displacements and hence significantly shorter simulation times.

### Acknowledgements

The authors wish to thank Stork Fokker AESP and Ten Cate Advanced Composites for extending complete cooperation during the experimental trials.

## Bibliography

[1] A. R. Offringa. 'Thermoplastic composites - rapid processing applications'. *Compos Part A-Appl S*, 27:329–336, 1996.

[2] A. Offringa. 'Thermoplastics in aerospace, a stepping stone approach'. Technical report, Stork Fokker AESP B.V., 2006.

[3] B. Ben Boubaker, B. Haussy and J. F. Ganghoffer. 'Discrete models of fabrics accounting for yarn interactions'. *Eur J Comput Mech*, 14:653–676, 2005.

[4] D. Durville. 'Numerical simulation of entangled materials mechanical properties'. *J Mater Sci*, 40:5941–5948, 2005.

[5] S. V. Lomov, D. S. Ivanov, I. Verpoest, M. Zako, T. Kurashiki, H. Nakai and S. Hirosawa. 'Meso-FE modelling of textile composites: Road map, data flow and algorithms'. *Compos Sci Technol*, 67:1870–1891, 2007.

[6] S.-W. Hsiao and N. Kikuchi. 'Numerical analysis and optimal design of composite thermoforming process'. *Comput Method Appl M*, 177:1–34, 1999.

[7] X. Peng and J. Cao. 'A dual homogenization and finite element approach for material characterization of textile composites'. *Compos Part B-Eng*, 33:45–56, 2002.

[8] A. Spencer. 'Theory of fabric-reinforced viscous fluids'. *Compos Part A-Appl S*, 31:1311–1321, 2000.

[9] W.-R. Yu, P. Harrison and A. Long. 'Finite element forming simulation for non-crimp fabrics using a non-orthogonal constitutive equation'. *Compos Part A-Appl S*, 36:1079–1093, 2005.

[10] X. Peng and J. Cao. 'A continuum mechanics-based non-orthogonal constitutive model for woven composite fabrics'. *Compos Part A-Appl S*, 36:859–874, 2005.

[11] P. Xue, X. Peng and J. Cao. 'Non-orthogonal constitutive model for characterizing woven composites'. *Compos Part A-Appl S*, 34:183–193, 2003.

[12] R. H. W. ten Thije, R. Akkerman and J. Huétink. 'Large deformation simulation of anisotropic material using an updated Lagrangian finite element method'. *Comput Method Appl M*, 196:3141–3150, 2007.

[13] S. Reese. 'Meso-macro modelling of fibre-reinforced rubber-like composites exhibiting large elastoplastic deformation'. *Int J Solids Struct*, 40:951–980, 2003.

[14] S. B. Sharma and M. P. F. Sutcliffe. 'A simplified finite element model for draping of woven material'. *Compos Part A-Appl S*, 35:637–643, 2004.

[15] A. A. Skordos, C. M. Aceves and M. P. F. Sutcliffe. 'A simplified rate dependent model of forming and wrinkling of pre-impregnated woven composites'. *Compos Part A-Appl S*, 38:1318–1330, 2007.

[16] A. K. Pickett, G. Creech and P. de Luca. 'Simplified and advanced simulation methods for prediciton of fabric draping'. *Eur J Comput Mech*, 14:677–691, 2005.

[17] D. Soulat, A. Cheruet and P. Boisse. 'Simulation of continuous fibre reinforced thermoplastic forming using a shell finite element with transverse stress'. *Comput Struct*, 84:888–903, 2006.

[18] E. A. D. Lamers. *Shape distortions in fabric reinforced composites due to processing induced fibre reorientation.* Ph.D. thesis, University of Twente, the Netherlands, 2004. ISBN 90-365-2043-6.

[19] R. Akkerman, E. A. D. Lamers and S. Wijskamp. 'An integral process

model for high precision composite forming'. *Eur J Comput Mech*, 4:359–378, 2006.

[20] S. Wijskamp, E. A. D. Lamers and R. Akkerman. 'Residual stresses in rubber formed thermoplastic composites'. In *Proc 6th Int ESAFORM Conf*, pages 855–858. Nuova Ipsa Editore, Palermo, Italy, 2003. ISBN 88-7676-211-6.

[21] S. Wijskamp. *Shape distortions in composite forming*. Ph.D. thesis, University of Twente, the Netherlands, 2005. ISBN 90-365-2175-0.

[22] R. H. W. ten Thije and R. Akkerman. 'Solutions to intra-ply shear locking in finite element analyses of fibre reinforced materials'. *Pre-print submitted to Compos Part A-Appl S*, 2007.

[23] H. J. M. Geijselaers. 'A second order discontinuous Galerkin method for advection on unstructured triangular meshes'. *Commun Numer Meth En*, 19:275–284, 2003.

[24] S. T. Peters, editor. *Handbook of Composites*. Chapmann and Hall, 1998. ISBN13: 9780412540202.

[25] R. Akkerman, M. P. Ubbink, M. B. de Rooij and R. H. W. ten Thije. 'Tool-Ply Friction In Composite Forming'. In *Proc 10th Int ESAFORM Conf*. 2007.

[26] A. M. Murtagh, M. R. Monaghan and P. Mallon. 'Investigation of the interply slip process in continuous fibre thermoplastic composites'. In *Proc 9th ICCM Conf*. 1993.

[27] S. P. McEntee and C. M. ÓBrádaigh. 'Large deformation finite element modelling of single-curvature composite sheet forming with tool contact'. *Compos Part A-Appl S*, 29:207–213, 1998.

[28] R. B. Dessenberger and C. L. Tucker III. 'Ideal forming analysis for random fiber preforms'. *J Manuf Sci E-T ASME*, 125:146–153, 2003.

[29] H. Lin, J. Wang, A. C. Long, M. J. Clifford and P. Harrison. 'Predictive modelling for optimization of textile composite forming'. *Compos Sci Technol*, article in press, 2007. Doi:10.1016/j.compscitech.2007.03.040.

[30] P. Badel, E. Vidal-Sallé and P. Boisse. 'Computational determination of in-plane shear mechanical behaviour of textile composite reinforcements'. *Comp Mater Sci*, article in press, 2007. Doi:10.1016/j.commatsci.2007.01.022.

# Chapter 5

# Conclusions

Forming processes of single-layer and multi-layer composite materials have been successfully simulated using the Finite Element (FE) method. A new non-linear FE formulation allows for accurately simulations of large deformations of highly anisotropic materials. Solutions were presented to prevent intra-ply shear locking, a numerical artefact in composite forming simulations. A multi-layer element was developed for efficient simulations of laminated composite forming processes with only one element through the thickness.

Classical stress rate types, such as the Jaumann rate, are inadequate for continuum approaches to composite forming simulations due to the incorrect updating of the fibre directions. Instead, the deformation gradient should be decomposed into a rotation tensor and a stretch tensor for each fibre family present in the material. Stresses are computed using invariant local stress and stiffness tensors. This leads to a simple and straightforward implementation of constitutive laws.

Consistent tangent matrices improve the speed of complex, implicit simulations significantly. For highly anisotropic materials, even minor inconsistencies can cause the solution to diverge. Consistent tangents were presented for generalised anisotropic materials and plastically deformable fibres, resulting in quadratic convergence of the simulations for arbitrary deformation gradients and arbitrary degrees of anisotropy. The use of non-linear strain definitions improves the robustness of simulations. Poorly shaped elements behave significantly better when using the right Cauchy-Green strain definition instead of a linear strain definition.

Intra-ply shear locking can be solved by aligning the mesh with the fibre directions, by applying selective reduced integration (SRI) or by using multi-field elements. SRI indicates that only the fibre stress terms of the material model are under-integrated. The new multi-field elements combine the standard displacement degrees of freedom with an additional field that interpolates the fibre strain. The constraint counting method proved to be a useful method to predict the element's accuracy and tendency to lock.

Mesh alignment is impossible in multi-layer elements, leaving SRI and multi-field elements as the only options in simulations of laminated composites. SRI can be easily implemented, but the numerical performance of the multi-layer elements in large deformations is significantly better. The elements based on SRI and multi-field elements underestimate the stiffness, typically from 5% to 15% in this particular study.

Drape experiments of a laminated composite on a dome geometry confirmed the significance of the inter-ply friction during forming. Quasi-isotropic laminates ($[0/45,45/\text{-}45]_s$) showed hardly any inter-ply slip due to high interface traction caused by the rapid forming process. As a consequence, severe wrinkling occurred. A multi-layer element was developed to simulate the forming process. This multi-layer element avoids the use of a computationally expensive contact logic algorithm between the individual layers and is faster than a model in which a number of elements are stacked. The simulation results agree very well with the experimental results for a $[0/90,90/0]_s$ lay-up where wrinkling is absent.

Membrane elements were chosen based on simulation time arguments and their use is justified when stretching of the laminate is the dominant deformation mechanism. Membranes can therefore not predict realistic wrinkling shapes. Shell or solid elements can, but will increase the simulation time significantly. In studies on the feasibility of a design, predicting the occurrence of defects is more important than the exact shape of the defect. Forming Limit Diagrams (FLD) can therefore offer a solution. They allow for fast simulations with coarse meshes using membrane elements and hence for optimisation of the design. A procedure on how to construct such an FLD for a fibre reinforced material is not readily available and requires further research.

# Appendices

These appendices present a detailed look into the most important material models and boundary conditions that were used in the finite element simulations within this research. Specifically, the derivation of consistent tangent matrices is addressed, since these significantly improve convergence speed and hence simulation times of implicit finite element simulations. For highly anisotropic materials, consistent tangents are essential for convergence.

Appendix A summarises the basic continuum mechanics equations that were frequently used in this thesis. Appendix B presents the equation for the finite element nodal forces and the basic equation for the consistent tangent. Both topics, continuum mechanics and the finite element formulation, are widely covered in literature. Therefore, the equations in these appendices are just listed without explanation.

The uni-axial fibre model is presented in the appendices C and D. Appendix C concerns elastic deformations only and in appendix D, plastic deformations are included as well. A generalised anisotropic model for elastic deformations is given in appendix E. The mathematical elaboration of the Mooney-Rivlin material model is given in appendix F. The Mooney-Rivlin model is widely used for simulations with (nearly) incompressible rubber-like solids. The appendices present consistent tangents in finite element formulations. Examples that prove the consistency of the tangents are given.

The consistent linearisation of boundary conditions can decrease simulation times significantly, especially when large deformations are involved. This is done for a uniform surface pressure on planar three node elements in appendix G.

The final appendix, appendix H, summarises the algebraic tensor operations that were frequently used in these appendices.

# Appendix A

# Continuum mechanics

This appendix contains a number of continuum mechanics equations that are frequently used in this thesis. The equations are based on the work of Truesdell and Noll [1], of which a more recent version can be found in the work of Bowen and Wang [2] or Besseling and van der Giessen [3].

Upon deformation, an arbitrary initial material vector $\mathbf{x}_0$ transforms into $\mathbf{x}$. The relation between these two vectors is given by the second order deformation tensor $\mathbf{F}$, which is found by taking the post-gradient of the transformed vector with respect to the initial coordinates:

$$\mathbf{F} = \mathbf{x}\overleftarrow{\nabla}_0 \tag{A.1}$$

The time derivative of $\mathbf{F}$ is given by:

$$\dot{\mathbf{F}} = \mathbf{L} \cdot \mathbf{F}, \tag{A.2}$$

with $\mathbf{L}$ the velocity gradient:

$$\mathbf{L} = \mathbf{v}\overleftarrow{\nabla} \tag{A.3}$$

and $\mathbf{v}$ the velocity. The velocity gradient can be split into a symmetric rate of deformation tensor $\mathbf{D}$ and a skew-symmetric spin tensor $\mathbf{W}$:

$$\mathbf{L} = \mathbf{D} + \mathbf{W}, \tag{A.4}$$

with

$$\mathbf{D} = \tfrac{1}{2}(\mathbf{v}\overleftarrow{\nabla} + \overrightarrow{\nabla}\mathbf{v}) \tag{A.5}$$

and

$$\mathbf{W} = \tfrac{1}{2}(\mathbf{v}\overleftarrow{\nabla} - \overrightarrow{\nabla}\mathbf{v}). \tag{A.6}$$

An initial vector $\mathbf{a}_0$ is transformed by the deformation gradient $\mathbf{F}$ to the current state $\mathbf{a}$ with length $\ell$. Based on that relation, the rate of change of the length $\ell$ can be expressed using the rate of deformation tensor $\mathbf{D}$,

$$\frac{\dot{\ell}}{\ell} = \frac{1}{\ell^2}\mathbf{a}\cdot\mathbf{D}\cdot\mathbf{a}. \tag{A.7}$$

The determinant of $\mathbf{F}$ is also known as the Jacobian $J$ or the volume ratio,

$$\begin{aligned} J &= \det(\mathbf{F}) \\ &= \frac{V}{V_0}, \end{aligned} \tag{A.8}$$

with $V$ the specific volume. The conservation of mass can be expressed as:

$$\rho J = c, \tag{A.9}$$

in which $\rho$ denotes the density. Hence, the relation between the rates of $\rho$ and $J$ is given by:

$$\frac{\dot{\rho}}{\rho} = -\frac{\dot{J}}{J}\,. \tag{A.10}$$

Based on geometrical considerations, the volume ratio can be expressed using the rate of deformation tensor $\mathbf{D}$ as well:

$$\frac{\dot{J}}{J} = \operatorname{trace}(\mathbf{D}). \tag{A.11}$$

Two Cauchy-Green strain tensors are frequently used as a strain measure, e.g. the left Cauchy-Green strain tensor:

$$\mathbf{B} = \mathbf{F}\cdot\mathbf{F}^T \tag{A.12}$$

and the right Cauchy-Green strain tensor:

$$\mathbf{C} = \mathbf{F}^T\cdot\mathbf{F}. \tag{A.13}$$

Hence, the rate of the left Cauchy-Green strain tensor $\mathbf{B}$ can be expressed as:

$$\dot{\mathbf{B}} = \mathbf{L}\cdot\mathbf{B} + \mathbf{B}\cdot\mathbf{L}^T \tag{A.14}$$

and the rate of inverse of $\mathbf{B}$ as:

$$\dot{\mathbf{B}}^{-1} = -\mathbf{B}^{-1}\cdot\mathbf{L} - \mathbf{L}^T\cdot\mathbf{B}^{-1}. \tag{A.15}$$

The rate of the right Cauchy-Green strain tensor $\mathbf{C}$ is given by

$$\dot{\mathbf{C}} = 2\mathbf{F}^T\cdot\mathbf{D}\cdot\mathbf{F}. \tag{A.16}$$

# Bibliography

[1] C. Truesdell and W. Noll. *The Non-Linear Field Theories of Mechanics*, volume III/3 of *The Encyclopedia of Physics*. Springer, New York, 1965.

[2] R. M. Bowen and C. C. Wang. *Introduction to Continuum Mechanics for Engineers*. Plenum Press, New York, 1989. URL www1.mengr.tamu.edu/rbowen/.

[3] J. F. Besseling and E. van der Giessen. *Mathematical Modelling of Inelastic Deformation*. Chapman & Hall, 1994. ISBN: 0-412-45280-4.

# Appendix B

# Finite element formulation

The finite element method is widely documented in literature. A few well-known authors are Zienkiewicz, Taylor, Belytschko, Hughes and Cook [1–4]. Therefore, this appendix presents only the final equations for the finite element nodal forces and the basic equation for the consistent tangent, as derived by Huétink [5].

## B.1 Nodal forces

The starting point for the evaluation of the nodal forces is the equilibrium equation. After weighing, integration by parts and applying Gauss' theorem, equilibrium of the finite element system is given by:

$$\int_V \mathbf{w}\overleftarrow{\nabla} : \boldsymbol{\sigma}\, dV = \int_\Gamma \mathbf{w}\cdot\mathbf{t}\, d\Gamma, \tag{B.1}$$

where $\sigma$ is the Cauchy stress, $\mathbf{w}$ are the element weight functions and $\mathbf{t}$ is the traction on the boundary surface. The volume is denoted by $V$ and the boundary surface by $\Gamma$.

## B.2 Consistent tangent

The rate form of equation (B.1) in the current configuration is given by

$$\int_V \left(\mathbf{w}\overleftarrow{\nabla} : \dot{\boldsymbol{\sigma}} - \mathbf{w}\overleftarrow{\nabla}\cdot\mathbf{v}\overleftarrow{\nabla} : \boldsymbol{\sigma} + \mathbf{w}\overleftarrow{\nabla} : \boldsymbol{\sigma}\tfrac{\dot{J}}{J}\right) dV = \int_\Gamma \mathbf{w}\cdot\dot{\mathbf{t}} + \mathbf{w}\cdot\mathbf{t}(\mathbf{v}\cdot\overleftarrow{\nabla})_\Gamma\, d\Gamma, \tag{B.2}$$

where $\mathbf{v}$ denotes the velocity, $J$ the Jacobian or the volume ratio and $(\mathbf{v} \cdot \overleftarrow{\nabla})_\Gamma$ the rate of change of unit surface area. The left hand side of equation (B.2) represents the consistent linearisation of the internal forces with respect to time:

$$K = \int_V \left( \mathbf{w}\overleftarrow{\nabla} : \dot{\boldsymbol{\sigma}} - \mathbf{w}\overleftarrow{\nabla} \cdot \mathbf{v}\overleftarrow{\nabla} : \boldsymbol{\sigma} + \mathbf{w}\overleftarrow{\nabla} : \boldsymbol{\sigma} \overset{j}{J} \right) dV. \tag{B.3}$$

## Bibliography

[1] O. C. Zienkiewicz and R. L. Taylor. *The Finite Element Method for Solid and Structural Mechanics, Sixth Edition.* Butterworth-Heinemann, 2002. ISBN 978-0750663212.

[2] T. Belytschko, W. K. Liu and B. Moran. *Nonlinear Finite Elements for Continua and Structures.* John Wiley & Sons Ltd, West Sussex, England, 2000. ISBN 0-471-98774-3.

[3] T. J. R. Hughes. *The Finite Element Method: linear static and dynamic finite element analysis.* Dover publications, Mineola, New York, 2000. ISBN 0-486-41181-8.

[4] R. D. Cook. *Finite Element Modeling for Stress Analysis.* J. Wiley and Sons, New York, 1995. ISBN 0-471-10774-3.

[5] J. Huétink. *On the simulation of thermo-mechanical forming processes.* Ph.D. thesis, University of Twente, the Netherlands, 1986. URL www.dieka.org.

# Appendix C

# Uni-axial fibre model

A method to implement non-linear elastic deformations of uni-axial fibres in finite element simulations is developed in this section. The Cauchy stress is given and the consistent tangent matrix is derived. The consistency of the tangent is demonstrated in a one element example. A second example illustrates that the consistent tangent matrix becomes non-symmetric if density changes of the material are ignored in plane strain conditions.

## C.1 Cauchy stress

The deformation gradient $\mathbf{F}$ is decomposed into a stretch tensor $\mathbf{G}$ and a subsequent rotation $\mathbf{R}$:

$$\mathbf{F} = \mathbf{R} \cdot \mathbf{G}. \tag{C.1}$$

This decomposition is illustrated in figure C.1.

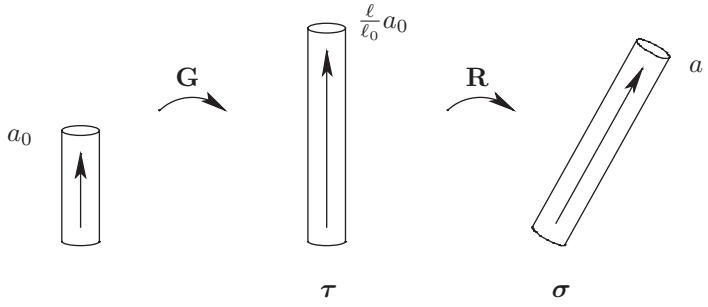


*Figure C.1: Decomposition of the fibre deformation in a stretch part and a subsequent rotation.*

In this figure, $\boldsymbol{\sigma}$ denotes the Cauchy stress tensor and $\boldsymbol{\tau}$ the local, invariant stress tensor. This local stress tensor $\boldsymbol{\tau}$ is given by

$$\boldsymbol{\tau} = \frac{\rho E \ell^2}{2\rho_0 \ell_0^6} \mathbf{a}_0\mathbf{a}_0\mathbf{a}_0\mathbf{a}_0 : (\mathbf{C} - \mathbf{I}), \tag{C.2}$$

in which $\rho$ denotes the density, $E$ the Young's modulus of the fibre, $\ell$ the length of the fibre and $\mathbf{C}$ the right Cauchy-Green tensor. The Cauchy stress is found by rotating the local stress tensor

$$\boldsymbol{\sigma} = \mathbf{R} \cdot \boldsymbol{\tau} \cdot \mathbf{R}^T. \tag{C.3}$$

The Cauchy stress is used in the evaluation of the nodal forces, given by equation (B.1).

## C.2 Consistent tangent

The starting point is the tangent of the finite element nodal forces, given by equation (B.3). This equation contains the rate of the Cauchy stress $\dot{\boldsymbol{\sigma}}$, which is found by differentiating equation C.3 with respect to time:

$$\dot{\boldsymbol{\sigma}} = \dot{\mathbf{R}} \cdot \boldsymbol{\tau} \cdot \mathbf{R}^T + \mathbf{R} \cdot \dot{\boldsymbol{\tau}} \cdot \mathbf{R}^T + \mathbf{R} \cdot \boldsymbol{\tau} \cdot \dot{\mathbf{R}}^T \tag{C.4}$$

The integrant of the tangent matrix (B.3) can now be rewritten as

$$\begin{aligned} \overleftarrow{\mathbf{w}\nabla} : \dot{\boldsymbol{\sigma}} - \overleftarrow{\mathbf{w}\nabla} \cdot \overleftarrow{\mathbf{v}\nabla} : \boldsymbol{\sigma} + \overleftarrow{\mathbf{w}\nabla} : \boldsymbol{\sigma} \overset{j}{J} = \underbrace{\overleftarrow{\mathbf{w}\nabla} : \dot{\mathbf{R}} \cdot \boldsymbol{\tau} \cdot \mathbf{R}^T}_{a} + \\ \underbrace{\overleftarrow{\mathbf{w}\nabla} : \mathbf{R} \cdot \boldsymbol{\tau} \cdot \dot{\mathbf{R}}^T}_{b} + \underbrace{\overleftarrow{\mathbf{w}\nabla} : \mathbf{R} \cdot \dot{\boldsymbol{\tau}} \cdot \mathbf{R}^T}_{c} - \underbrace{\overleftarrow{\mathbf{w}\nabla} \cdot \overleftarrow{\mathbf{v}\nabla} : \boldsymbol{\sigma}}_{d} + \underbrace{\overleftarrow{\mathbf{w}\nabla} : \boldsymbol{\sigma} \overset{j}{J}}_{e}. \end{aligned} \tag{C.5}$$

Evaluation of the parts $a$ and $b$ requires the rate of rotation tensor $\dot{\mathbf{R}}$. Differentiating both sides of equation (C.1) with respect to time and re-arranging results in

$$\dot{\mathbf{R}} = \dot{\mathbf{F}} \cdot \mathbf{G}^{-1} - \mathbf{R} \cdot \dot{\mathbf{G}} \cdot \mathbf{G}^{-1}. \tag{C.6}$$

The time derivative of $\mathbf{F}$ is given by

$$\dot{\mathbf{F}} = \mathbf{L} \cdot \mathbf{F}, \tag{C.7}$$

with $\mathbf{L}$ the velocity gradient:

$$\mathbf{L} = \mathbf{v}\overleftarrow{\nabla} \tag{C.8}$$

The stretch tensor $\mathbf{G}$ relates the current length of the fibre to the initial length:

$$\mathbf{G} \cdot \mathbf{a}_0 = \tfrac{\ell}{\ell_0}\mathbf{a}_0. \tag{C.9}$$

The inverse, $\mathbf{G}^{-1}$ and the time derivative $\dot{\mathbf{G}}$ hence satisfy, respectively,

$$\mathbf{G}^{-1} \cdot \mathbf{a}_0 = \tfrac{\ell_0}{\ell}\mathbf{a}_0 \tag{C.10}$$

and

$$\dot{\mathbf{G}} \cdot \mathbf{a}_0 = \tfrac{\dot{\ell}}{\ell_0}\mathbf{a}_0. \tag{C.11}$$

The rate of rotation tensor $\dot{\mathbf{R}}$ can now be written as:

$$\begin{aligned} \dot{\mathbf{R}} &= \mathbf{L} \cdot \mathbf{R} - \mathbf{R} \cdot \dot{\mathbf{G}} \cdot \mathbf{G}^{-1} \\ &= \mathbf{L} \cdot \mathbf{R} - \tfrac{\dot{\ell}}{\ell}\mathbf{R}. \end{aligned} \tag{C.12}$$

Evaluation of the parts $a$ and $b$ of equation (C.5) results in:

$$\begin{aligned} a + b &= \mathbf{w}\overleftarrow{\nabla} : (\dot{\mathbf{R}} \cdot \boldsymbol{\tau} \cdot \mathbf{R}^T + \mathbf{R} \cdot \boldsymbol{\tau} \cdot \dot{\mathbf{R}}^T) \\ &= \mathbf{w}\overleftarrow{\nabla} : (\mathbf{L} \cdot \mathbf{R} \cdot \boldsymbol{\tau} \cdot \mathbf{R}^T + \mathbf{R} \cdot \boldsymbol{\tau} \cdot \mathbf{R}^T \cdot \mathbf{L}^T - 2\tfrac{\dot{\ell}}{\ell}\mathbf{R} \cdot \boldsymbol{\tau} \cdot \mathbf{R}^T) \\ &= \underbrace{\mathbf{w}\overleftarrow{\nabla} : \mathbf{v}\overleftarrow{\nabla} \cdot \boldsymbol{\sigma}}_{a_1} + \underbrace{\mathbf{w}\overleftarrow{\nabla} : \boldsymbol{\sigma} \cdot \overrightarrow{\nabla}\mathbf{v}}_{a_2} - \underbrace{\mathbf{w}\overleftarrow{\nabla} : 2\tfrac{\dot{\ell}}{\ell} \cdot \boldsymbol{\sigma}}_{a_3}. \end{aligned} \tag{C.13}$$

The parts $a_1$, $a_2$ and $d$ can be combined by making use of the operations given by the equations (H.1) and (H.2):

$$\begin{aligned} a_1 + a_2 + d &= \mathbf{w}\overleftarrow{\nabla} : \mathbf{v}\overleftarrow{\nabla} \cdot \boldsymbol{\sigma} + \mathbf{w}\overleftarrow{\nabla} : \boldsymbol{\sigma} \cdot \overrightarrow{\nabla}\mathbf{v} - \mathbf{w}\overleftarrow{\nabla} \cdot \mathbf{v}\overleftarrow{\nabla} : \boldsymbol{\sigma} \\ &= (\overrightarrow{\nabla}\mathbf{w} \cdot \mathbf{v}\overleftarrow{\nabla} + \overrightarrow{\nabla}\mathbf{w} \cdot \overrightarrow{\nabla}\mathbf{v} - \mathbf{w}\overleftarrow{\nabla} \cdot \mathbf{v}\overleftarrow{\nabla}) : \boldsymbol{\sigma} \\ &= \underbrace{\overrightarrow{\nabla}\mathbf{w} \cdot \mathbf{v}\overleftarrow{\nabla} : \boldsymbol{\sigma}}_{d1}. \end{aligned} \tag{C.14}$$

Differentiating the local stress $\boldsymbol{\tau}$ of equation (C.2)with respect to time results in

$$\dot{\boldsymbol{\tau}} = {}^4\mathbf{H} : \dot{\mathbf{C}} + \boldsymbol{\tau}(2\frac{\dot{\ell}}{\ell} + \frac{\dot{\rho}}{\rho}), \tag{C.15}$$

with

$${}^4\mathbf{H} = \frac{\rho E \ell^2}{2\rho_0 \ell_0^6}\, \mathbf{a}_0\mathbf{a}_0\mathbf{a}_0\mathbf{a}_0. \tag{C.16}$$

Evaluation of part $c$ of equation (C.5) now gives

$$\begin{aligned} c &= \mathbf{w}\overleftarrow{\nabla} : \left\{\mathbf{R}\cdot\left({}^4\mathbf{H} : \dot{\mathbf{C}} + \boldsymbol{\tau}(2\frac{\dot{\ell}}{\ell} + \frac{\dot{\rho}}{\rho})\right)\cdot\mathbf{R}^T\right\} \\ &= \underbrace{\mathbf{w}\overleftarrow{\nabla} : (\mathbf{R}\cdot{}^4\mathbf{H} : \dot{\mathbf{C}}\cdot\mathbf{R}^T)}_{c_1} + \underbrace{\mathbf{w}\overleftarrow{\nabla} : 2\frac{\dot{\ell}}{\ell}\boldsymbol{\sigma}}_{c_2} + \underbrace{\mathbf{w}\overleftarrow{\nabla} : \frac{\dot{\rho}}{\rho}\cdot\boldsymbol{\sigma}}_{c_3}. \end{aligned} \tag{C.17}$$

The combination of $a_3$, $c_2$, $c_3$ and $e$ is equal to zero (A.10):

$$\begin{aligned} a_3 + c_2 + c_3 + e &= \mathbf{w}\overleftarrow{\nabla} : (-2\frac{\dot{\ell}}{\ell}\boldsymbol{\sigma} + 2\frac{\dot{\ell}}{\ell}\boldsymbol{\sigma} + \frac{\dot{\rho}}{\rho}\boldsymbol{\sigma} + \frac{\dot{j}}{j}\boldsymbol{\sigma}) \\ &= 0. \end{aligned} \tag{C.18}$$

Using the equations (A.16), (H.4), (H.5) and (H.2), $c_1$ can be expressed as

$$\begin{aligned} c_1 &= \mathbf{w}\overleftarrow{\nabla} : (\mathbf{R}\cdot{}^4\mathbf{H} : \dot{\mathbf{C}}\cdot\mathbf{R}^T) \\ &= \frac{\rho E\ell^2}{2\rho_0\ell_0^6}\,\mathbf{w}\overleftarrow{\nabla} : (\mathbf{R}\cdot\mathbf{a}_0\mathbf{a}_0\cdot\dot{\mathbf{C}}\cdot\mathbf{a}_0\mathbf{a}_0\cdot\mathbf{R}^T) \\ &= \frac{\rho E\ell^2}{\rho_0\ell_0^6}\,\mathbf{w}\overleftarrow{\nabla} : (\mathbf{R}\cdot\mathbf{a}_0\mathbf{a}_0\cdot\mathbf{F}^T\cdot\mathbf{D}\cdot\mathbf{F}\cdot\mathbf{a}_0\mathbf{a}_0\cdot\mathbf{R}^T) \\ &= \frac{\rho E\ell^2}{\rho_0\ell_0^6}\,\mathbf{w}\overleftarrow{\nabla} : (\frac{\ell_0}{\ell}\cdot\mathbf{a}\mathbf{a}\cdot\mathbf{D}\cdot\mathbf{a}\mathbf{a}\frac{\ell_0}{\ell}) \\ &= \frac{\rho E}{\rho_0\ell_0^4}\,(\mathbf{w}\overleftarrow{\nabla}\cdot\mathbf{a}\mathbf{a}) : (\mathbf{a}\mathbf{a}\cdot\mathbf{D}) \\ &= \frac{\rho E}{\rho_0\ell_0^4}\left(\tfrac{1}{2}(\mathbf{w}\overleftarrow{\nabla} + \overrightarrow{\nabla}\mathbf{w})\cdot\mathbf{a}\mathbf{a}\right) : \left(\mathbf{a}\mathbf{a}\cdot\tfrac{1}{2}(\mathbf{v}\overleftarrow{\nabla} + \overrightarrow{\nabla}\mathbf{v})\right). \end{aligned} \tag{C.19}$$

Finally, the tangent matrix of the uni-axial fibre model consists of the parts $c_1$ and $d_1$ found in the equation (C.19) and (C.14)

$$\begin{aligned} K = \int_V \Bigg[\frac{\rho E}{\rho_0\ell_0^4}\left(\tfrac{1}{2}(\mathbf{w}\overleftarrow{\nabla} + \overrightarrow{\nabla}\mathbf{w})\cdot\mathbf{a}\mathbf{a}\right) : \left(\mathbf{a}\mathbf{a}\cdot\tfrac{1}{2}(\mathbf{v}\overleftarrow{\nabla} + \overrightarrow{\nabla}\mathbf{v})\right) + \\ \overrightarrow{\nabla}\mathbf{w}\cdot\mathbf{v}\overleftarrow{\nabla} : \boldsymbol{\sigma}\Bigg]\, dV. \end{aligned} \tag{C.20}$$

## C.3 Application

The uni-axial fibre model has been implemented in MATLAB©. Figure C.2 shows the initial and final, deformed shape of a one element simulation. The initial width and height of the element is 1 mm. The fibres are oriented at 0°, 45° and -45° with respect to the $x$-axis. The Young's modulus of the fibres

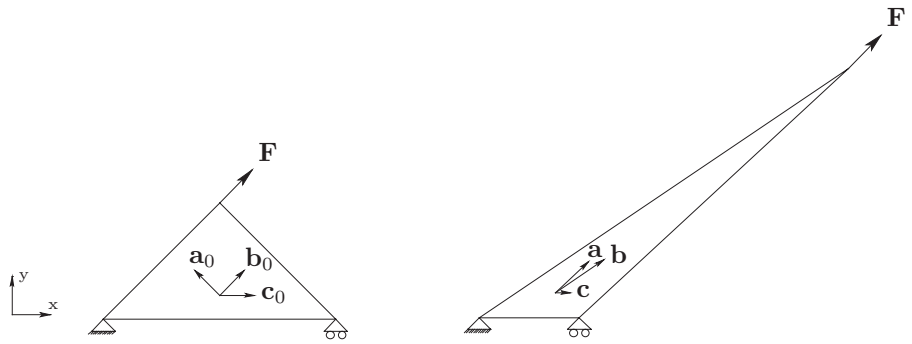


*Figure C.2: Initial and final configurations of an element with three fibre families.*

was set to 1 MPa and the applied force was $\frac{1}{2}\sqrt{2}$ N. The triangle has a linear displacement field and an initial thickness of 1 mm. The volume of the element is constant during the simulation and plane stress conditions are assumed.

A Newton-Raphson procedure was used to find the solution of this non-linear problem. The error norm $\epsilon$ after each iteration $i$ can be expressed as a function of the previous error norm:

$$\epsilon_i = \alpha \epsilon_{i-1}^n. \tag{C.21}$$

The convergence rate depends on the convergence factor $\alpha$ and the convergence power $n$. A convergence power value of $n = 1$ indicates linear convergence and the error norm will decrease by the factor $\alpha$ each iteration. A value of $n > 1$ indicates superlinear convergence. The error norm will be powered to the value of $n$ in each subsequent iteration, resulting in an exponential sequence and high convergence speeds. The Newton-Raphson scheme shows quadratic convergence with $n = 2$, provided the objective function is linearised consistently and the initial value is sufficiently close to the objective value.

Figure C.3 shows the error norms during the iterative process of this simulation. The unbalance norm $\epsilon_u$ and the displacement norm $\epsilon_d$ are given by:

$$\epsilon_u = \frac{\|R - F\|}{\|R\|} \qquad \epsilon_d = \frac{\|\triangle u\|}{\|u\|}, \tag{C.22}$$

where $R$ are the reaction forces, $F$ the applied nodal loads, $\triangle u$ the displacement found during the iteration and $u$ the total displacement. The slope that corresponds to a quadratically converging sequence is indicated

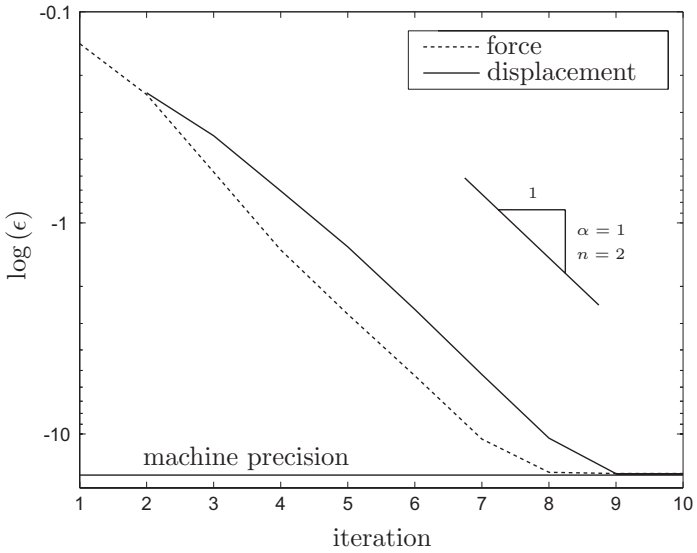


*Figure C.3: Convergence plot of the one element test. The slope $n = 2$ indicates quadratic convergence.*

as well. Figure C.3 shows that the convergence rate is quadratic from the third/fourth iteration onwards until the solution reaches the machine precision, which was $2.2 \cdot 10^{-16}$ for the double precision real on the PC used.

Table C.1 shows the approximated values of the horizontal displacement of the top node and the convergence power of the displacement norm. The convergence power value $n$ is found by rewriting equation (C.21) and by assuming that $\alpha = 1$:

$$n = \frac{\log \epsilon_i}{\log \epsilon_{i-1}}. \tag{C.23}$$

Initially, the convergence speed is superlinear due to the large displacements and strain increments. It becomes quadratic from the fourth iteration onwards. The number of significant digits doubles each iteration and machine precision is reached within four iterations. The error norm levels once the machine precision has been reached, resulting in a convergence power value of one.

| iteration | $u$ [mm] | $n$ |
|---|---|---|
| 1 | 1.750 000 000 000 001 | - |
| 2 | 1.216 051 380 773 097 | 1.60 |
| 3 | 1.030 015 264 088 182 | 1.83 |
| 4 | 1.058 502 507 917 225 | 1.84 |
| 5 | 1.086 982 862 613 517 | 1.98 |
| 6 | 1.088 624 189 628 079 | 2.03 |
| 7 | 1.088 627 323 631 528 | 2.00 |
| 8 | 1.088 627 323 651 719 | 1.48 |
| 9 | 1.088 627 323 651 718 | 1.00 |

*Table C.1: Horizontal displacement of the top node and the convergence power value. The significant digits are underlined.*

## C.4 Plane strain

The assumption of plane stress conditions in combination with a constant element volume was used in the example in the previous section. In this section, plane strain conditions are assumed. Hence, the volume of the element is not constant and the rate of the volume ratio $J$ is not equal to zero:

$$\frac{\dot{J}}{J} \neq 0. \tag{C.24}$$

The density of the material will change upon forming according to equation (A.10). However, these density changes are often neglected in FE simulations, in both the evaluation of the element stresses as well as in the evaluation of the tangent matrix. This can cause a significant drop in the convergence speed. Neglecting the density change results in

$$\frac{\dot{\rho}}{\rho} = 0 \tag{C.25}$$

and the last two terms in equation (C.18) will not cancel out. This results in a non-symmetric tangent matrix for the plane strain simulation. The consistent tangent matrix consists of the symmetric part given by equation (C.20), from which the neglected density change has to be subtracted. For the upper left

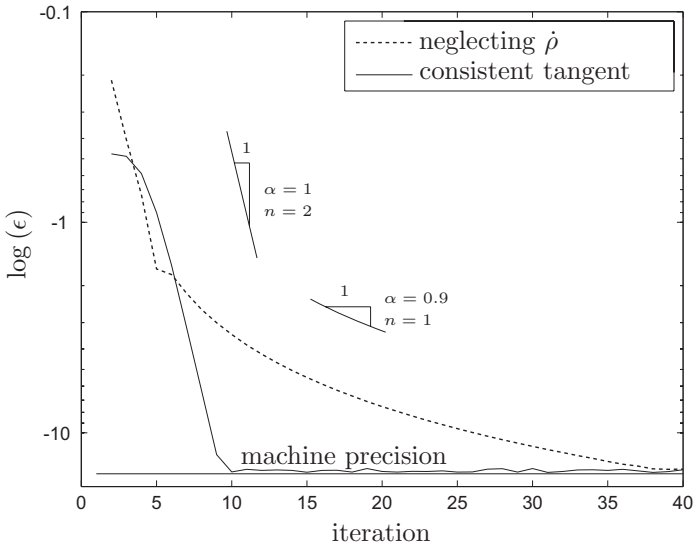


*Figure C.4: Convergence plot of the plane strain element test with and without taking into account density changes.*

part of the tangent matrix in the deformed state, this results in:

$$K_{[1:2,1:2]} = \text{eq. (C.20)} - \int_V \mathbf{w}\overleftarrow{\nabla} : \frac{\dot{\rho}}{\rho}\boldsymbol{\sigma}\, dV \tag{C.26}$$

$$= \text{eq. (C.20)} + \int_V \mathbf{w}\overleftarrow{\nabla} : \boldsymbol{\sigma} \cdot \text{tr}\,(\mathbf{D})\, dV$$

$$\begin{bmatrix} 2.354 & -0.135 \\ 1.743 & 0.221 \end{bmatrix} = \begin{bmatrix} 1.229 & 0.717 \\ 0.717 & 0.998 \end{bmatrix} + \begin{bmatrix} 1.125 & -0.852 \\ 1.026 & -0.777 \end{bmatrix}.$$

The simulation setup from section C.3 was used for two new simulations. Now plane strain conditions were assumed instead of plane stress conditions. The symmetric tangent, given by equation (C.20), was used in first simulation and the consistent, non-symmetric tangent, was used in the second simulation. Figure C.4 shows the convergence speed of both simulations. Neglecting the density change causes the convergence speed to drop from quadratic to linear. The number of iterations necessary to reach machine precision increased from 10 to 40. The results emphasise the importance of consistent tangents. Solving large FE systems of equations is computationally expensive. Consistent tangent matrices reduce the number of times the system of equations has to be solved and hence the simulation times.

# Appendix D

# Uni-axial fibre model including plasticity

A uni-axial fibre model for elastic deformations in finite element simulations was developed in appendix C. In this appendix, plastic deformation is included as well. The Cauchy stress and the consistent tangent matrix are derived for arbitrarily sized plastic deformation increments and arbitrary hardening laws. A one element example is given, in which quadratic convergence was proven for a plastic strain increment around 100%.

## D.1 Cauchy stress

The deformation gradient $\mathbf{F}$ is decomposed into a stretch tensor $\mathbf{G}$ and a subsequent rotation $\mathbf{R}$. The stretch tensor is split into a plastic part $\mathbf{G}_p$ and an elastic part $\mathbf{G}_e$.

$$\mathbf{F} = \mathbf{R} \cdot \mathbf{G}_e \cdot \mathbf{G}_p \tag{D.1}$$

The decomposition is illustrated in figure D.1. Plastic deformation introduces permanent strains. The fibre will not retain the original length $\ell_0$ after unloading, but will retract to the new stress free length $\ell_*$.

The total strain $\varepsilon$, the plastic strain $\varepsilon_p$ and the elastic strain $\varepsilon_p$ are expressed in the fibre lengths and as a function of the total right Cauchy-Green strain

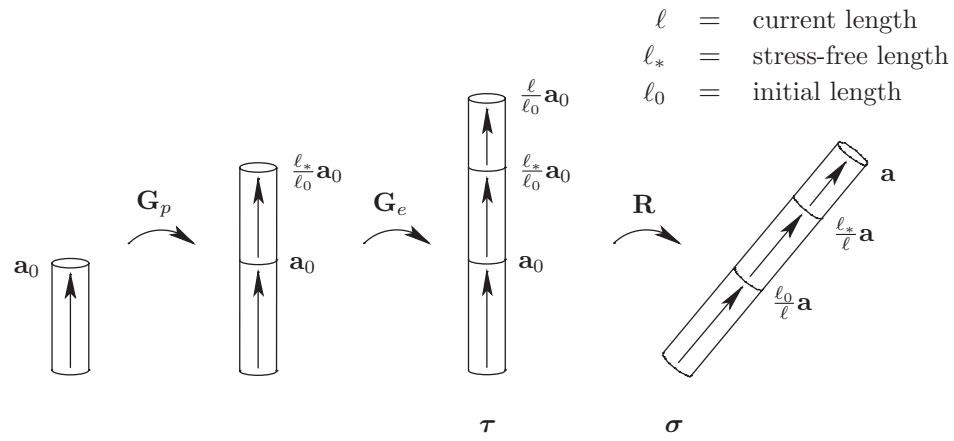


*Figure D.1: Decomposition of the fibre deformation in a stretch part and a subsequent rotation including plasticity.*

tensor $\mathbf{C}$.

$$\varepsilon = \frac{\ell^2 - \ell_0^2}{2\ell_0^2} = \tfrac{1}{2}\mathbf{a}_0\mathbf{a}_0 : (\mathbf{C} - \mathbf{I}) \tag{D.2}$$

$$\varepsilon_p = \frac{\ell_*^2 - \ell_0^2}{2\ell_0^2} = \tfrac{1}{2}\mathbf{a}_0\mathbf{a}_0 : \left(\frac{\ell_*^2}{\ell_0^2}\mathbf{C} - \mathbf{I}\right) \tag{D.3}$$

$$\varepsilon_e = \frac{\ell^2 - \ell_*^2}{2\ell_*^2} = \tfrac{1}{2}\mathbf{a}_0\mathbf{a}_0 : \left(\frac{\ell_0^2}{\ell_*^2}\mathbf{C} - \mathbf{I}\right) \tag{D.4}$$

The total strain is not equal to the sum of the plastic and elastic strain due to the nonlinear strain measure:

$$\varepsilon \neq \varepsilon_e + \varepsilon_p. \tag{D.5}$$

The scalar fibre stress $\tau^\diamond$ is expressed as:

$$\tau^\diamond = \alpha \cdot \varepsilon_e, \tag{D.6}$$

with

$$\alpha = \frac{\rho E \ell^2}{\rho_0 \ell_*^4}. \tag{D.7}$$

The local stress tensor $\boldsymbol{\tau}$ is given by:

$$\begin{aligned} \boldsymbol{\tau} &= \frac{\tau^\diamond}{\ell_0^2}\mathbf{a}_0\mathbf{a}_0 \\ &= \frac{\rho E \ell^2}{2\rho_0 \ell_*^4 \ell_0^2}\mathbf{a}_0\mathbf{a}_0\mathbf{a}_0\mathbf{a}_0 : \left(\frac{\ell_0^2}{\ell_*^2}\mathbf{C} - \mathbf{I}\right) \end{aligned} \tag{D.8}$$

The Cauchy stress is found by rotating the local stress by the rotation tensor $\mathbf{R}$:

$$\boldsymbol{\sigma} = \mathbf{R} \cdot \boldsymbol{\tau} \cdot \mathbf{R}^T. \tag{D.9}$$

The nodal forces are then calculated from equation (B.1).

## D.2 Consistent tangent

The consistent tangent is given by equation (B.3). Identical to the first steps of section C.2, equation (B.3) is rewritten as:

$$\begin{aligned}\overleftarrow{\mathbf{w}\nabla} : \dot{\boldsymbol{\sigma}} - \overleftarrow{\mathbf{w}\nabla} \cdot \overleftarrow{\mathbf{v}\nabla} : \boldsymbol{\sigma} + \overleftarrow{\mathbf{w}\nabla} : \boldsymbol{\sigma}\tfrac{\dot{J}}{J} = \underbrace{\overleftarrow{\mathbf{w}\nabla} : \dot{\mathbf{R}} \cdot \boldsymbol{\tau} \cdot \mathbf{R}^T}_{a} + \\ \underbrace{\overleftarrow{\mathbf{w}\nabla} : \mathbf{R} \cdot \boldsymbol{\tau} \cdot \dot{\mathbf{R}}^T}_{b} + \underbrace{\overleftarrow{\mathbf{w}\nabla} : \mathbf{R} \cdot \dot{\boldsymbol{\tau}} \cdot \mathbf{R}^T}_{c} - \underbrace{\overleftarrow{\mathbf{w}\nabla} \cdot \overleftarrow{\mathbf{v}\nabla} : \boldsymbol{\sigma}}_{d} + \underbrace{\overleftarrow{\mathbf{w}\nabla} : \boldsymbol{\sigma}\tfrac{\dot{J}}{J}}_{e}.\end{aligned} \tag{D.10}$$

The parts $a$, $b$ and $d$ can be combined as shown in section C.2, equation (C.13) and (C.14) to

$$a + b + d = \underbrace{-\overleftarrow{\mathbf{w}\nabla} : 2\tfrac{\dot{\ell}}{\ell} \cdot \boldsymbol{\sigma}}_{a_3} + \underbrace{\overrightarrow{\nabla}\mathbf{w} \cdot \overleftarrow{\mathbf{v}\nabla} : \boldsymbol{\sigma}}_{d_1}. \tag{D.11}$$

The local stress rate $\dot{\boldsymbol{\tau}}$ is found by differentiating equation (D.8) with respect to time:

$$\begin{aligned}\dot{\boldsymbol{\tau}} &= \frac{\dot{\tau}^{\diamond}}{\ell_0^2}\mathbf{a}_0\mathbf{a}_0 \\ &= \frac{1}{\ell_0^2}\mathbf{a}_0\mathbf{a}_0(\dot{\alpha} \cdot \varepsilon_e + \alpha \cdot \dot{\varepsilon}_e) \\ &= \boldsymbol{\tau}\Big(\frac{\dot{\rho}}{\rho} + \frac{2\dot{\ell}}{\ell} - \frac{6\dot{\ell}_*}{\ell_*}\Big) - \frac{\dot{\ell}_*}{\ell_*}\frac{\rho E \ell^2}{\rho_0 \ell_*^4}\mathbf{a}_0\mathbf{a}_0 + \frac{\rho E \ell^2}{2\ell_*^6}\mathbf{a}_0\mathbf{a}_0\mathbf{a}_0\mathbf{a}_0 : \dot{\mathbf{C}},\end{aligned} \tag{D.12}$$

with $\dot{\alpha}$ as

$$\dot{\alpha} = \alpha\Big(\frac{\dot{\rho}}{\rho} + \frac{2\dot{\ell}}{\ell} - \frac{4\dot{\ell}_*}{\ell_*}\Big) \tag{D.13}$$

and $\dot{\varepsilon}_e$ as

$$\begin{aligned}\dot{\varepsilon}_e &= \tfrac{1}{2}\mathbf{a}_0\mathbf{a}_0 : \Big(\frac{-2\ell_0^2\ell_*}{\ell_*^3}\mathbf{C} + \frac{\ell_0^2}{\ell_*^2}\dot{\mathbf{C}}\Big) \\ &= \frac{\ell_0^2}{2\ell_*^2}\mathbf{a}_0\mathbf{a}_0 : \dot{\mathbf{C}} - \frac{\dot{\ell}_*}{\ell_*}(2\varepsilon_e + \ell_0^2).\end{aligned} \tag{D.14}$$

The evaluation of part $c$ now reads:

$$\begin{aligned} c &= \mathbf{w}\overleftarrow{\nabla} : \mathbf{R}\cdot\dot{\boldsymbol{\tau}}\cdot\mathbf{R} \\ &= \underbrace{\mathbf{w}\overleftarrow{\nabla} : \boldsymbol{\sigma}\Big(\frac{\dot\rho}{\rho}+\frac{2\dot\ell}{\ell}\Big)}_{c_1} - \underbrace{\mathbf{w}\overleftarrow{\nabla} : \frac{6\dot\ell_*}{\ell_*}\boldsymbol{\sigma}}_{c_2} - \underbrace{\mathbf{w}\overleftarrow{\nabla} : \frac{\dot\ell_*}{\ell_*}\frac{\rho E\ell_0^2}{\rho_0\ell_*^4}\mathbf{aa}}_{c3} + \\ &\qquad \underbrace{\mathbf{w}\overleftarrow{\nabla} : \frac{\rho E\ell_0^2}{2\ell_*^6}\mathbf{aaa}_0\mathbf{a}_0 : \dot{\mathbf{C}}}_{c_4}. \end{aligned} \tag{D.15}$$

By using the equality (A.10), it is shown that the combination of the parts $a_3$, $c_1$ and $e$ equals zero:

$$\begin{aligned} a_3 + c_1 + e &= \mathbf{w}\overleftarrow{\nabla} : \boldsymbol{\sigma}\Big(-\frac{2\dot\ell}{\ell}+\frac{\dot\rho}{\rho}+\frac{2\dot\ell}{\ell}+\frac{\dot J}{J}\Big) \\ &= 0. \end{aligned} \tag{D.16}$$

Using equation (A.7), the normalised rate of $\ell_*$ is expressed as:

$$\begin{aligned} \frac{\dot\ell_*}{\ell_*} &= \frac{1}{\ell_*}\cdot\frac{\partial\ell_*}{\partial\ell}\cdot\frac{\partial\ell}{\partial t} \\ &= \frac{1}{\ell\ell_*}\cdot\frac{\partial\ell_*}{\partial\ell}\cdot\mathbf{a}\cdot\mathbf{D}\cdot\mathbf{a}. \end{aligned} \tag{D.17}$$

With equation (D.17) and (D.8) and the tensor operation given by (H.4), (H.5) and (H.2), the parts $c_2$, $c_3$ and $c_4$ are now written, respectively,

$$\begin{aligned} c_2 &= -\mathbf{w}\overleftarrow{\nabla} : \frac{6\dot\ell_*}{\ell_*}\boldsymbol{\sigma} \\ &= -\frac{\rho E\ell_0^2}{\rho_0\ell_*^6}\frac{\ell_*}{\ell}\frac{\partial\ell_*}{\partial\ell}\frac{6\varepsilon_e}{\ell_0^2}\Big(\tfrac{1}{2}(\mathbf{w}\overleftarrow{\nabla}+\overrightarrow{\nabla}\mathbf{w})\cdot\mathbf{aa}\Big) : \Big(\mathbf{aa}\cdot\tfrac{1}{2}(\mathbf{v}\overleftarrow{\nabla}+\overrightarrow{\nabla}\mathbf{v})\Big), \end{aligned} \tag{D.18}$$

$$\begin{aligned} c_3 &= -\mathbf{w}\overleftarrow{\nabla} : \frac{\dot\ell_*}{\ell_*}\frac{\rho E\ell_0^2}{\rho_0\ell_*^4}\mathbf{aa} \\ &= -\frac{\rho E\ell_0^2}{\rho_0\ell_*^6}\frac{\ell_*}{\ell}\frac{\partial\ell_*}{\partial\ell}\Big(\tfrac{1}{2}(\mathbf{w}\overleftarrow{\nabla}+\overrightarrow{\nabla}\mathbf{w})\cdot\mathbf{aa}\Big) : \Big(\mathbf{aa}\cdot\tfrac{1}{2}(\mathbf{v}\overleftarrow{\nabla}+\overrightarrow{\nabla}\mathbf{v})\Big), \end{aligned} \tag{D.19}$$

$$\begin{aligned} c_4 &= \mathbf{w}\overleftarrow{\nabla} : \frac{\rho E\ell_0^2}{2\ell_*^6}\mathbf{aaa}_0\mathbf{a}_0 : \dot{\mathbf{C}} \\ &= \frac{\rho E\ell_0^2}{\rho_0\ell_*^6}\Big(\tfrac{1}{2}(\mathbf{w}\overleftarrow{\nabla}+\overrightarrow{\nabla}\mathbf{w})\cdot\mathbf{aa}\Big) : \Big(\mathbf{aa}\cdot\tfrac{1}{2}(\mathbf{v}\overleftarrow{\nabla}+\overrightarrow{\nabla}\mathbf{v})\Big). \end{aligned} \tag{D.20}$$

The expression for $\frac{\partial \ell_*}{\partial \ell}$ is found by starting with:

$$\frac{\partial \sigma_y}{\partial \ell} = \frac{\partial \sigma_y}{\partial \ell_*} \cdot \frac{\partial \ell_*}{\partial \ell}, \tag{D.21}$$

which can be rewritten as

$$\begin{aligned} \frac{\partial \ell_*}{\partial \ell} &= \frac{\partial \sigma_y}{\partial \ell} \cdot \left(\frac{\partial \sigma_y}{\partial \ell_*}\right)^{-1} \\ &= \frac{\partial \sigma_y}{\partial \ell} \cdot \left(\frac{\partial \sigma_y}{\partial \varepsilon_p} \cdot \frac{\partial \varepsilon_p}{\partial \ell_*}\right)^{-1}, \end{aligned} \tag{D.22}$$

with the derivative of the plastic strain with respect to $\ell_*$ as

$$\frac{\partial \varepsilon_p}{\partial \ell_*} = \frac{\ell_*}{\ell_0^2}. \tag{D.23}$$

The one-dimensional fibre stress $\tau^\diamond$ is equal to the yield stress $\sigma_y$ during plastic deformation. Their derivatives with respect to the driven length $\ell$ are equal as well:

$$\begin{aligned} \frac{\partial \sigma_y}{\partial \ell} &= \frac{\partial \tau^\diamond}{\partial \ell} \\ &= \frac{\partial \alpha}{\partial \ell} \cdot \varepsilon_e + \alpha \frac{\partial \varepsilon_e}{\partial \ell} \\ &= \left(\frac{2\alpha}{\ell} - \frac{4\alpha}{\ell_*} \cdot \frac{\partial \ell_*}{\partial \ell}\right) \cdot \varepsilon_e + \alpha \left(\frac{\ell}{\ell_*^2} - \frac{\ell^2}{\ell_*^3} \cdot \frac{\partial \ell_*}{\partial \ell}\right) \\ &= \frac{2\tau^\diamond}{\ell} + \frac{\alpha \ell}{\ell_*^2} - \left(\frac{4\tau^\diamond}{\ell_*} + \frac{\alpha \ell^2}{\ell_*^3}\right) \cdot \frac{\partial \ell_*}{\partial \ell}. \end{aligned} \tag{D.24}$$

Combining equation (D.22), (D.23), (D.24) results in

$$\frac{\partial \ell_*}{\partial \ell} = \frac{\dfrac{2\tau^\diamond}{\ell} + \dfrac{\alpha \ell}{\ell_*^2}}{\dfrac{\partial \sigma_y}{\partial \varepsilon_p} + \dfrac{4\tau^\diamond}{\ell_*} + \dfrac{\alpha \ell^2}{\ell_*^3}}, \tag{D.25}$$

in which $\frac{\partial \sigma_y}{\partial \varepsilon_p}$ is the input provided by the constitutive equations. Finally, the consistent tangent is combined from the parts $c_2$, $c_3$, $c_4$ and $d_1$:

$$\begin{aligned} K = \int_V \Bigg[ &\frac{\rho E \ell_0^2}{\rho_0 \ell_*^6} \left(1 - \frac{\ell_*}{\ell} \frac{\partial \ell_*}{\partial \ell} \left(1 + 6 \frac{\varepsilon_e}{\ell_0^2}\right)\right) \cdot \\ &\left(\tfrac{1}{2}(\mathbf{w}\overleftarrow{\nabla} + \overrightarrow{\nabla}\mathbf{w}) \cdot \mathbf{a}\mathbf{a}\right) : \left(\mathbf{a}\mathbf{a} \cdot \tfrac{1}{2}(\mathbf{v}\overleftarrow{\nabla} + \overrightarrow{\nabla}\mathbf{v})\right) + \overrightarrow{\nabla}\mathbf{w} \cdot \mathbf{v}\overleftarrow{\nabla} : \boldsymbol{\sigma} \Bigg] \, dV, \end{aligned} \tag{D.26}$$

using equation (D.25) for $\frac{\partial \ell_*}{\partial \ell}$. This tangent is valid for arbitrary hardening laws.

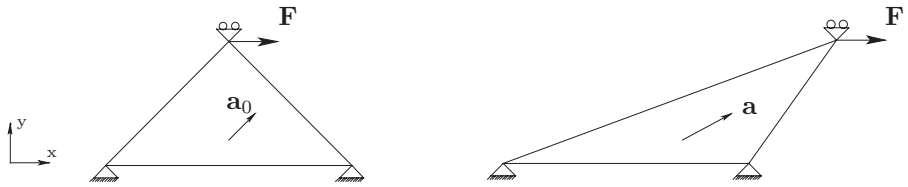


*Figure D.2: Initial and final configurations of an element with one fibre family with elasto-plastic deformation.*

| | | |
|---|---|---|
| E | [GPa] | 3 |
| $\sigma_0$ | [MPa] | 30 |
| C | [MPa] | 100 |
| $\varepsilon_0$ | [-] | $5{\cdot}10^{-5}$ |
| $n$ | [-] | 0.6 |

*Table D.1: Parameters of the Nadai stress-strain curve.*

## D.3 Application

The elasto-plastic material model has been implemented in MATLAB©. The initial and final geometries of a one element performance test are shown in figure D.2. The initial width, height and thickness of the element is 1 mm. Plane stress conditions are assumed. The fibre is initially oriented at 45° with respect to the $x$-axis. The applied force is 20 N. The fibre deforms according to a Nadai stress-strain curve, in which the yield stress $\sigma_y$ is given by:

$$\sigma_y = \sigma_0 + C(\varepsilon_0 + \varepsilon_p)^n, \tag{D.27}$$

with $\sigma_0$, $C$, $\varepsilon_0$ and $n$ the parameters of the curve and $\varepsilon_p$ the plastic strain. The values of the parameters are be found in table D.1 and a plot of the stress strain curve is found in figure 2.8. The material behavior is time independent. The size of the plastic strain increments is solved iteratively, if the elastic limit is exceeded. The derivative of the yield stress with respect to the plastic strain $\varepsilon_p$ is used in the consistent tangent and is given by:

$$\frac{\partial \sigma_y}{\partial \varepsilon_p} = nC(\varepsilon_0 + \varepsilon_p)^{n-1}. \tag{D.28}$$

The plastic strain reached 0.99 mm/mm. A convergence plot of this simulation is given in figure D.3. The displacement of the top node and the convergence power values are given in table D.2. The definition of the error norms and an

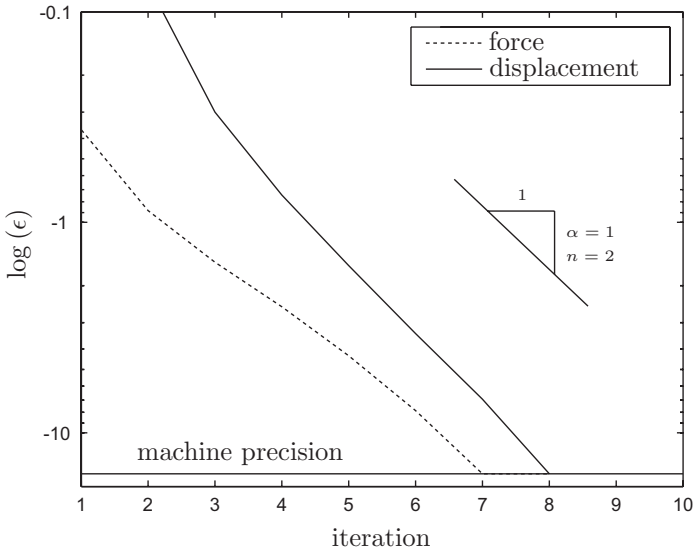


*Figure D.3: Convergence plot of the one element test including plasticity. The slope $n = 2$ indicates quadratic convergence.*

| iteration | $u$ [mm] | $n$ |
|---|---|---|
| 1 | 0.053 333 333 333 333 | - |
| 2 | 0.341 389 350 139 047 | 4.06 |
| 3 | 0.684 642 918 990 075 | 2.48 |
| 4 | 0.835 619 074 585 799 | 2.16 |
| 5 | 0.856 772 807 043 763 | 2.10 |
| 6 | 0.857 132 271 864 668 | 2.05 |
| 7 | 0.857 132 373 407 435 | 2.25 |
| 8 | 0.857 132 373 407 435 | 1.00 |

*Table D.2: Displacement of the top node and the convergence power value. The significant digits are underlined.*

explanation of the convergence powers can be found in section C.2. The slope of the graphs and the convergence power values from the table prove that the convergence speed is quadratic.

# Appendix E

# Generalised elastic anisotropic material model

Hooke's law states that stress increments are linearly coupled to strain increments by a fourth order stiffness tensor ${}^4\mathbf{E}$. The most general form of the stiffness tensor contains 21 independent material constants. In this appendix, a method is derived that gives the Cauchy stress, the finite element nodal forces and the consistent tangent for a generalised anisotropic material. The equations are expressed using a **constant** stiffness tensor, regardless of the size of the deformation increments and the rigid rotations. A one element example is given, in which quadratic convergence speed is shown for an orthotropic material.

## E.1 Cauchy stress

The deformation gradient $\mathbf{F}$ is decomposed in a stretch tensor $\mathbf{G}$ and a subsequent rotation $\mathbf{R}$. The local stress $\boldsymbol{\tau}$, the stress before rotation, of the generalised anisotropic model is given by:

$$\boldsymbol{\tau} = \frac{\rho}{2\rho_0}(\mathbf{G} \cdot {}^4\mathbf{I} \cdot \mathbf{G}) : {}^4\mathbf{E} : (\mathbf{C} - \mathbf{I}), \tag{E.1}$$

with $\rho$ the density, ${}^4\mathbf{E}$ the fourth order material stiffness tensor and $\mathbf{C}$ the right Cauchy-Green tensor. The Cauchy stress is found by rotating the local stress tensor:

$$\boldsymbol{\sigma} = \mathbf{R} \cdot \boldsymbol{\tau} \cdot \mathbf{R}^T. \tag{E.2}$$

The Cauchy stress is used in the evaluation of the nodal forces, given by equation (B.1).

## E.2 Consistent tangent

The consistent tangent matrix is given by equation (B.3). The rate of the Cauchy stress with respect to time is given by equation (C.4). The consistent tangent can now be written as the volume integral of the following five parts:

$$\overleftarrow{\mathbf{w}\nabla} : \dot{\boldsymbol{\sigma}} - \overleftarrow{\mathbf{w}\nabla} \cdot \overleftarrow{\mathbf{v}\nabla} : \boldsymbol{\sigma} + \overleftarrow{\mathbf{w}\nabla} : \boldsymbol{\sigma} \frac{\dot{J}}{J} = \underbrace{\overleftarrow{\mathbf{w}\nabla} : \dot{\mathbf{R}} \cdot \boldsymbol{\tau} \cdot \mathbf{R}^T}_{a} + \tag{E.3}$$

$$\underbrace{\overleftarrow{\mathbf{w}\nabla} : \mathbf{R} \cdot \boldsymbol{\tau} \cdot \dot{\mathbf{R}}^T}_{b} + \underbrace{\overleftarrow{\mathbf{w}\nabla} : \mathbf{R} \cdot \dot{\boldsymbol{\tau}} \cdot \mathbf{R}^T}_{c} - \underbrace{\overleftarrow{\mathbf{w}\nabla} \cdot \overleftarrow{\mathbf{v}\nabla} : \boldsymbol{\sigma}}_{d} + \underbrace{\overleftarrow{\mathbf{w}\nabla} : \boldsymbol{\sigma} \frac{\dot{J}}{J}}_{e}.$$

With the arbitrary split of $\mathbf{F}$ into $\mathbf{R} \cdot \mathbf{G}$, the rate of rotation tensor $\dot{\mathbf{R}}$ is expressed as:

$$\dot{\mathbf{R}} = \mathbf{L} \cdot \mathbf{R} - \mathbf{R} \cdot \mathbf{L}_g, \tag{E.4}$$

with $\mathbf{L}$ the velocity gradient and $\mathbf{L}_g$ the adapted velocity gradient defined as:

$$\mathbf{L}_g = \dot{\mathbf{G}} \cdot \mathbf{G}^{-1}. \tag{E.5}$$

The rate of $\mathbf{G}$ is then given by:

$$\dot{\mathbf{G}} = \mathbf{L}_g \cdot \mathbf{G}. \tag{E.6}$$

Part $a$ and $b$ of equation (E.3) can now be written as:

$$\begin{aligned} a &= \overleftarrow{\mathbf{w}\nabla} : (\mathbf{L} \cdot \boldsymbol{\sigma} - \mathbf{L}_g \cdot \boldsymbol{\sigma}) \\ b &= \overleftarrow{\mathbf{w}\nabla} : (\boldsymbol{\sigma} \cdot \mathbf{L}^T - \boldsymbol{\sigma} \cdot \mathbf{L}_g^T). \end{aligned} \tag{E.7}$$

Differentiating the local stress tensor $\boldsymbol{\tau}$ from equation (E.1) results in

$$\dot{\boldsymbol{\tau}} = \frac{\dot{\rho}}{\rho} \boldsymbol{\tau} + \mathbf{L}_g \cdot \boldsymbol{\tau} + \boldsymbol{\tau} \cdot \mathbf{L}_g^T + \frac{\rho}{2\rho_0} (\mathbf{G} \cdot {}^4\mathbf{I} \cdot \mathbf{G}) : {}^4\mathbf{E} : \dot{\mathbf{C}}. \tag{E.8}$$

Part $c$ of equation (E.3) is then written as:

$$c = \underbrace{\frac{\dot{\rho}}{\rho} \overleftarrow{\mathbf{w}\nabla} : \boldsymbol{\sigma}}_{c_1} + \underbrace{\overleftarrow{\mathbf{w}\nabla} : \mathbf{L}_g \cdot \boldsymbol{\sigma}}_{c_2} + \underbrace{\overleftarrow{\mathbf{w}\nabla} : \boldsymbol{\sigma} \cdot \mathbf{L}_g^T}_{c_3} + \tag{E.9}$$

$$\underbrace{\frac{\rho}{2\rho_0} \overleftarrow{\mathbf{w}\nabla} : \left\{ \mathbf{R} \cdot \left( (\mathbf{G} \cdot {}^4\mathbf{I} \cdot \mathbf{G}) : {}^4\mathbf{E} : \dot{\mathbf{C}} \right) \cdot \mathbf{R}^T \right\}}_{c_4}.$$

With the use of equations (A.16) and (H.3), $c_4$ is rewritten as

$$\begin{aligned} c_4 &= \frac{\rho}{\rho_0}\mathbf{w}\overleftarrow{\nabla} : \left\{\mathbf{R}\cdot\left(\left(\mathbf{G}\cdot{}^4\mathbf{I}\cdot\mathbf{G}\right) : {}^4\mathbf{E} : \mathbf{F}^T\cdot\mathbf{D}\cdot\mathbf{F}\right)\cdot\mathbf{R}^T\right\} \\ &= \frac{\rho}{\rho_0}\mathbf{w}\overleftarrow{\nabla} : \left(\mathbf{F}\cdot{}^4\mathbf{I}\cdot\mathbf{F}\right) : {}^4\mathbf{E} : \left(\mathbf{F}^T\cdot{}^4\mathbf{I}\cdot\mathbf{F}^T\right) : \mathbf{D}. \end{aligned} \tag{E.10}$$

The sum of $c_1$ and $e$ is equal to zero, (A.10),

$$\begin{aligned} c_1 + e &= \frac{\dot{\rho}}{\rho}\mathbf{w}\overleftarrow{\nabla} : \boldsymbol{\sigma} + \mathbf{w}\overleftarrow{\nabla} : \boldsymbol{\sigma}\frac{\dot{J}}{J} \\ &= 0. \end{aligned} \tag{E.11}$$

The remaining terms can be rewritten using (H.1) and (H.2),

$$\begin{aligned} a + b + c_2 + c_3 + d &= \mathbf{w}\overleftarrow{\nabla} : \left(\mathbf{L}\cdot\boldsymbol{\sigma} + \boldsymbol{\sigma}\cdot\mathbf{L}^T\right) + \mathbf{w}\overleftarrow{\nabla}\cdot\mathbf{v}\overleftarrow{\nabla} : \boldsymbol{\sigma} \\ &= \overrightarrow{\nabla}\mathbf{w}\cdot\mathbf{v}\overleftarrow{\nabla} : \boldsymbol{\sigma}. \end{aligned} \tag{E.12}$$

The consistent tangent matrix for the generalised anisotropic model follows by the addition of (E.10) and (E.12),

$$\begin{aligned} K = \int_V \Bigg[\frac{\rho}{\rho_0}\cdot\tfrac{1}{2}\left(\mathbf{w}\overleftarrow{\nabla} + \overrightarrow{\nabla}\mathbf{w}\right) : \left(\mathbf{F}\cdot{}^4\mathbf{I}\cdot\mathbf{F}\right) : {}^4\mathbf{E} : \\ \left(\mathbf{F}^T\cdot{}^4\mathbf{I}\cdot\mathbf{F}^T\right) : \tfrac{1}{2}\left(\mathbf{v}\overleftarrow{\nabla} + \overrightarrow{\nabla}\mathbf{v}\right) + \overrightarrow{\nabla}\mathbf{w}\cdot\mathbf{v}\overleftarrow{\nabla} : \boldsymbol{\sigma}\Bigg]\, dV. \end{aligned} \tag{E.13}$$

## E.3 Application

The generalised anisotropic material model has been implemented in MATLAB©. Figure E.1 shows the initial and final deformed shapes of a one element simulation with an orthotropic material model. An orthotropic material has nine independent material parameters. Plane stress conditions are assumed and only in-plane behavior is of interest. These assumptions reduce the total number of independent material parameters to four: $E_1 = 10$ MPa, $E_2 = 1$ MPa, $G_{12} = 0.5$ MPa and $\nu_{12} = 0.33$. The principal stiffness directions coincide with the axes of the coordinate system, as indicated in figure E.1. The initial width, height and thickness of the element is 1 mm and the applied force was 0.75 N. The triangle has a linear displacement field.

A convergence plot of this simulation is given in figure E.2. The horizontal displacement of the top node and the convergence power values are given in table E.1. The definition of the error norms and an explanation of the convergence powers were introduced in section C.2. The slope of the graphs and the convergence power values from the table prove that the convergence speed is quadratic for this example with an orthotropic material model.

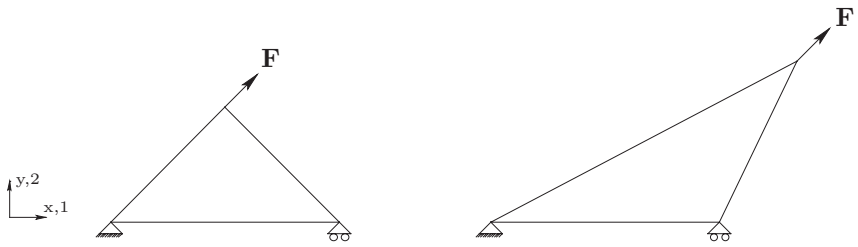


*Figure E.1: Initial and final configurations.*

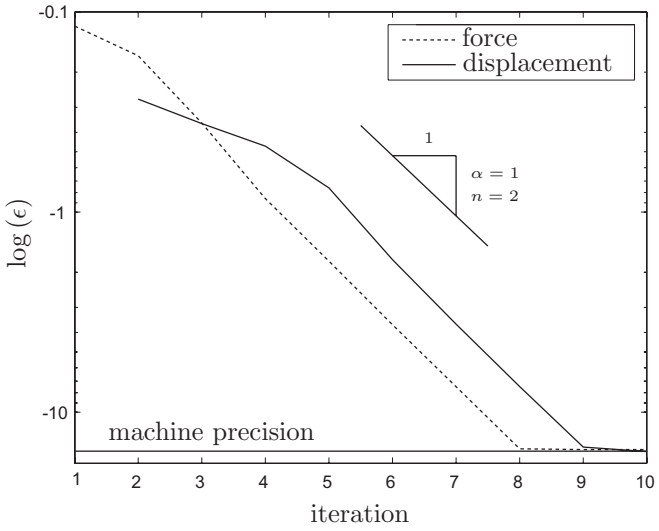


*Figure E.2: Convergence plot of the one element test. The slope $n = 2$ indicates quadratic convergence.*

| iteration | $u$ [mm] | $n$ |
|---|---|---|
| 1 | 2.834 437 532 386 275 | - |
| 2 | 1.905 639 849 410 504 | 1.32 |
| 3 | 1.344 467 756 660 898 | 1.29 |
| 4 | 1.003 647 611 982 085 | 1.61 |
| 5 | 0.860 380 926 041 880 | 2.28 |
| 6 | 0.844 556 443 852 118 | 2.10 |
| 7 | 0.844 358 701 391 119 | 2.05 |
| 8 | 0.844 358 670 901 146 | 2.00 |
| 9 | 0.844 358 670 901 145 | 1.05 |

*Table E.1: Horizontal displacement of the top node and the convergence power value. The significant digits are underlined.*

# Appendix F

# Mooney-Rivlin material model

The Mooney-Rivlin (MR) material model is a generalisation of the neo-Hookean material model. The non-linear stress-strain response of the MR material model is widely used to model the response of (nearly incompressible) rubber-like solids and polymers. The Cauchy stress and the consistent tangent matrices of the MR material model are presented in this section. An example is given, where a cube of a MR material is compressed to half of the original height. This simulation shows quadratic convergence, proving the consistency of the tangents derived.

## F.1 Cauchy stress

The stress state of a Mooney-Rivlin material is given by [1]

$$\boldsymbol{\sigma} = \underbrace{\frac{g_0}{J}(J-1)\mathbf{I}}_{\boldsymbol{\sigma}_a} + \underbrace{\frac{g_1}{J}(\mathbf{B}-\mathbf{I})}_{\boldsymbol{\sigma}_b} + \underbrace{\frac{g_2}{J}(\mathbf{B}^{-1}-\mathbf{I})}_{\boldsymbol{\sigma}_c}, \tag{F.1}$$

in which $g_0$, $g_1$ and $g_2$ are the material parameters, $J$ is the volume ratio and $\mathbf{B}$ is the left Cauchy-Green strain tensor given by:

$$\mathbf{B} = \mathbf{F} \cdot \mathbf{F}^T. \tag{F.2}$$

The Cauchy stress is used in the evaluation of the nodal forces, given by equation (B.1).

## F.2 Consistent tangent

The starting point is equation (B.3):

$$K = \int_V \mathbf{w}\overleftarrow{\nabla} : \dot{\boldsymbol{\sigma}}\, dV - \int_V \mathbf{w}\overleftarrow{\nabla} \cdot \mathbf{v}\overleftarrow{\nabla} : \boldsymbol{\sigma}\, dV + \int_V \mathbf{w}\overleftarrow{\nabla} : \boldsymbol{\sigma}\tfrac{\dot{J}}{J}\, dV. \tag{F.3}$$

This equation will be evaluated for the three stress components $\boldsymbol{\sigma}_a$, $\boldsymbol{\sigma}_b$ and $\boldsymbol{\sigma}_c$ of equation (F.1) individually, in turn leading to three components in the tangent matrix,

$$K = K_a + K_b + K_c. \tag{F.4}$$

The rate of the stress component $\boldsymbol{\sigma}_a$ is given by

$$\dot{\boldsymbol{\sigma}}_a = -\frac{\dot{J}}{J}\boldsymbol{\sigma}_a + \frac{\dot{J}}{J} g_0\, \mathbf{I}. \tag{F.5}$$

The tangent matrix (F.3) for this stress component is found using equations (A.5), (A.11), (H.2) and (H.6),

$$K_a = \int_V \left[ g_0 \cdot \tfrac{1}{2}(\mathbf{w}\overleftarrow{\nabla} + \overrightarrow{\nabla}\mathbf{w}) : \mathbf{II} : \tfrac{1}{2}(\mathbf{v}\overleftarrow{\nabla} + \overrightarrow{\nabla}\mathbf{v}) - \mathbf{w}\overleftarrow{\nabla} \cdot \mathbf{v}\overleftarrow{\nabla} : \boldsymbol{\sigma}_a \right] dV. \tag{F.6}$$

The rate of the stress component $\boldsymbol{\sigma}_b$ reads

$$\begin{aligned} \dot{\boldsymbol{\sigma}}_b &= -\frac{\dot{J}}{J}\boldsymbol{\sigma}_b + \frac{g_1}{J}\dot{\mathbf{B}} \\ &= -\frac{\dot{J}}{J}\boldsymbol{\sigma}_b + \frac{g_1}{J}\left( \mathbf{L}\cdot\mathbf{B} + \mathbf{B}\cdot\mathbf{L}^T \right) \\ &= -\frac{\dot{J}}{J}\boldsymbol{\sigma}_b + \mathbf{L}\cdot\boldsymbol{\sigma}_b + \boldsymbol{\sigma}_b\cdot\mathbf{L}^T + \frac{2g_1}{J}\mathbf{D}, \end{aligned} \tag{F.7}$$

in which equation (A.14) was used. The tangent matrix (F.3) of part $b$ is now elaborated using a similar procedure as for (F.6), resulting in

$$K_b = \int_V \left[ \frac{2g_1}{J} \cdot \tfrac{1}{2}(\mathbf{w}\overleftarrow{\nabla} + \overrightarrow{\nabla}\mathbf{w}) : \tfrac{1}{2}(\mathbf{v}\overleftarrow{\nabla} + \overrightarrow{\nabla}\mathbf{v}) + \overrightarrow{\nabla}\mathbf{w}\cdot\mathbf{v}\overleftarrow{\nabla} : \boldsymbol{\sigma}_b \right] dV. \tag{F.8}$$

Using equation (A.15), the rate of the stress component $\boldsymbol{\sigma}_c$ is expressed as:

$$\begin{aligned} \dot{\boldsymbol{\sigma}}_c &= -\frac{\dot{J}}{J}\boldsymbol{\sigma}_c + \frac{g_2}{J}\dot{\mathbf{B}}^{-1} \\ &= -\frac{\dot{J}}{J}\boldsymbol{\sigma}_b + \frac{g_2}{J}\left( -\mathbf{B}^{-1}\cdot\mathbf{L} - \mathbf{L}^T\cdot\mathbf{B}^{-1} \right) \\ &= -\frac{\dot{J}}{J}\boldsymbol{\sigma}_b - \boldsymbol{\sigma}_c\cdot\mathbf{L} - \mathbf{L}^T\cdot\boldsymbol{\sigma}_c - \frac{2g_2}{J}\mathbf{D}. \end{aligned} \tag{F.9}$$

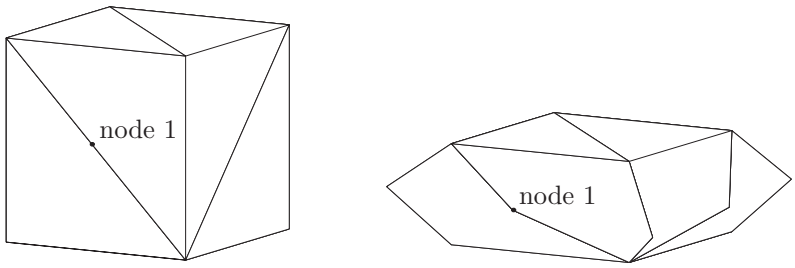


*Figure F.1: Compression of a cube to 50% of the original height. The cube is meshed with six 10-node quadratic tetrahedrons.*

An elaboration of (F.3) similar to the procedure as used for (F.6), results in the tangent for this component,

$$K_c = \int_V \Big[ -\frac{2g_2}{J} \cdot \tfrac{1}{2}(\mathbf{w}\overleftarrow{\nabla} + \overrightarrow{\nabla}\mathbf{w}) : \tfrac{1}{2}(\mathbf{v}\overleftarrow{\nabla} + \overrightarrow{\nabla}\mathbf{v}) - \Big( \mathbf{w}\overleftarrow{\nabla} \cdot \overrightarrow{\nabla}\mathbf{v} + \overrightarrow{\nabla}\mathbf{w} \cdot \overrightarrow{\nabla}\mathbf{v} + \mathbf{w}\overleftarrow{\nabla} \cdot \mathbf{v}\overleftarrow{\nabla} \Big) : \boldsymbol{\sigma}_c \Big] \, dV. \tag{F.10}$$

The complete tangent is found by evaluating equation (F.4).

## F.3 Application

The Mooney-Rivlin model has been implemented in 10-node quadratic tetrahedron elements, using MATLAB©. Figure F.1 shows the initial and final configurations of an example, in which a cube is compressed to 50% of the original height. The cube is meshed with 6 elements. The initial size of the cube is 1 mm. The Mooney-Rivlin parameters are $g_0$ = 1.0 MPa, $g_1$ = 0.0315 MPa and $g_2$ = -0.0415 MPa [2].

The simulation converged to machine precision within eight iterations. The convergence behaviour of the simulation does not depend on the initial size of the cube, only on the ratio of compression. The convergence speed of the simulation is plotted in figure F.2. The vertical displacement and the convergence power values of node one are given in table F.1. Node one is indicated in figure F.1. The error norms and an explanation of the convergence powers were introduced in section C.2. The slope of the graphs and the convergence power values from the table show that the convergence rate is quadratic.

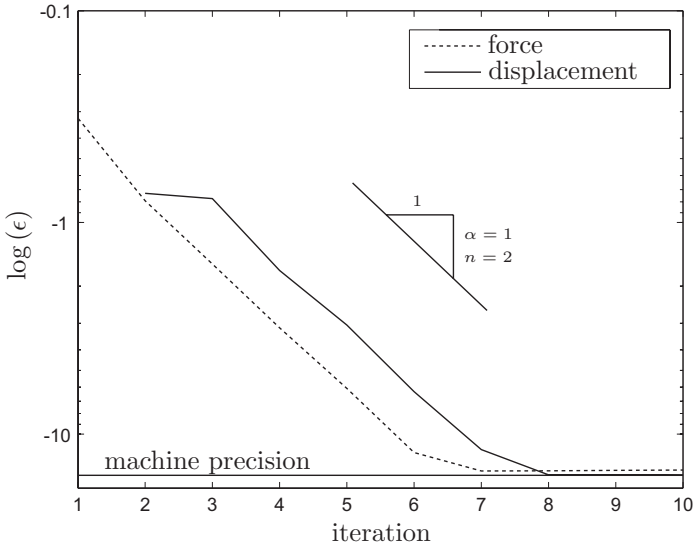


*Figure F.2: Convergence plot of the compression of a rubber cube. The slope $n = 2$ indicates quadratic convergence.*

| iteration | $u$ [mm] | $n$ |
|---|---|---|
| 1 | -0.260 686 309 183 553 | - |
| 2 | -0.244 368 257 447 417 | 1.06 |
| 3 | -0.255 314 031 414 305 | 2.18 |
| 4 | -0.253 851 874 881 629 | 1.80 |
| 5 | -0.253 774 065 876 776 | 2.07 |
| 6 | -0.253 774 005 340 125 | 1.88 |
| 7 | -0.253 774 005 340 036 | 1.32 |
| 8 | -0.253 774 005 340 036 | 1.00 |

*Table F.1: Vertical displacement of node 1 and the convergence power value. The significant digits are underlined.*

# Bibliography

[1] R. Ogden. *Non-linear Elastic Deformations*. Dover Publications Inc., 1997. ISBN-13: 978-0486696485.

[2] G. K. Klute and B. Hannaford. 'Accounting for Elastic Energy Storage in McKibben Artificial Muscle Actuators'. *J Dyn Syst-T ASME*, 122:386–388, 2000.

# Appendix G

# Uniform surface pressure on planar three node elements

The consistent linearisation of boundary conditions can decrease simulation times significantly. This section discusses uniform surface pressures on planar three node elements. The resulting nodal forces are given, as well as the consistent linearisation of these forces with respect to the nodal displacements. The inflation of a rubber ball was simulated and the results are presented at the end of the section. The simulation shows quadratic convergence, proving the consistency of the tangent.

## G.1 Nodal forces

The total force $F_p$, exerted by a uniform pressure $p$ on the face of a planar membrane element is given by

$$F_p = p \cdot A, \tag{G.1}$$

in which A denotes the surface area of the element. The exerted force is equally distributed among the nodes for the three node planar element. The nodal force vector $\mathbf{F}$ is therefore given by

$$\mathbf{F} = -\mathbf{n} \cdot \tfrac{1}{3} F_p, \tag{G.2}$$

where $\mathbf{n}$ denotes the normal on the element.

## G.2 Consistent tangent

The element is first rotated from the global coordinate system to the $xy$-plane by the rotation tensor $\mathbf{R}$. This rotation is depicted in figure G.1, in which

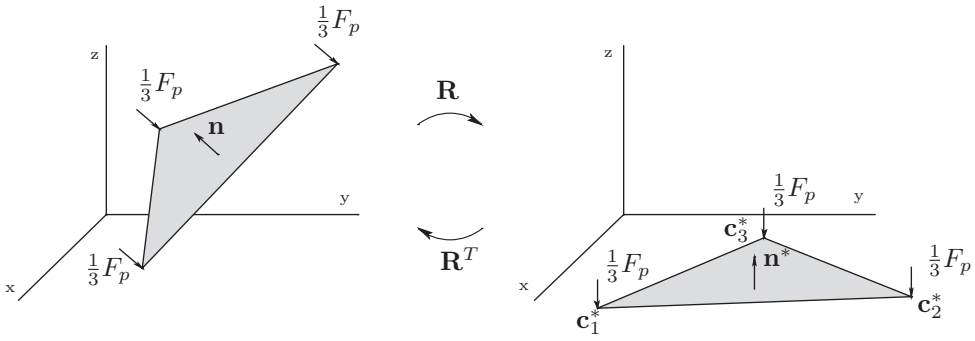


*Figure G.1: Rotation of the element from the three dimensional space to the xy-plane and back.*

$\mathbf{c}^*$ are the rotated coordinate vectors of the nodes. The rotated normal $\mathbf{n}^*$ now points in the $z$-direction. The rotated situation will be referred to as the local coordinate system, indicated by the asterisk. The next step is to derive the local tangent matrix $\mathbf{K}^*$. The global tangent $\mathbf{K}$ is subsequently found by rotating the local stiffness matrix to the global coordinate system,

$$\mathbf{K} = \mathbf{R}^T \cdot \mathbf{K}^* \cdot \mathbf{R}. \tag{G.3}$$

The local force vector $\mathbf{F}^*$ is needed to find the local tangent matrix $\mathbf{K}^*$. This local force vector as a result of the uniform pressure $p$ is given by

$$\mathbf{F}^* = -\tfrac{1}{3}F_p \cdot \mathbf{n}^*, \tag{G.4}$$

in which $F_p$ is given by equation (G.1). The rate form of (G.4) reads

$$\dot{\mathbf{F}}^* = -\underbrace{\tfrac{1}{3}F_p \cdot \dot{\mathbf{n}}^*}_{a} - \underbrace{\tfrac{1}{3}F_p \cdot \mathbf{n}^* \cdot \frac{\dot{A}}{A}}_{b}. \tag{G.5}$$

Part $a$ contains the rate of the local normal $\mathbf{n}^*$. This rate can be found by expressing the normal in the local coordinates:

$$\mathbf{n}^* = \frac{1}{L}\mathbf{s}_1^* \times \mathbf{s}_2^*, \tag{G.6}$$

in which the vectors $\mathbf{s}_1^*$ and $\mathbf{s}_2^*$ are the direction vectors of two element sides. These vectors are expressed using the coordinate vectors $\mathbf{c}^*$ of the nodes,

$$\begin{aligned} \mathbf{s}_1^* &= \mathbf{c}_2^* - \mathbf{c}_1^* \\ \mathbf{s}_2^* &= \mathbf{c}_3^* - \mathbf{c}_1^*. \end{aligned} \tag{G.7}$$

The nodal coordinate vectors $\mathbf{c}^*$ are shown in figure G.1. The length $L$ is given by:

$$L = \|\mathbf{s}_1^* \times \mathbf{s}_2^*\|. \tag{G.8}$$

The first order derivative of the local normal $\mathbf{n}^*$ depends on the nodal displacements in the $z$-direction only and not on the in-plane displacements. This is an advantage of rotating the element to the $xy$-plane first. The length change of $L$ is a second order effect as well. The rate of $\mathbf{n}^*$ follows from equation (G.6),

$$\frac{\partial \mathbf{n}_*}{\partial w_1^*} = \frac{1}{L} \begin{Bmatrix} y_3^* - y_2^* \\ x_2^* - x_3^* \\ 0 \end{Bmatrix}, \tag{G.9}$$

in which $w_1^*$ is the local displacement in the $z$-direction of the first node and $x_i^*$ and $y_i^*$ are the local nodal coordinates. The derivatives with respect to the vertical displacements of the other nodes can be derived similarly.

Part $b$ of equation (G.5) is evaluated using equation (A.11),

$$b = -\tfrac{1}{3} F_p \cdot \mathbf{n}^* \cdot \mathrm{tr}\,(\mathbf{D}^*), \tag{G.10}$$

in which $\mathbf{D}^*$ denotes the rate of deformation tensor.

The local tangent matrix (G.5) is found by combining (G.9) and (G.10). The global tangent matrix, equation (G.3), with respect to the displacements of the first node, is hence given by

$$\mathbf{K} = -\frac{F_p}{3} \cdot \mathbf{R}^T \cdot \begin{bmatrix} 0 & 0 & \frac{1}{L}(y_3^* - y_2^*) \\ 0 & 0 & \frac{1}{L}(x_2^* - x_3^*) \\ \mathrm{tr}\,(\mathbf{D}^*) & \mathrm{tr}\,(\mathbf{D}^*) & 0 \end{bmatrix} \cdot \mathbf{R}. \tag{G.11}$$

The tangent matrices with respect to the displacements of the other nodes can be derived similarly.

## G.3 Application

A linear, three node membrane element including a uniform surface pressure has been implemented in MATLAB©. An example of the inflation of a thin-walled rubber ball will be presented in this section. The initial and final geometries are shown in figure G.2. The initial radius of the ball is 50 mm and the wall thickness is 3 mm. The ball is meshed with 320 linear membrane

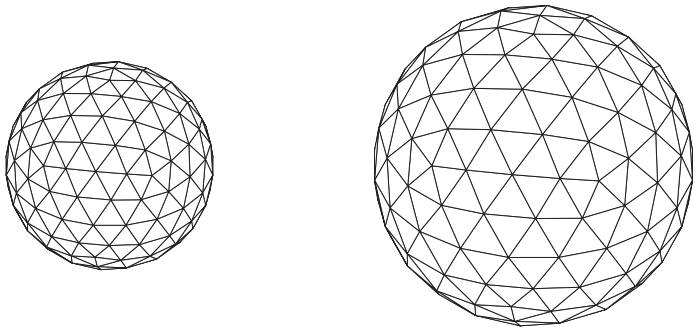

*Figure G.2: A thin-walled rubber ball in the initial and inflated state.*

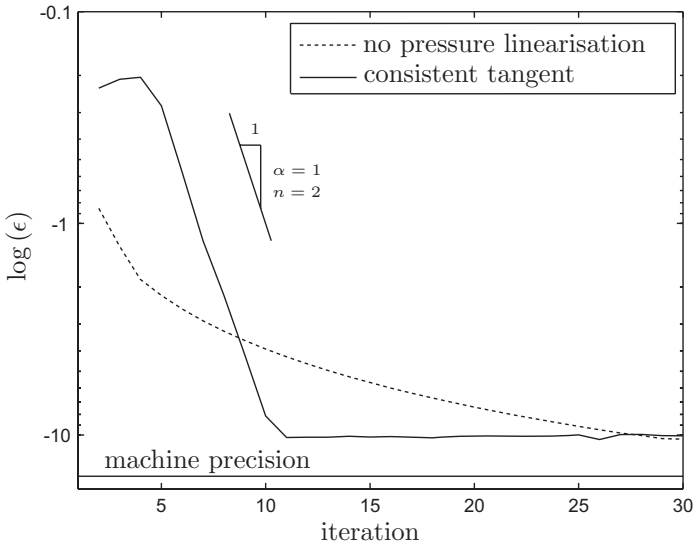


*Figure G.3: Convergence plot of the inflated ball example. The slope $n = 2$ indicates quadratic convergence.*

elements. The volume of the elements remains constant and plane stress conditions are assumed. The rubber material is modelled using a Mooney-Rivlin material model as introduced in appendix F, with $g_1 = 3$ MPa and $g_2 = 1$ MPa. The parameter $g_0$ is redundant in this case, due to the constant volume assumption. Inertia was included to avoid rigid body motions that introduce singularities. The density of the material was set to 1500 kg/m$^3$. The internal pressure was set to 0.5 bar. The radius of the ball increased from 50 to 77.1 mm during pressurisation.

| iteration | $u$ [mm] | $n$ |
|---|---|---|
| 1 | 180.017 437 433 241 | - |
| 2 | 112.000 643 619 285 | 0.91 |
| 3 | 68.276 616 473 731 | 0.98 |
| 4 | 41.858 938 478 218 | 1.36 |
| 5 | 28.780 789 031 673 | 2.07 |
| 6 | 26.103 073 655 063 | 2.10 |
| 7 | 27.075 399 952 663 | 1.81 |
| 8 | 27.113 572 866 349 | 1.91 |
| 9 | 27.114 057 744 545 | 1.94 |
| 10 | 27.114 057 802 066 | 1.22 |
| 11 | 27.114 057 802 902 | 1.04 |
| 12 | 27.114 057 802 242 | 0.97 |

*Table G.1: Radial displacement of node 1 an the convergence power value. The significant digits are underlined.*

Figure G.3 shows the convergence plot of this simulation, using only the material tangent and including the linearisation for the uniform pressure as derived in the previous section. The radial displacement of node 1 and the convergence power values are given in table G.1. The consistent tangent takes into account the increase in nodal forces due to the increase in surface area. This explains the large displacements found in the first iteration. A radial expansion of the ball increases the surface area and hence the total force exerted by the pressure, while there is (yet) no membrane tension present to restrain this expansion. Membrane stresses are present from the second iteration on and the radial displacement converges to the final value.

The simulation using only the material tangent converges much slower, despite the lower overshoot in the first iteration. The maximum number of significant digits obtained is 11. This is probably due to the calculation of the inverse matrices of the left Cauchy-Green strain tensor $\mathbf{B}$, used in the Mooney-Rivlin material model. Significant digits are lost in this process and the maximum number of 15 significant digits cannot be obtained.

# Appendix H

# Tensor algebra

Tensor and vector operations are indispensable in the mathematical description of mechanics and dynamics. They are well covered in literature. A formal and extensive overview can be found in the work of Bowen and Wang [1, 2]. The work of Heinbockel [3] provides a good introduction to tensor calculus. This appendix contains only a number of tensor operations that were frequently used in this thesis.

The following nomenclature is used:

| | |
|---|---|
| a | scalar |
| $\mathbf{a}$ | vector |
| $\mathbf{A}$ | second order tensor |
| ${}^{\mathrm{n}}\mathbf{A}$ | $\mathrm{n}^{\mathrm{th}}$ order tensor |
| $\mathbf{A}_s$ | symmetric tensor |

The following six tensor operations can be easily derived in index notation.

$$\begin{aligned} \mathbf{A} : (\mathbf{B} \cdot \mathbf{C}) &= (\mathbf{A}^T \cdot \mathbf{B}) : \mathbf{C}^T \\ &= \mathbf{C}^T : (\mathbf{A}^T \cdot \mathbf{B}) \\ &= (\mathbf{C} \cdot \mathbf{A}^T) : \mathbf{B} \end{aligned} \tag{H.1}$$

$$\begin{aligned} \mathbf{A} : \mathbf{B}_s &= \mathbf{A}^T : \mathbf{B}_s \\ &= \tfrac{1}{2}(\mathbf{A} + \mathbf{A}^T) : \mathbf{B}_s \end{aligned} \tag{H.2}$$

$$(\mathbf{A} \cdot {}^4\mathbf{I} \cdot \mathbf{C}) : \mathbf{B} = \mathbf{A} \cdot \mathbf{B} \cdot \mathbf{C}^T \tag{H.3}$$

$$\mathbf{aaaa} : \mathbf{B}_s = \mathbf{aa} \cdot \mathbf{B}_s \cdot \mathbf{aa} \tag{H.4}$$

$$\mathbf{B} : (\mathbf{aa} \cdot \mathbf{C} \cdot \mathbf{aa}) = (\mathbf{B} \cdot \mathbf{aa}) : (\mathbf{aa} \cdot \mathbf{C}) \tag{H.5}$$

$$\mathrm{tr}\,(\mathbf{A}) = \mathbf{I} : \mathbf{A} \tag{H.6}$$

## Bibliography

[1] R. M. Bowen and C. C. Wang. *Introduction to Vectors and Tensors, Vol. 1, Linear and Multilinear Algebra*. Plenum Press, New York, 1976. URL www1.mengr.tamu.edu/rbowen/.

[2] R. M. Bowen and C. C. Wang. *Introduction to Vectors and Tensors, Vol. 2, Vector and Tensor Analysis*. Plenum Press, New York, 1976. URL www1.mengr.tamu.edu/rbowen/.

[3] J. H. Heinbockel. *Introduction to Tensor Calculus and Continuum Mechanics*. Trafford Publishing, Canada, 2001. ISBN-13: 978-1553691334.

# Nawoord

Dit proefschrift is het resultaat van het werk dat ik uitgevoerd heb in de periode tussen september 2002 en september 2007. Het eerste deel van dit onderzoek is in deeltijd uitgevoerd, zodat ik tijd kon besteden aan mijn favoriete sport: roeien. Dit was niet mogelijk geweest zonder de medewerking van de Universiteit Twente en mijn promotor, Remko Akkerman. Gelukkig dragen beiden dit soort persoonlijke ontwikkelingen een warm hart toe, iets waarvan ik tijdens mijn studententijd ook al dankbaar gebruik heb gemaakt. Bedankt hiervoor.

De inzet en het enthousiasme van mijn promotoren Remko Akkerman en Han Huétink heeft er zeker aan bijgedragen dat ik deze belangrijke periode in mijn carrière met een goed gevoel en een goed resultaat afsluit. Hun open-deur-mentaliteit heb ik hierbij zeer gewaardeerd. Remko, als begeleider, bedankt voor de sturing en motivatie, vooral op de momenten dat het allemaal even vast leek te zitten.

Het dagelijkse plezier op het werk wordt natuurlijk voor een groot deel bepaald door de collega's. Collega's, ik heb zeer genoten van de koffiepauzes, borrels en mountainbike uitjes die we samen ondernomen hebben. Uit deze groep collega's wil ik een aantal mensen in het bijzonder noemen. Edwin Lamers, Sebastiaan Wijskamp en Richard Loendersloot, natuurlijk bedankt voor jullie input op sociaal gebied, maar ik weet zeker dat de discussies over onze onderzoeken ons allemaal vooruit geholpen hebben. Laurent Warnet, bedankt voor je inhoudelijke advies bij het schrijven van dit proefschrift en je hulp bij het opzetten en uitvoeren van experimenten. Ik wil ook zeker Ashok Sridhar niet vergeten te bedanken voor zijn spellings- en grammaticacorrecties van dit proefschrift.

Door het onderwerp van mijn onderzoek, eindige-elementensimulaties, stond ik ook met één been in de DiekA-groep. DiekA is de naam van het eindige-elementenpakket dat door deze groep ontwikkeld wordt en deze dame is

tevens de grootste concurrent van menig promovenduspartner. Hoewel de besprekingen op vrijdagochtend plaats vonden, leverden ze veel informatie, bruikbare tips en ideeën op. Van de DiekA-groep wil ik naast Han Huétink vooral Timo Meinders, Bert Geijselaers en Ton van de Boogaard bedanken voor hun hulp en adviezen. Daarnaast waren de Esaform-conferenties met de DiekA-groep ook altijd een groot succes. Onze roadtrips door Schotland en Spanje zal ik niet snel vergeten.

Velen hebben in de afgelopen vijf jaar een bijgedrage geleverd aan mijn onderzoek, direct of indirect. Een complete lijst hiervan geven is praktisch ondoenlijk, dus nu komt de vraag waar de lijst gaat stoppen. In ieder geval niet voor ik de volgende mensen genoemd heb. Tanja, Belinda en Debbie, bedankt voor het afhandelen van de papierwinkels die altijd maar weer opduiken. Dankzij jullie heb ik er vaak niet zoveel van gemerkt. Ook een flink aantal studenten heeft een bijdrage geleverd aan het onderzoek. De bijdragen van Lieuwe van de Meer en Sebastiaan Haanappel wil ik hierbij apart noemen, omdat deze direct verwerkt zijn in dit proefschrift. Daarnaast wil ik Michael Wielant van Stork Fokker AESP bedanken voor zijn medewerking en hulp bij het uitvoeren van experimenten.

En natuurlijk, last but not least on the list, mijn zonnetje Marijke. Vooral, omdat je er altijd voor me bent.

René ten Thije
Enschede, september 2007